

# Process development and optical simulation of fully evaporated perovskite solar cells

Von der Fakultät für Elektrotechnik und Informatik  
der Gottfried Wilhelm Leibniz Universität Hannover  
zur Erlangung des Grades

Doktor der Naturwissenschaften  
Dr. rer. nat.

genehmigte Dissertation von

M. Sc. Marvin Diederich

geboren am 25.03.1992  
in Homberg (Efze), Deutschland

2023

Referent: Prof. Dr. Hans-Jörg Osten  
Korreferent: Prof. Dr. Robby Peibst  
Korreferent: Prof. Dr. Jan Schmidt  
Prüfungsvorsitz: Prof. Dr. Bernhard Wicht  
Tag der Prüfung: 13.02.2023

## Kurzzusammenfassung

Perowskite sind eines der vielversprechendsten Materialien für die nächste Generation von Solarzellen, insbesondere die Kombination einer Perowskit Topsolarzelle mit einer Silizium Bottomsolarzelle in einer Tandemsolarzelle. Perowskit-solarzellen werden jedoch durch verschiedene Umwelteinflüsse beeinträchtigt, und sowohl die Langzeitstabilität als auch die Reproduzierbarkeit des Herstellungsprozesses sind nach wie vor wichtige Probleme, die noch nicht gelöst sind. In dieser Arbeit werde ich die Herstellung von Perowskitsolarzellen mit dem aufgedampften Perowskit  $\text{MAPbI}_3$  detailliert beschreiben. Ich werde zeigen, dass diese Solarzellen derzeit vor allem unter zwei Mechanismen leiden, die den Wirkungsgrad begrenzen und eine Degradation verursachen. Der erste ist die Degradation durch Feuchtigkeit, die hauptsächlich durch hygroskopisches MAI in der Perowskitschicht verursacht wird, da unsere Prozessierung und Messung teilweise in Umgebungsatmosphäre stattfindet. Der zweite Effekt wird durch Ionenbewegung im Perowskit verursacht, die Hystereseeffekte und, sobald die Metallelektrode der Perowskitsolarzelle abgeschieden ist, auch langfristige Degradation verursacht. Ich werde skizzieren, wie beide Effekte in Zukunft durch Optimierungen der Herstellungs- und Messbedingungen bestimmt und minimiert werden können. Erste Experimente mit einigen dieser Optimierungen zeigen bereits Zellwirkungsgrade von bis zu 17%. Im zweiten Teil dieser Arbeit werde ich optische Simulationen sowohl von Perowskit-Single-Junction Solarzellen als auch von Perowskit-Silizium-Tandemsolarzellen vorstellen. Für die Perowskit-Single-Junction Solarzellen mit aufgedampftem  $\text{MAPbI}_3$  werde ich ein effektives Medium-Modell vorstellen, das verwendet werden kann, um variierende Absorption in  $\text{PbI}_2$  reichen  $\text{MAPbI}_3$  zu beschreiben. Für die Tandemsolarzellen werde ich die Auswirkungen der Vorder- und Rückseitentextur sowie einen neuartigen Poly-Silizium-Rekombinationsübergang zwischen den Perowskit- und Silizium-Subzellen auf die Stromerzeugung untersuchen.

Schlagworte: Perowskitsolarzelle, aufgedampftes  $\text{MAPbI}_3$ , optische Simulation, Perowskit Tandem

## Abstract

Perovskites are one of the most promising materials for next generation photovoltaics, especially the combination of a perovskite top solar cell with a silicon bottom solar cell in a tandem solar cell. Perovskite solar cells however suffer from degradation due to several ambient effects and long term stability as well as process reproducibility are still major issues to overcome. In this thesis I will explain the processing of perovskite solar cells with the evaporated perovskite  $\text{MAPbI}_3$ . I will show that these devices currently suffer mostly from two effects that limit efficiency and cause degradation. The first is degradation due to moisture mainly caused by hygroscopic MAI in the perovskite layer, since our processing and measurement partially takes place in ambient atmosphere. The second effect is caused by ionic movement in the perovskite, which causes hysteresis effects as well as long term degradation once the metal electrode of the perovskite solar cell is deposited. I will outline how to measure and minimize both effects in future with optimisations in the processing and measurement conditions. First experiments including some of these optimisations already show cell efficiencies up to 17%. In the second part of this work I will present optical simulations of both single-junction perovskite and perovskite-silicon tandem solar cells. For the perovskite single-junction cells with evaporated  $\text{MAPbI}_3$  I will present an effective medium model that can be used to identify the varying absorption in the  $\text{PbI}_2$  rich  $\text{MAPbI}_3$ . For the tandem solar cells I will discuss the optical effects of front and rear side texture as well as a novel poly-silicon recombination junction in between the perovskite and silicon subcells.

Keywords: perovskite solar cell, evaporated  $\text{MAPbI}_3$ , optical simulation, perovskite tandem



# Contents

<b>1</b>	<b>Introduction</b>	<b>1</b>
<b>2</b>	<b>Perovskite solar cell operation and deposition</b>	<b>3</b>
2.1	Perovskite solar cells: Fundamentals . . . . .	3
2.1.1	Cell design of perovskite solar cells . . . . .	3
2.1.2	Band alignment in perovskite solar cells . . . . .	4
2.1.3	Recombination and loss analysis . . . . .	7
2.1.4	Perovskite properties . . . . .	8
2.1.5	Co-evaporation of MAPbI <sub>3</sub> . . . . .	10
2.2	Cell geometry and processing in this work . . . . .	13
2.2.1	Cell geometry and processing overview . . . . .	13
2.2.2	Thermal evaporation and evaporation tools . . . . .	15
2.2.3	Deposition process and thickness accuracy of the contact layers . . . . .	16
2.2.4	Perovskite deposition . . . . .	17
2.2.5	Cell area, series resistance and upscaling of perovskite solar cells . . . . .	18
2.2.6	Encapsulation . . . . .	19
<b>3</b>	<b>Perovskite properties</b>	<b>21</b>
3.1	Perovskite processing . . . . .	21
3.1.1	Impact of substrate temperature . . . . .	21
3.1.2	MAI properties . . . . .	22
3.1.3	Cross-Contamination . . . . .	26
3.2	Influence of PbI <sub>2</sub> to MAI ratio . . . . .	28
3.2.1	Crystal properties and hydrate formation in MAPbI <sub>3</sub> . . . . .	29
3.2.2	Morphology and grain size of MAPbI <sub>3</sub> . . . . .	31
3.2.3	Photoluminescence and recombination . . . . .	34
3.3	Summary: Air exposure and reproducibility . . . . .	38

<b>4</b>	<b>Cell measurements of PSCs</b>	<b>39</b>
4.1	Cell reproducibility and influence of process conditions . . . . .	41
4.1.1	Refilled MAI and effect of MAI excess . . . . .	41
4.1.2	Fresh MAI and temperature controlled processes . . . . .	43
4.1.3	Chamber cleaning . . . . .	45
4.1.4	Dark-IV and Shunts . . . . .	47
4.1.5	Influence of $\text{PbI}_2$ excess on processing stability . . . . .	49
4.1.6	Processing and measurements without ambient atmosphere and efficiency potential . . . . .	53
4.2	PSC solar cell stability and measurement . . . . .	54
4.2.1	Ionic charge transport, charge accumulation and hysteresis .	54
4.2.2	Cell stability, aging and s-shape . . . . .	57
4.2.3	Ionic movement and how to measure perovskite solar cells .	59
4.2.4	$QFLS$ , $V_{OC}$ and photoluminescence of perovskite solar cells	61
<b>5</b>	<b>Optics of perovskite solar cells</b>	<b>65</b>
5.1	Basics of optical simulation . . . . .	65
5.2	Complex refractive index . . . . .	67
5.2.1	Effective medium model . . . . .	71
5.3	$EQE$ measurements and optical simulations at ISFH . . . . .	73
5.3.1	Influence of the perovskite layer on current generation . . .	73
5.3.2	Simulation study for optimised current generation . . . . .	76
5.3.3	$EQE$ measurements of perovskite solar cells at ISFH . . . . .	78
5.3.4	Approach to optical simulation for PSCs . . . . .	84
5.3.5	Thickness gradient . . . . .	87
5.3.6	$EQE$ and reflection - long term stability . . . . .	88
5.3.7	Different perovskite band gaps . . . . .	89
5.4	Optical simulation of tandem cells . . . . .	91
5.4.1	Impact of texture and parasitic absorption . . . . .	92
5.4.2	Influence of recombination junction and current optimisa- tion in tandem solar cells . . . . .	95
5.4.3	Current matching in tandem solar cells . . . . .	97
5.5	Chapter summary . . . . .	100
<b>6</b>	<b>Summary: Results and outlook</b>	<b>101</b>
6.1	Results . . . . .	101
6.2	Outlook . . . . .	102
	Appendix - sheet resistance in TCO . . . . .	124

# 1 Introduction

Lead halide perovskite solar cells have gained a lot of attention in the scientific community in the recent years since the first published perovskite solar cells in 2009 [1]. Since then, perovskite solar cells with up to 25.5% efficiency have been demonstrated [2, 3]. This is already relatively close to the 26.7% efficiency of the best performing silicon solar cell [4]. Since lead halide perovskites are a material class it is possible to tune their band gap which makes them suitable for different tandem solar cells [5, 6]. The combination of a perovskite top solar cell with a silicon bottom solar cell is especially appealing [7, 8, 9], because silicon solar cells are dominating the market for solar cells [10] and many of the current industrial tools used for commercial solar cell production could still be used. Perovskite-silicon tandem solar cells have achieved efficiencies of over 29% [2, 11]. This makes perovskites one of the most promising candidates for future photovoltaic applications.

ISFH started perovskite solar cell development in mid-2016. This work mostly features the progresses made in single perovskite cells with the perovskite methylammonium lead iodide ( $\text{MAPbI}_3$ ) from the first processed perovskite solar cells at around the end of 2019 to our current (Q1/2022) highest efficient perovskite solar cells.

The ultimate goal at ISFH is to combine high efficiency ISFH-processed silicon solar cells [12] as a bottom cell with a ISFH-processed perovskite top solar cell for an efficient tandem solar cell.

One of the major downsides of perovskite solar cells is their instability [13, 14] and the scalability of the perovskite deposition. Currently, most high efficient perovskite single-junction or tandem solar cells have a size of  $1 \text{ cm}^2$  or less and perovskite solar cells with larger areas are worse in terms of performance [15, 16, 17]. With spin-coating, the most common deposition technique, it is difficult to conformally coat large areas or rough surfaces like textured silicon [15, 18]. In this work, we use thermal evaporation for the deposition of the perovskite methylammonium lead iodide ( $\text{MAPbI}_3$ ), because it allows homogeneously thick layers on large areas and textured surfaces [19, 20].

## CHAPTER 1. INTRODUCTION

In chapter 2 I explain the basic principles of operation for perovskite solar cells as well as some of the unique features occurring in perovskites, for example ion migration. Additionally, I show how we process our perovskite solar cells at ISFH and our cell design.

In chapter 3 I discuss the reproducibility of the perovskite deposition and different non-cell properties of the deposited perovskite layers measured with x-ray diffraction (XRD), scanning electron microscopy (SEM) and photoluminescence (PL). I discuss how the ratio of the perovskite educts lead iodide ( $\text{PbI}_2$ ) and methylammonium iodide (MAI) during perovskite deposition affects for example grain size or water diffusion into the perovskite.

In chapter 4 I present the cell results of our perovskite solar cells and discuss how the ratio of  $\text{PbI}_2$  to MAI during perovskite deposition affects the cell performance. I also discuss several other effects, like how shunts in our solar cells originate. In addition, I discuss hysteresis, s-shape and short and long term stability of our perovskite solar cells, as well as the mechanisms behind degradation and performance losses.

In chapter 5 I show the refractive indices of all layers of our perovskite solar cells, which I measured with spectroscopic ellipsometry. I introduce an effective medium model for the perovskite, which accounts for the varying absorption in the perovskite layer. Chapter 5 also features optical simulations of our perovskite solar cells and compares the external quantum efficiency of measured devices with these simulations to identify current losses in our cells. In the second part, I present optical simulations of various types of tandem solar cells with a top perovskite and bottom silicon solar cell to quantify the effect of both texture and a poly-silicon recombination layer.

In chapter 6 I summarize the results from chapter 2 to 5 and explain how to improve the processing and measurement conditions for better and more stable perovskite solar cells in future.

# 2 Perovskite solar cell operation and deposition

In this chapter, I will discuss the fundamental properties and processing of perovskite solar cells (PSCs). First, I will explain the structure of a PSC in general and the one displayed in this work. Then I will discuss different processing possibilities for different layers applied in PSCs as well as the impact of environmental conditions on them. Lastly, I will explain the deposition methods used here to fabricate the PSCs.

## 2.1 Perovskite solar cells: Fundamentals

### 2.1.1 Cell design of perovskite solar cells

A solar cell consists of a semiconductor material where charge carriers (electrons and holes) are generated by absorbing light. For a PSC a metal halide perovskite, which is a direct band gap semiconductor [21], serves this purpose. The generated charge carriers are extracted with charge selective layers, that block one of the charge carriers and let the other charge carrier pass through for both electrons and holes, ideally without energy loss. These are called electron transporting layer (ETL or ETM for electron transporting material) and hole transporting layer (HTL or HTM for hole transporting material) respectively. The third integral component are contacts that collect the charge carriers and transport them into an external circuit for power generation. A more detailed explanation about solar cell operation in general can be found in [22].

For a thin film solar cell like a PSC, in contrast to e.g. silicon, which serves as its own substrate, an additional substrate is needed. PSCs can be deposited onto a glass substrate or a transparent foil [23] as well as a silicon solar cell for tandem applications for example. In the case of a single junction perovskite solar cell, glass is the most common substrate. Onto the glass substrate a transparent conductive oxide (TCO, mostly Indium Tin Oxide (ITO) or Fluorine doped Tin

Oxide, FTO) is sputtered as the front contact [24].

Next, the perovskite embedded in the charge selective layers is deposited, followed by the back contact, which is typically evaporated metal (copper, silver or gold).



Figure 2.1: p-i-n type PSC.

Due to the perovskite being not intentionally doped in most cases, they are often considered intrinsic (i), contrary to the electron (n) and hole (p) transporting materials. PSCs where the perovskite is deposited onto the electron transporting layer are called n-i-p type. If the perovskite is deposited onto the hole transporting layer the cell is called p-i-n type [25]. A p-i-n type PSC is schematically shown in Figure 2.1. Historically, the first published PSCs had a n-i-p type structure with mesoporous  $\text{TiO}_2$  as an electron transporting layer [1] and up to now n-i-p-type PSCs

achieve the highest efficiencies [3]. For this reason n-i-p type PSCs are often labelled standard structure and p-i-n type PSCs as inverted structure.

For the perovskite as well as the ETL and HTL several deposition methods are utilised. These include wet chemical methods like spin-coating, dip-coating, blade-coating, slot-die coating or chemical bath deposition as well as evaporation or sputtering [17]. There also exists a wide variety of different materials for both the HTL and ETL. Typical materials for the ETL are inorganic metal oxides such as  $\text{ZnO}_x$ ,  $\text{SnO}_x$  or  $\text{TiO}_x$  as well as variants of fullerene based organic materials like C60 or PCBM [26, 27]. For the HTL, again metal oxides or sulfides like CuS,  $\text{NiO}_x$  or  $\text{MoS}_x$  or organic molecules like P3HT, PTAA or spiro-OMETAD are used [28, 29]. Recently, organic self-assembled monolayers (SAMs) have shown to be a promising candidate for the hole transporting layer in a PSC [30]. Combinations of contact layer materials as well as doping of the contact layers is utilized in some cases to improve the device performance [31, 32, 33]. The material combinations and deposition methods for the contact layers are therefore plentiful and also rapidly evolving. The following chapter explains some of the properties of the contact layers.

### 2.1.2 Band alignment in perovskite solar cells

As already mentioned, one important aspect of a charge selective layer is that one polarity of carriers is blocked and the other passes through. To explain a couple

## 2.1. PEROVSKITE SOLAR CELLS: FUNDAMENTALS

Material	ITO	spiro-TTB	MAPbI <sub>3</sub>	C60	BCP	Au
Function	TCO	HTL	Perovskite	ETL	ETL	Electrode
Source	[34]	[35]	[34]	[34]	[34]	[36]
WF/LUMO/CB [eV]	-4.8	-2.1	-3.9	-4.2	-3.5	-5.1
HOMO/VB [eV]		-5.2	-5.4	-5.9	-7	

Table 2.1: Energy level of electrons and holes for perovskite (MAPbI<sub>3</sub>), charge selective layers (spiro-TTB, C60, BCP), TCO (ITO) and electrode (Au).

Green: Pathway of holes in PSC, Red: Pathway of electrons in PSC. The charge carriers are extracted from the perovskite layer into the ITO (holes) or Au (electrons).

of properties these charge selective layers have to fulfill, we take a look at the materials used as hole and electron transporting layers for the solar cells presented in this work.

Table 2.1 shows the energy level of the work functions for the TCO and electrode, the energies of the highest occupied and lowest unoccupied molecule orbital (HOMO and LUMO) for the organic contact layers (spiro-TTB, C60 and BCP) as well as the valence and conduction band of the perovskite MAPbI<sub>3</sub>.

If we look at the pathway for holes (light green in Table 2.1) for this solar cell design, we can see that the energy levels of unexcited electrons in spiro-TTB and ITO are higher than in the perovskite, which means that holes in the perovskite layer will be filled up by electrons in spiro-TTB and ITO, therefore extracting the holes. The energy level of unexcited electrons on the C60 and BCP side is lower than in the perovskite, therefore hole transport is blocked in this direction. The offset between the energy of unexcited electrons in C60 and the perovskite is only 0.5 eV, whereas for BCP to perovskite this offset is 1.6 eV. Because of the small offset of C60 to perovskite, the capability to block holes effectively is higher with the additional BCP, which leads to higher achievable cell efficiencies (to be precise: higher open circuit voltages) [37].

If we look at the pathway for (excited) electrons in our solar cell, it is efficiently blocked by spiro-TTB with a 1.8 eV offset. The energy level for electrons in C60 is lower than in the perovskite, so electrons generated in the perovskite layer are extracted into the C60. If we look at the energy level of electrons in the BCP there is an energetic offset of 0.7 eV to C60, which would cause blocking of the electrons and therefore no efficient charge carrier extraction would occur. This barrier is however removed due to interdiffusion of metal atoms into BCP, creating gap-states with energies lower than the conduction band in the perovskite or the LUMO of C60 [38, 34], and therefore BCP still functions as an effective electron selective layer in combination with a metal layer, in this case the Au.

In this example, which is the layer sequence of the PSCs presented in this work, the spiro-TTB serves as the hole transporting layer (HTL) and C60 and BCP combined as electron transporting layer (ETL).

If BCP is effectively blocking holes and transporting electrons, the question arises, why C60 is even needed. In this specific case, the reason why BCP is not used alone is because of the low extraction efficiency of electrons due to the low mobility of electrons at the BCP/perovskite interface which causes low performance of solar cell without the additional C60 [34]. In the above mentioned publication, they could show that even a one nanometer thick C60 layer between the perovskite and BCP is enough to achieve good solar cell efficiencies.

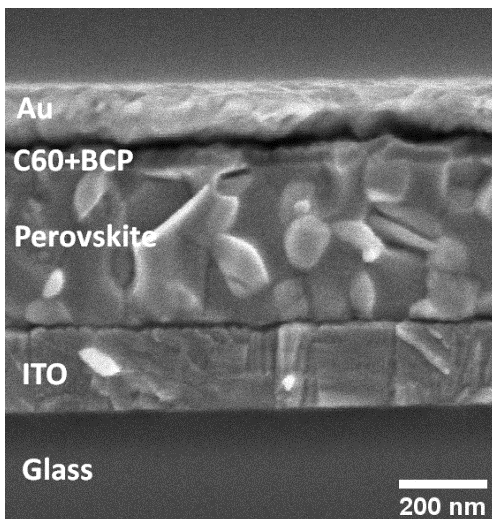


Figure 2.2: Cross section of a PSC made at ISFH.

However, when C60 is deposited on top of the perovskite, it is typical to use a C60 layer of around 20 nm [11, 39] for high performing solar cells. Too thin layers can cause an incomplete coverage of the surface, which leads to losses in the fill factor of the solar cell [40]. Figure 2.2 shows a scanning electron microscope (SEM) image of one of the solar cells processed at ISFH with the cell stack given in Table 2.1. The ITO and perovskite feature some surface roughness (for the perovskite in a typical range of 10 to 30 nm for most of our solar cells), which necessitates thicker charge selective layers for a complete surface coverage as for completely smooth surfaces. The perovskite morphology changes drastically with the deposition techniques and processing parameters (as will be discussed in chapter 3 for our processing) and therefore the ideal thickness of charge selective layers is highly dependent on the processing conditions of the other layers, especially the perovskite. Increasing the thickness of the charge selective layer can lead to an increase in series resistance, reducing the efficiency of the solar cell [41]. Comparing similar charge selective layers amongst different research groups gets furthermore complicated due to different processing and ambient conditions, altering their properties [42].



### 2.1.3 Recombination and loss analysis

Another important aspect of the charge selective layer is the recombination at the perovskite interface. In silicon solar cells a passivation layer at the silicon surface is needed to reduce surface recombination [43]. Contrarily, perovskites exhibit only low surface recombination or recombination at grain boundaries and adding a charge selective layer increases recombination and decreases carrier lifetime in most cases [44, 45, 46].

To summarize, a charge selective material in a perovskite solar cell has to fulfill the following conditions:

- Effective extraction of desired charge carrier
- Blocking of non-desired charge carrier
- Low recombination at perovskite interface
- Low contact resistances and sheet resistance
- Compatibility to the overall cell processing (e.g. thermal/mechanical stability)
- Commercial aspects: Wide process window, cheap, fast processing, good reproducibility etc.

By measuring the photoluminescence quantum yield (PLQY) and thereby quantifying the amount of radiative recombination in the perovskite, it is possible to determine the quasi-fermi level splitting (QFLS) of a perovskite with contact layers which makes a quantitative comparison of the open-circuit voltage ( $V_{OC}$ )-potential of different contact layers possible [47, 48]. By comparing the  $V_{OC}$  calculated from the QFLS to the solar cell  $V_{OC}$ , it is possible to identify whether the cell  $V_{OC}$  is limited by nonradiative recombination in the perovskite layer [ $V_{OC}(QFLS)=V_{OC}(Cell)$ ] or restricted due to losses at the interfaces [ $V_{OC}(QFLS)>V_{OC}(Cell)$ ] because of, for example, band bending at non-selective contacts [47]. Combined measurements of the solar cell ideality factor [49] with PLQY measurements were recently demonstrated for a refined loss analysis of perovskite solar cells [50].

Chapter 4.2.4 will present a first look at photoluminescence measurements compared to the open circuit voltage for the cell stack processed in this work.

### 2.1.4 Perovskite properties

Perovskites used for solar cells are so called metal halide perovskites, with a perovskite crystal structure and the sum formula of  $ABX_3$  with A being a (organic) cation, B a metal (mostly lead) and X being a halide (iodide, chlorine or bromine) [51]. Replacements for lead concerning its toxicity and potential negative environmental impact are discussed, but perovskites solar cells without lead suffer from poor performance [52]. For the halide component a single halide as well as mixtures of two or three halides (I, Br, Cl) are used [9, 11]. For the cation component the two organic molecules formamidinium and methylammonium as well as the alkali metal caesium are common [53]. Perovskites with only caesium as cation component are often called inorganic perovskite. Although the highest performing perovskite solar cells use a multi-cation-multi-anion (MKMA) perovskite composition [11], methylammonium lead iodide ( $MAPbI_3$ ) is the most thoroughly investigated composition for fundamental properties of metal halide perovskites. Since  $MAPbI_3$  is the perovskite used in this work as well, I will explain a few basic properties of perovskites in general as well as  $MAPbI_3$  in specific using  $MAPbI_3$  as an example.

$MAPbI_3$  is a direct semiconductor with a band gap of about 1.6 eV [54]. It is formed by the reaction of methylammonium iodide (MAI) and lead iodide ( $PbI_2$ ). The unique feature that makes it so appealing for solar cells is that most common defects in its crystal lattice are only shallow and act as sort of doping instead of deep trap states [55, 56, 57]. The exact mechanisms behind the high carrier lifetimes in  $MAPbI_3$  are however still in debate [58].

Grain boundaries that are normally detrimental to solar cell performance are not necessarily the limiting factor for cell efficiency in perovskite solar cells due to them being electrically neutral during solar cell operation [46].

Another key difference compared to other semiconductors used for solar cells like silicon is that the multicrystalline perovskite layer is not stable at room temperature and ions (especially iodide) can move through the perovskite layer, likely at grain boundaries [59], especially after for example excitation with light [60, 61]. Ion migration is however detrimental for the performance and stability of perovskite solar cells [62, 63]. Most perovskite layers are multi-crystalline, with grain sizes from a few nanometer to several micrometers (see e.g. Figure 2.2 for a perovskite grown at ISFH). Due to the movement and accumulation of ions in perovskites hysteresis phenomena can occur for solar cell operation, which can lead to an s-shape like form of the light IV-curve [60, 64]. Hysteresis effects of

## 2.1. PEROVSKITE SOLAR CELLS: FUNDAMENTALS

perovskite solar cells measured at ISFH were investigated in the master thesis of Moritz Engl [65] and will be featured in chapter 4.2.1 in this work as well. An example for ionic movement in  $\text{MAPbI}_3$  is depicted in Figure 2.3.

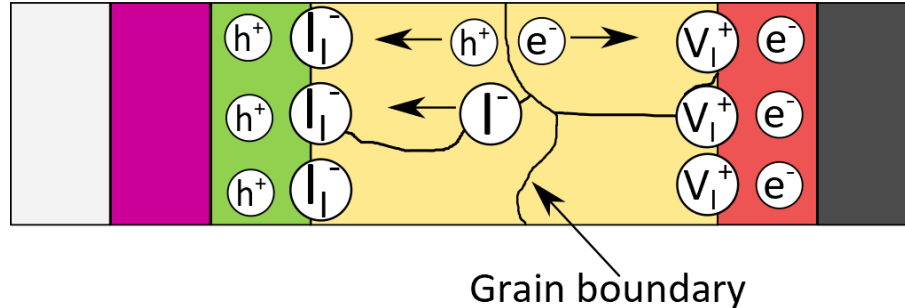


Figure 2.3: Ionic movement and accumulation of ions in a perovskite under solar cell operation. Electrons ( $e^-$ ) and holes ( $h^+$ ) move to their respective contacts, free ions (shown in this case for iodide ( $I^-$ )) move in respect to their charge along the grain boundaries to the respective contacts and accumulate, creating additional charged interstitials ( $I^-$ ) or vacancies ( $V_I^+$ ) at the contact layer interfaces [59, 66].

Additionally, perovskite solar cells are prone to degradation due to for example oxygen or moisture, which causes concerns in terms of long-term stability of perovskite solar cells [67, 68, 69]. A certain, controlled amount of moisture during perovskite processing can however lead to improved device performance. The incorporation of water into the perovskite, which is mediated by the hygroscopic MAI, leads to a self-annealing of the perovskite layer, reducing crystal defects [70]. Due to the importance of the environmental conditions during processing, storing and measurement on device performance, most high performing perovskite solar cells are manufactured in a glovebox atmosphere where the environmental conditions can be precisely controlled. Perovskite solar cells processed without artificially controlled environmental conditions fall short in terms of efficiency [71, 72].

Another influence factor is the non-stoichiometry of the perovskite layer. Stoichiometric  $\text{MAPbI}_3$  consists of an equal amount of MAI and  $\text{PbI}_2$ , but there are numerous reports of perovskite solar cells with either MAI or  $\text{PbI}_2$  excess. There are reports for both MAI excess [73, 74] as well as  $\text{PbI}_2$  excess [75, 76, 77] being beneficial or detrimental for device performance.  $\text{PbI}_2$  is reported to accumulate at perovskite grain boundaries, passivating them [78, 79]. For high amounts of  $\text{PbI}_2$  excess in the perovskite layer, the crystalline amount of  $\text{PbI}_2$  does not increase and amorphous  $\text{PbI}_2$  starts to form, which is reported to be detrimental to

cell performance [76]. Many results of these reports often contradict each other at first glance, however most differences in these reports likely stem from the different processing conditions and measuring conditions of the solar cells. In a bachelor thesis published in 2019 the perovskite layer processed with a wet-chemical deposition method showed visible differences after two nominally identical processes, revealing the often unstable processing [80].

It is therefore crucial for the development of perovskite solar cells to control the processing and environmental conditions as good as possible to receive meaningful results.

### 2.1.5 Co-evaporation of $\text{MAPbI}_3$

For the deposition of the perovskite layer the most common approach is a wet-chemical deposition, mostly spin-coating. The first published perovskite solar cells [1] as well as the highest performing solar cells to date, both as single-junction [3] and as a perovskite-silicon tandem solar cell [11] use spin-coated perovskites. Wet-chemical processes have the disadvantage that coating on rough substrates, like front side textured silicon, results in inhomogeneous thick films [18]. This can be bypassed by vacuum-deposition of the non-organic component and then wet-chemical deposition of the organic component [7]. After the wet-chemical deposition the deposited perovskite precursors are annealed to form the perovskite [70, 81, 82].

In 2013, Snaith et. al demonstrated a solar cell with a fully thermally evaporated perovskite ( $\text{MAPbI}_3$ ) with an efficiency of 15.4%, which was at that point one of the highest reported efficiencies of a perovskite solar cell [18]. Compared to wet-chemical deposited films evaporated perovskites have the advantage of coating textured surfaces with a homogeneously thick layer [83]. The best cell efficiencies of evaporated perovskites today (Q2/2022) are however about 5% absolute efficiency lower than their solution-processed counterpart, both as single-junction [84] and as perovskite-silicon tandem solar cells [85]. This raises some concerns, that evaporation may not be a suitable option in the long term and evaporation based PSCs are a niche even in the perovskite community [86].

With a sequential evaporation method, by repeatedly depositing  $\text{PbI}_2$  and afterwards MAI followed by an annealing step, cell efficiencies of 20% could be demonstrated [87]. The more common approach for thermal evaporation is however to simultaneously evaporate the precursor molecules for the perovskite from two or more crucibles, which is called co-evaporation, as can be seen in Figure 2.4 for the co-evaporation of  $\text{MAPbI}_3$ . For co-evaporated perovskites, there are still

## 2.1. PEROVSKITE SOLAR CELLS: FUNDAMENTALS

differences in the deposition methods. For most evaporated thin films a quartz crystal monitor (QCM) is used during processing to determine the deposition rate for each deposited material independently.

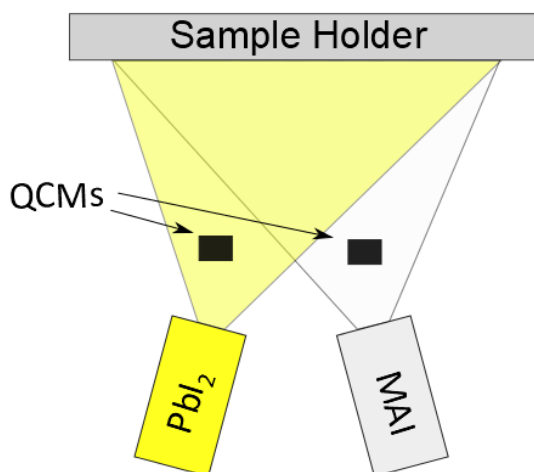


Figure 2.4: Co-evaporation of PbI<sub>2</sub> and MAI.

Unfortunately, the organic component of MAPbI<sub>3</sub>, MAI, is reportedly difficult to measure using QCM due to partial decomposition when evaporated, an adsorbance highly influenced by the substrate as well as diffuse evaporation of MAI, influencing the measured deposition rate of other sources [84, 88, 39]. Caused by this uncommon behaviour, two specific types of evaporation chambers have been developed to still perform QCM-based deposition of MAI based perovskites. These reduce the influence of the diffuse evaporation of MAI. One option is to add an additional QCM next to the sample holder, as well as a shielding surrounding the QCM for PbI<sub>2</sub> [39]. Another option is to cool the surrounding surfaces of the MAI crucible to reduce the diffuse evaporation that impacts the measurement of PbI<sub>2</sub> [84]. With both setups solar cell efficiencies of over 20% could be demonstrated. These sophisticated evaporation chambers are however not available for every research group that focusses on evaporated perovskites.

Two other methods that do not require QCM are therefore commonly employed. The first is to measure the diffuse evaporation of MAI by controlling the chamber background pressure [89, 90, 91]. The second one is to keep the MAI temperature constant during processing [92, 93]. Similar to the sophisticated approaches with QCM monitoring, efficiencies of up to 20% could be achieved with these approaches.

Since the MAI partially decomposes during heating [88], the MAI crucible is typically completely emptied and refilled after each process, therefore the starting MAI properties remain similar from process to process [91]. Other materials for evaporation like PbI<sub>2</sub> are typically used in several consecutive evaporations. An-

other important aspect of the evaporation of MAI is that the impurities in the MAI source material affect the amount of evaporated MAI as well as perovskite properties [88]. All groups that reported solar cell efficiencies of more than 20% with co-evaporated MAPbI<sub>3</sub> use high purity MAI from one specific supplier (LumTec) [39, 84, 93].

Up to this point, I mainly discussed the influence of the properties of the MAI itself on the evaporation process, the substrate properties are however important as well. The amount of MAI incorporated into the perovskite is decreasing with increasing substrate temperature and most groups use a substrate temperature of about 25 °C (room temperature) for efficient perovskite solar cells [84]. There are reports that reducing the amount of MAI incorporated into the perovskite by increasing the temperature during evaporation leads to smaller grain sizes (more grain boundaries) but higher efficiencies in the solar cells [94]. Other publications note the same trend for grain sizes but little to no effect on the solar cell efficiencies [83, 39]. Some reports show that there is a relatively wide process window in terms of the ratio of PbI<sub>2</sub> to MAI incorporated into the perovskite without any big effects on cell efficiencies [83, 39]. This process window however refers only to the calculated precursor ratio from measuring the evaporation rates of the precursors, not the resulting perovskite composition. The MAI incorporation is reported to be increased for a PbI<sub>2</sub> rich surface [84, 39], which could cause the perovskite layers deposited to be more stoichiometric than by just measuring the evaporation rates of MAI and PbI<sub>2</sub>.

X-ray diffraction (XRD) measurements on several evaporated perovskite films show crystalline PbI<sub>2</sub> in the perovskite, even for high efficiency solar cells with a stoichiometric precursor ratio [84, 95]. The charge transport layer on which the perovskite is deposited also affects the grain size and crystallite morphology of the perovskite layer [84, 91].

All of the above cited reports of high efficiency perovskite solar cells with co-evaporated perovskites are processed and measured in a glovebox with nitrogen atmosphere. The processing tools for evaporation are loaded through a glovebox, so that no contact of the samples with ambient atmosphere occurs. Additionally, they deposit the perovskite layer in a designated evaporation chamber for only the perovskite. Although not reported, this is likely to reduce cross-contamination of the contact layers with MAI, which contaminates the whole chamber (see section 3.1.3 for more information). There are other groups that do not have the possibilities to process their solar cells in separate deposition tools without contact to ambient atmosphere (including ISFH as I will explain

## 2.2. CELL GEOMETRY AND PROCESSING IN THIS WORK

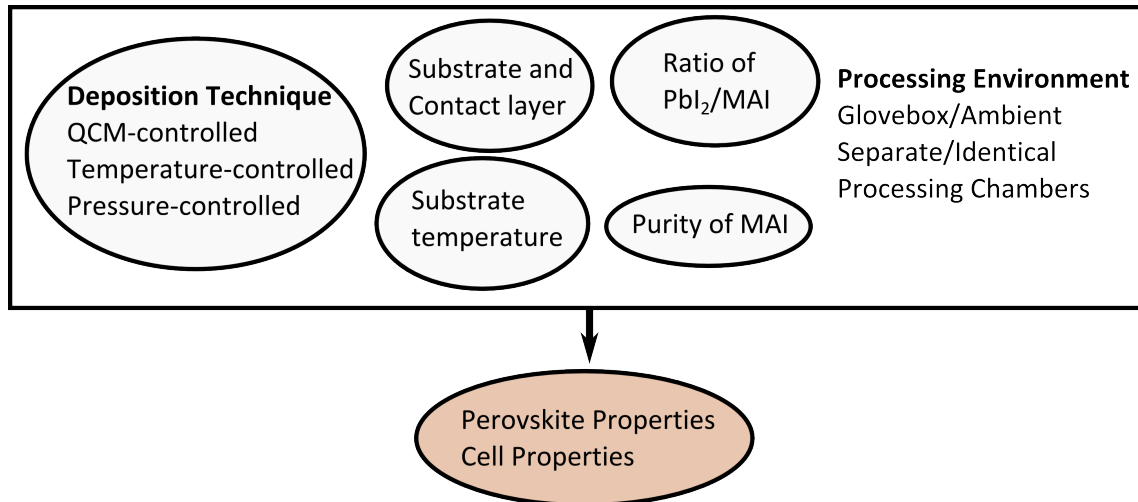


Figure 2.5: Known influence factors for the thermal evaporation of the perovskite that determine the perovskite and cell properties.

later). Their reported devices are however much worse compared to the ones mentioned above [96]. In this work, I will show experiments on the influence of several of the factors depicted in Figure 2.5, including substrate temperature, the MAI source material and the effect of  $\text{PbI}_2$  or MAI excess on our solar cells.

## 2.2 Cell geometry and processing in this work

### 2.2.1 Cell geometry and processing overview

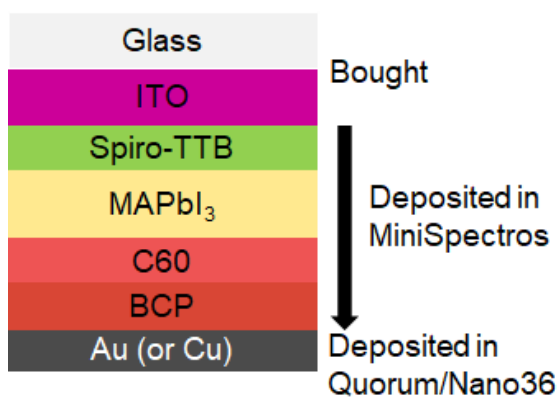


Figure 2.6: Cell geometry of ISFH  $\text{MAPbI}_3$ -based perovskite solar cells as well as the tools used for deposition.

The solar cells in this work are p-i-n-type perovskite solar cells. We use ITO coated glass as substrate and TCO that is bought from PGO. Then we thermally evaporate spiro-TTB (LumTec) as HTL,  $\text{PbI}_2$  (Strem Chemicals) and MAI (made at ISFH or from LumTec) to form the perovskite  $\text{MAPbI}_3$ , C60 (Sigma Aldrich/Across Mechanics) and BCP (Sigma Aldrich) as ETL and gold or copper as electrode material. The resulting cell stack is shown in Figure 2.6. Abzieher et al.

already demonstrated solar cells with over 19% efficiency with this combination

of layers in a fully evaporated perovskite solar cell [91].

All samples shown in this work are deposited on square-sized substrates with an area of  $2.5 \times 2.5 \text{ cm}^2$ . For the solar cells we pre-structure the ITO coated glass by partial laser ablation to get four individual solar cells on each substrate. Additionally we use front-side polished silicon wafers for ellipsometry or SEM measurements and float glass for transmission and reflection measurements to identify non cell-properties of the deposited layers. The ITO coated glass is cleaned in an ultrasonic bath in three consecutive steps with Mucisol (soap), isopropanol and acetone before the deposition of the other layers. The perovskite and contact layers are all thermally evaporated in a Lesker MiniSpectros. The electrode material (gold or copper) is evaporated in a second chamber, for the most part a Quorum Q300T plus. A second evaporation tool (Lesker Nano36) for the metallisation was just recently (Q4/2021) employed at ISFH.

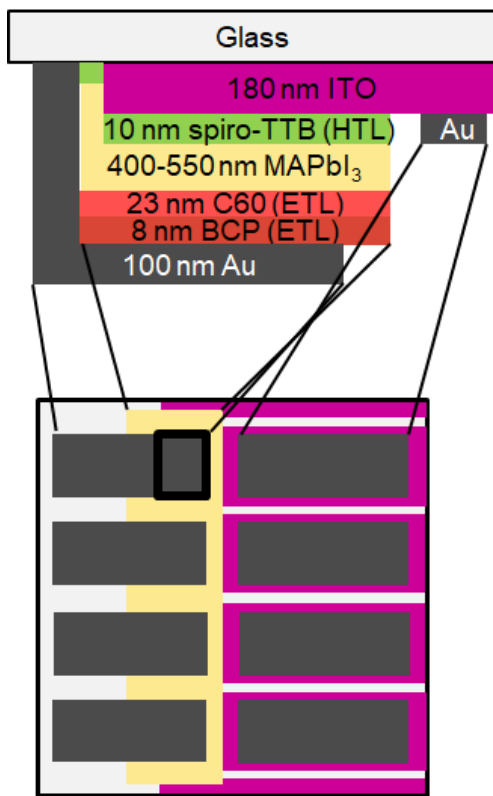


Figure 2.7: Top: Schematic view of our  $\text{MAPbI}_3$  solar cell including the typical layer thicknesses of each material. Bottom: Actual scale of each layer on a  $2.5 \times 2.5 \text{ cm}^2$  substrate.

By employing masks during evaporation of the contact layers and perovskite ( $\text{MAPbI}_3$ ) as well as during metal evaporation we create the cell pattern that is shown in Figure 2.7. The yellow colour depicts the area, where the contact layers and perovskite are deposited and the grey colour shows the area of the metal electrode (Au). The ITO is purple and the bright grey area is where the ITO is removed during the pre-structuring process. The overlap of ITO, contact layers, perovskite and electrode is the active cell area, depicted as the small black square in the first “stripe” in Figure 2.7. This area has a size of  $3 \times 4 \text{ mm}^2$  ( $0.12 \text{ cm}^2$ ). The cell is contacted at the outer area of the gold metallisation on each side, avoiding short-circuiting by pressing the contact needle through the perovskite layer. This design has the disadvantage, that the actual “device area” ( $4 \times 0.12 \text{ cm}^2$ ) in comparison to the overall

area of the substrate ( $6.25 \text{ cm}^2$ ) is quite small ( $< 10\%$ ). Compared to an industrial



## 2.2. CELL GEOMETRY AND PROCESSING IN THIS WORK

silicon solar cell with several hundred square centimeters our solar cells are much smaller, but actually a typical size for lab-type perovskite solar cells [93].

### 2.2.2 Thermal evaporation and evaporation tools

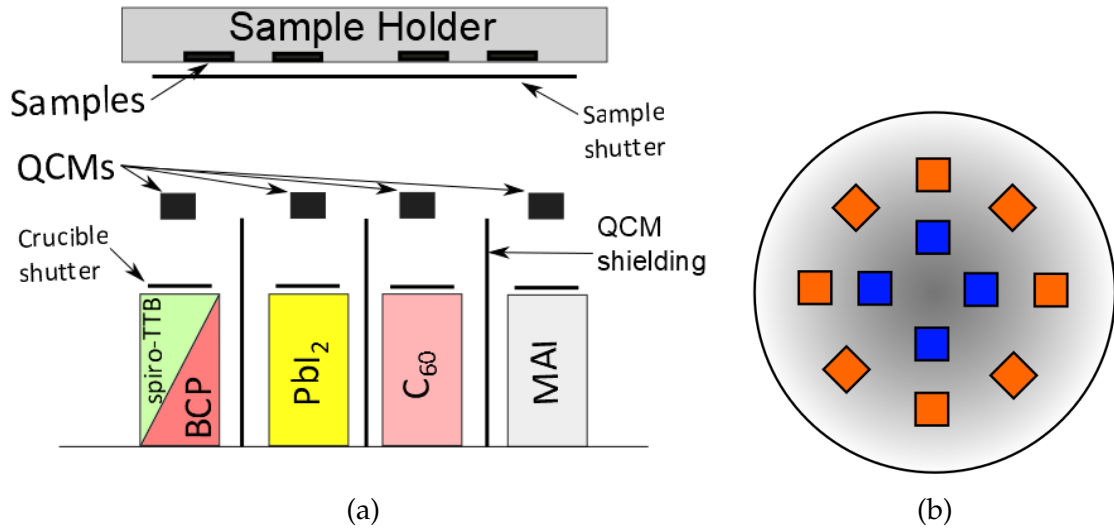


Figure 2.8: (a) Schematic overview of the MiniSpectros thermal evaporation system used in this work (b) Sample holder used in the MiniSpectros with 4 inner (blue) and 8 outer (orange) sample positions.

The Lesker MiniSpectros, where we deposit the contact layers and the perovskite (MAPbI<sub>3</sub>) via thermal evaporation, is schematically drawn in Figure 2.8a. We have four different crucibles that are heated with a filament. Each crucible has a separate quartz crystal monitor (QCM). Because of the defined position of the QCM in respect to the sample holder, the amount of material deposited on the QCM compared to the samples is constant for each crucible and material and called tooling factor. The QCMs of the different crucibles are separated by a metal shielding to reduce unwanted deposition of material on QCMs of neighbouring crucibles. Each crucible has a crucible shutter to reduce undesired evaporation of material into the chamber. In front of the sample holder is a sample shutter. If the crucible shutter is open the rate of evaporated material can be measured. As soon as a desired rate is reached the sample shutter opens to start the deposition of material on the sample. The sample holder has 12 positions for 2.5×2.5 cm<sup>2</sup> samples (see Figure 2.8b) with 8 outer (orange) and 4 inner (blue) sample positions. Its temperature (the substrate temperature) is controlled with an external cooling circuit. The sample holder is rotating during the evaporation, so that the amount of deposited material is similar for each position. There is however a

thickness gradient from the inside (blue positions) to the outside (orange positions) as indicated by the gray scale in Figure 2.8b.

The whole evaporation chamber is loaded through a nitrogen-filled glovebox to minimize effects on the perovskite solar cell due to oxygen or moisture. For the metal evaporation we use similar systems (Quorum Q300T plus and Lesker Nano36). The Quorum Q300T plus is not incorporated in a glovebox, therefore samples processed in this chamber are exposed to ambient conditions before and after each evaporation. The sample holder is not cooled as well, leading to temperatures of up to 100 to 130 °C on the samples. An investigation of the temperatures during metallisation as well as its influence on cell performance was done in the bachelor thesis of Niko Mielich [97]. As discussed above (chapter 2.1.4), an uncontrolled exposure to ambient atmosphere is detrimental to cell performance. This makes the Quorum Q300T plus not suitable for high performing solar cells and stable processing. The Nano36 is loaded from a glovebox and has a cooled sample holder, similar to the MiniSpectros which mitigates the disadvantages of the Quorum Q300T plus.

### 2.2.3 Deposition process and thickness accuracy of the contact layers

For the evaporation of the contact layers, the crucibles get preheated until about 50 °C below the typical evaporation temperature. Then the crucible shutter is opened and the crucible is heated further until a specific deposition rate is measured with the QCM. The heating power and deposition rate are regulated with a power control of the heating filament. The power is regulated by a PID controller. After the desired rate ( $0.25 \text{ \AA}/\text{s}$  for the contact layers) is obtained, the substrate shutter opens until the desired thickness of each material is reached. For all contact layers we use a substrate temperature of 25 °C.

For our solar cells, we employ thicknesses of 10 nm for spiro-TTB, 23 nm for C60 and 8 nm for BCP. As mentioned above, there is a thickness gradient from the inside to the outside of the chamber. The thickness of the inner samples is about  $1.14 \pm 0.02$  times the thickness of the outer samples (thicknesses measured with spectroscopic ellipsometry for C60, spiro-TTB and BCP). For one sample position (inner or outer) the thickness of the contact layers between processes varies by  $\pm 10\%$  of the total thickness, different samples in one process have only marginally different thicknesses, as is shown for spiro-TTB in Figure 2.9.

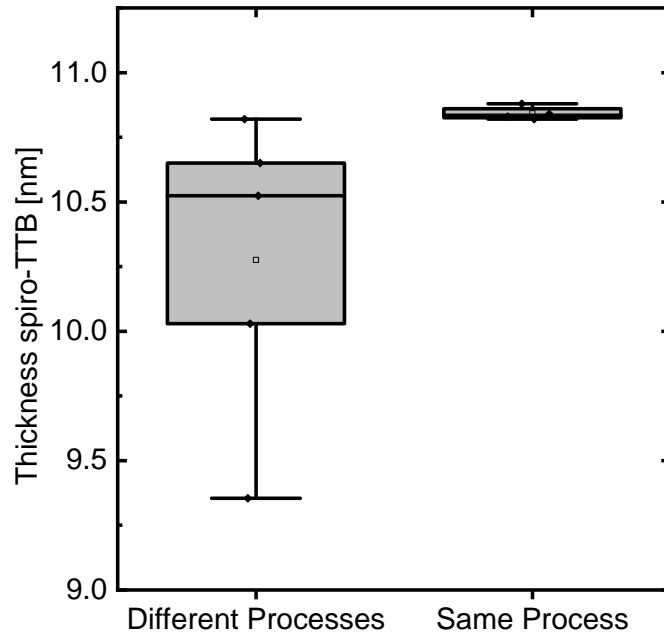


Figure 2.9: Thickness variation of spiro-TTB for samples from several processes (left) and one process (right).

## 2.2.4 Perovskite deposition

For the perovskite  $\text{MAPbI}_3$  we need to co-evaporate both MAI and  $\text{PbI}_2$ . After preheating both materials the  $\text{PbI}_2$  is set to a fixed rate (typically  $1.08 \text{ \AA}/s$ ), similar to the contact layers. For MAI we perform experiments with both a fixed rate (rate controlled), as well as a fixed crucible temperature (temperature controlled) during the deposition. The overall layer thickness is controlled by the total amount of deposited  $\text{PbI}_2$ , which is typically 300 nm to get a perovskite layer with a thickness of about 500 nm. We use substrate temperatures of  $70 \text{ }^\circ\text{C}$  and  $25 \text{ }^\circ\text{C}$  for the rate controlled processes. For the temperature controlled processes we use a substrate temperature of  $25 \text{ }^\circ\text{C}$ . For pure  $\text{PbI}_2$  layers the inner samples are  $1.029 \pm 0.001$  times thicker than the outer samples. This is different compared to the contact layers. The most likely cause for this is that the angle of the crucible of  $\text{PbI}_2$  is different in respect of the sample holder compared to the other crucibles, leading to a more homogeneous layer thickness. The resulting perovskite layers for  $\text{MAPbI}_3$  are approximately 1.1 to 1.15 times thicker for the inner samples compared to the outer samples, however we have only anecdotal references for that and did no systematical investigations.

In chapter 3 we will look at the stability and reproducibility of the perovskite deposition as well as several properties of our perovskite layers.

## 2.2.5 Cell area, series resistance and upscaling of perovskite solar cells

Most perovskite single junction solar cells that are deposited on a glass substrate use a full area TCO for charge transport of one type of carrier. The typical cell areas of these types of solar cells are below  $1 \text{ cm}^2$  and increasing the cell size leads to a loss in fill factor due to sheet resistance in the TCO [93]. As an example we will look at cell type with full area ITO with the ITO we use in our solar cells here.

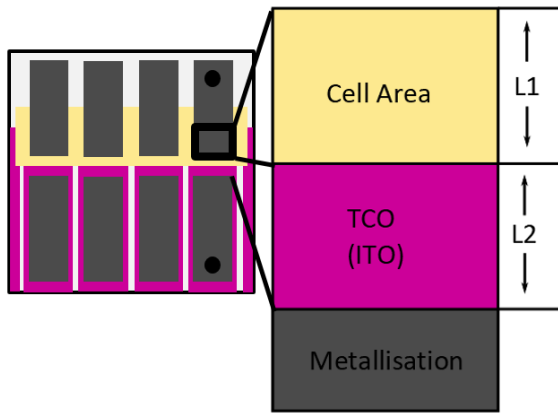


Figure 2.10: Pathway of charge carriers through ITO for a perovskite solar cell as processed in this work.

The series resistance in the ITO can be separated into two terms: the series resistance contribution of the ITO in the cell area (with length  $L1$ ) and the ITO width between cell area and metallisation (with length  $L2$ ), as can be seen in Figure 2.10. The contribution of the sheet resistance in ITO to the series resistance of a perovskite solar cell can be calculated similarly to the finger or emitter resistance of a silicon solar cell [98, 99]. A step by step derivation

of the formula we use here can be found in the appendix.

The series resistance contribution to our solar cells in ITO  $R_{S,ITO}$  can be described with the length  $L1$ ,  $L2$  and the sheet resistance of ITO  $R_{ITO}$ .

$$R_{S,ITO} = \left(\frac{L1}{3} + L2\right) \cdot L1 \cdot R_{ITO} \quad (2.1)$$

Since you want to maximize the active cell area, you would need the length  $L1$  to be much larger than the area fraction of  $L2$  and the metallisation. There needs to be some spacing  $L2$  to separate the cell contact. However you want  $L2$  to be as small as possible without short-circuiting the solar cell. For ITO with  $R_{ITO} = 8.4 \text{ Ohm/sq}$  (the ITO we use here), Table 2.2 shows  $R_{S,ITO}$  for different lengths  $L1$  and  $L2$ . In our cells we have  $L1 = 0.3 \text{ cm}$  and  $L2 = 0.2 \text{ cm}$ .

We can see that just the ITO series resistance contribution in solar cells with our size limitations which is  $0.756 \text{ Ohmcm}^2$  is higher than the overall series resistance of an industrial PERC solar cell, which is below  $0.6 \text{ Ohmcm}^2$  [100]. Further increasing the cell length  $L1$  leads to unreasonable high series resistances. In our

## 2.2. CELL GEOMETRY AND PROCESSING IN THIS WORK

$R_{S,ITO}$ [Ohmcm <sup>2</sup> ]	$L1=0.3$ cm	$L1=1$ cm	$L1=10$ cm
$L2=0$ cm	0.252	2.8	280
$L2=0.1$ cm	0.504	3.64	288.4
$L2=0.2$ cm	0.756	4.48	296.4

Table 2.2: Series resistance in ITO  $R_{S,ITO}$  in Ohmcm<sup>2</sup> for different cell sizes  $L1$  and  $L2$ .

case, since the ITO width is wider (0.6 cm) than the cell area (0.4 cm), the actual series resistance contribution from ITO would only attribute to about 2/3 of the amount in Table 2.2, but is still considerable, especially since the cell area is so small (0.12 cm<sup>2</sup>). Increasing not the length but the width of the cell stripe would have no effect on the series resistance contribution in ITO, making this approach suitable for lab-scale mini-modules [92]. The still needed metal fraction and TCO length  $L2$  is however limiting this solar cell design to more of a proof of concept type device than for actual commercial use.

PSCs on glass (or a flexible transparent foil) with metal contacts on the front side deposited between ITO and glass are developed as well. Currently, these types of solar cells are still much smaller (typically <100 cm<sup>2</sup>) and less efficient (<20%) than industrial-type silicon solar cells [101].

The tandem-approach with a silicon solar cell as a substrate is to this date much more promising in terms of efficiency and area. Oxford PV demonstrated a 200 cm<sup>2</sup> solar cell with a PCE of over 26% at HOPV 2021 [102], greatly exceeding the efficiencies of large area perovskite solar cells on a glass substrate.

The here presented small-sized (0.12 cm<sup>2</sup>) perovskite solar cells on a glass substrate are therefore mostly a development step towards a perovskite-silicon tandem solar cell [103].

### 2.2.6 Encapsulation

As discussed before, perovskite layers and devices are prone to degradation due to moisture and oxygen in ambient atmosphere. To protect the perovskite layer various methods of encapsulation have been published [104]. To protect our lab scale samples here we seal the samples inside a glovebox with an UV-curable glue (Blufixx) and a cover slip, which is shown in Figure 2.11. This exact encapsulation method is used by HZB as well, which currently hold the world record for the highest efficiency perovskite-silicon tandem solar cells [2, 105].

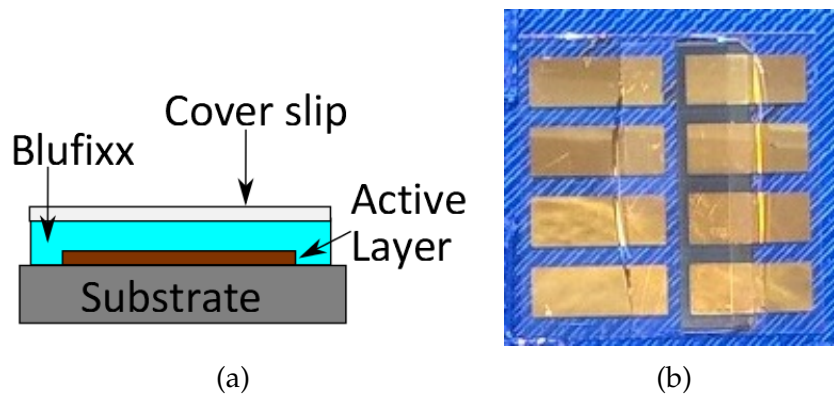


Figure 2.11: (a) Cross section scheme of perovskite encapsulation with Blufixx and a cover slip (b) Encapsulated perovskite solar cell at ISFH.

# 3 Perovskite properties

This chapter will explain the progress made at ISFH in the deposition of MAPbI<sub>3</sub> from around mid-2019 to the beginning of 2022. This chapter features also some basic properties of the deposited perovskite layers with non-cell measurements.

## 3.1 Perovskite processing

### 3.1.1 Impact of substrate temperature

As introduced in the last chapter, we deposit the perovskite layer MAPbI<sub>3</sub> by co-evaporation of MAI and PbI<sub>2</sub>. In 2018, there were several publications made by ISFH about a rate controlled co-evaporation with substrate temperatures of 60 °C or 70 °C [106, 107]. At that point, we had no working perovskite solar cells made at ISFH (in hindsight due to a combination of perovskite properties and cell designs where we short-circuited our solar cells during contacting), which made the evaluation of the process on a cell level difficult. We chose a substrate temperature of 70 °C due to concerns about the perovskite formation because wet-chemical processed perovskites need an annealing step after deposition. In 2019 and beginning of 2020, several groups reported promising cell results as well as good perovskite properties with a substrate at room temperature[94, 108].

Reducing the substrate temperature leads to an increased incorporation of MAI into the perovskite, whereas the PbI<sub>2</sub> incorporation is stable [84]. For the rate controlled processes, we have to decrease the evaporation rate of the MAI crucible from 0.35 to 0.12 Å/s to achieve a similar perovskite thickness of about 500 nm when we reduce the substrate temperature from 70 °C to 25 °C. In our experiments, the MAI consumption in the MAPbI<sub>3</sub> co-evaporation decreases from about 1.4 g to 0.3 g for this reduction in substrate temperature, as is shown in Figure 3.1. We can also see, that the amount of consumed MAI in the respective groups is not stable.

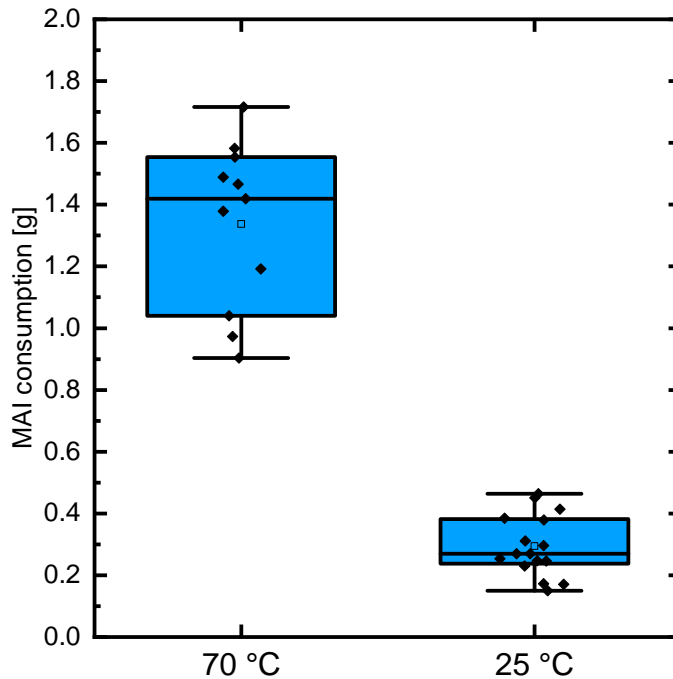


Figure 3.1: MAI consumption for the rate controlled deposition of 500 nm  $\text{MAPbI}_3$  at 70 °C and 25 °C substrate temperature.

### 3.1.2 MAI properties

In the processes shown in Figure 3.1 we refill the MAI crucible when it is nearly empty and we use the material for several processes, as is common for vacuum deposition. Borchert et. al however showed that impurities in the MAI affect the deposition properties and MAI ages (= decomposes) when used for several consecutive depositions [88].

The amount of MAI consumed in the processes directly after filling in new MAI in the crucible is lower than in our average processes as well, as is shown exemplarily in Figure 3.2. To avoid the uncertainty from the MAI properties we adapt from refilling the MAI crucible to using fresh MAI in every process and discard the remaining used MAI in the crucible after the perovskite deposition, which is common by now [91].

We have also changed from a rate controlled to a temperature controlled process for MAI because of promising results from other groups [109] as well as some practical benefits with our deposition tool. The MAI we use is typically made at ISFH in batches of 10 or 20 grams [107]. If we compare similar processes with different batches of MAI we can see that the evaporation properties of MAI change with different batches. Figure 3.3 shows the MAI consumption of temperature controlled processes from three ISFH-made batches of MAI, all with a constant



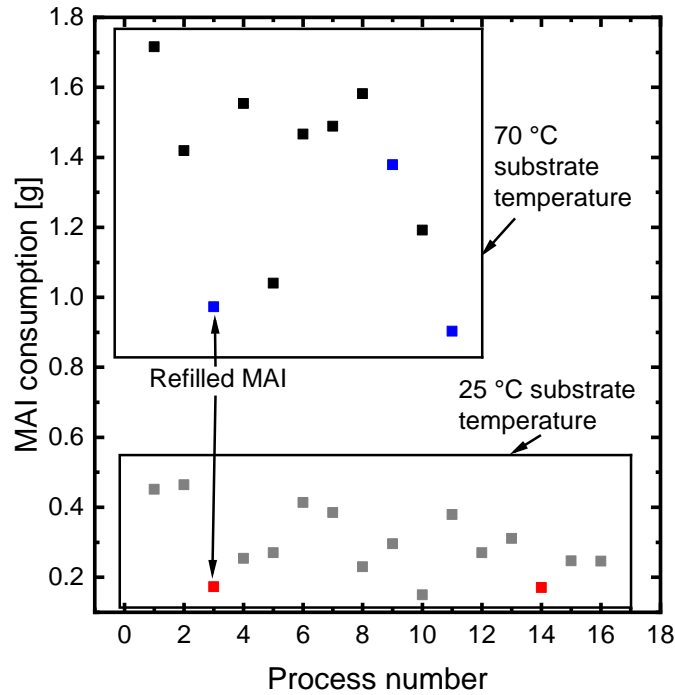


Figure 3.2: MAI consumption for several consecutive depositions at 70 °C and 25 °C substrate temperature. The processes where we refilled the MAI crucible prior to the deposition are marked in red and blue.

crucible temperature for MAI of 118 °C during the deposition. We can clearly see that the MAI consumption is higher in batch 2 compared to 3 and 4, which are relatively similar to each other. The difference is that for the preparation of MAI at ISFH, a different bottle of hydrogen iodide was used in batch 1 and 2 compared to 3 and 4, which were prepared shortly after each other from the same source materials.

Comparing our MAI to one we purchased from Lumtec, which is used from several groups that report high efficiency solar cells [84, 39], we see even clearer differences in the amount of evaporated MAI in respect to the crucible temperature, as is shown in Figure 3.4. Additionally, the amount of evaporated MAI changes by more than 100% from process to process, even for similar MAI crucible temperatures and MAI batches. So far I have only shown the MAI consumption during the processes, not perovskite layer properties by itself. As we have a fixed  $\text{PbI}_2$  thickness of 300 nm in every process, which is measured with the QCM above the  $\text{PbI}_2$  crucible, the resulting perovskite layer thickness should mainly be influenced by the amount of incorporated MAI during the process.

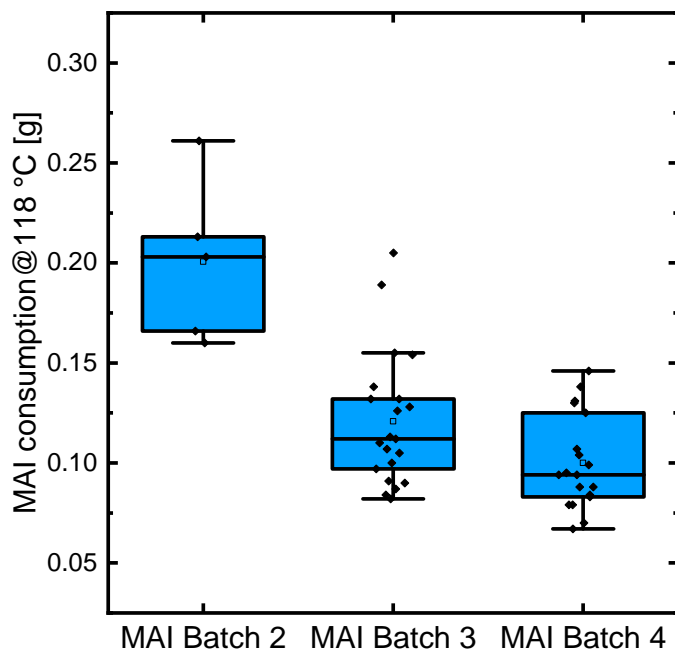


Figure 3.3: MAI consumption for a temperature controlled deposition with a MAI crucible temperature of 118 °C for MAI Batch 2, 3 and 4.

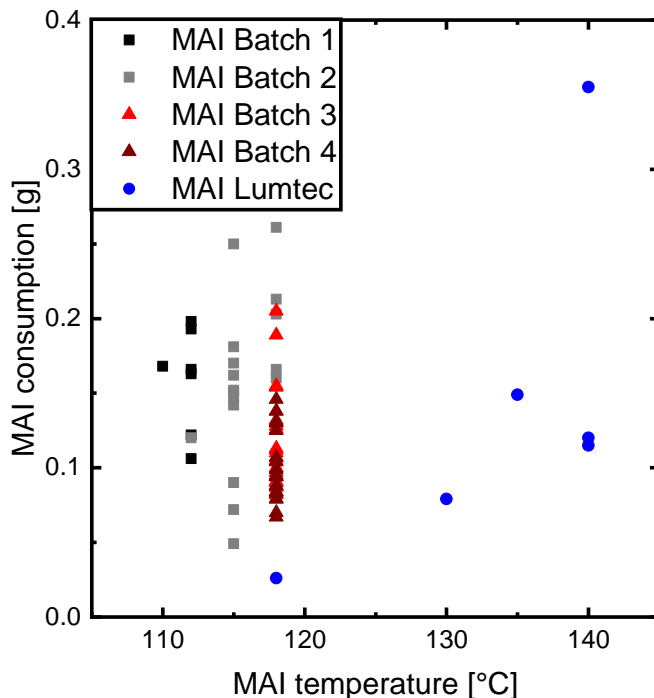


Figure 3.4: Temperature dependent MAI consumption for MAI Batch 1, 2, 3 and 4 and MAI from Lumtec for several processes with a MAI crucible temperature ranging from 110 to 140 °C.

We therefore determine the perovskite film thickness of several processes with either SEM, ellipsometry or from optical simulations (see chapter 5) of the measured spectral reflection of solar cells and compare the measured thickness to the MAI consumption. Figure 3.5a shows the comparison of the film thickness to MAI consumption for perovskite layers made with different batches of MAI from ISFH and MAI from Lumtec. We can see that for the groups of MAI Batch 1+2 and MAI Lumtec the layer thickness increases with increasing MAI consumption, but with a different slope for each batch. For MAI Batch 3+4, the MAI consumption is however not related to the layer thickness for most processes. This result implies, that not only the amount of MAI evaporated in each process is heavily influenced by the properties of the MAI, but also the incorporation into the perovskite film. To investigate if these changes can be mitigated by using a rate controlled process we compare the measured film thickness to the monitored MAI thickness on the quartz crystal, which we still monitor even for the temperature controlled processes. In Figure 3.5b we can see, that for MAI Batch 1+2 and MAI Batch 3+4 the measured film thicknesses generally increase with increasing thickness measured on the QCM. We still see variations in the ratio of measured to monitored film thickness in each group and even bigger differences between both groups. Therefore using a rate controlled process would still result in a thickness variation of the perovskite film, even when using fresh MAI from one batch.

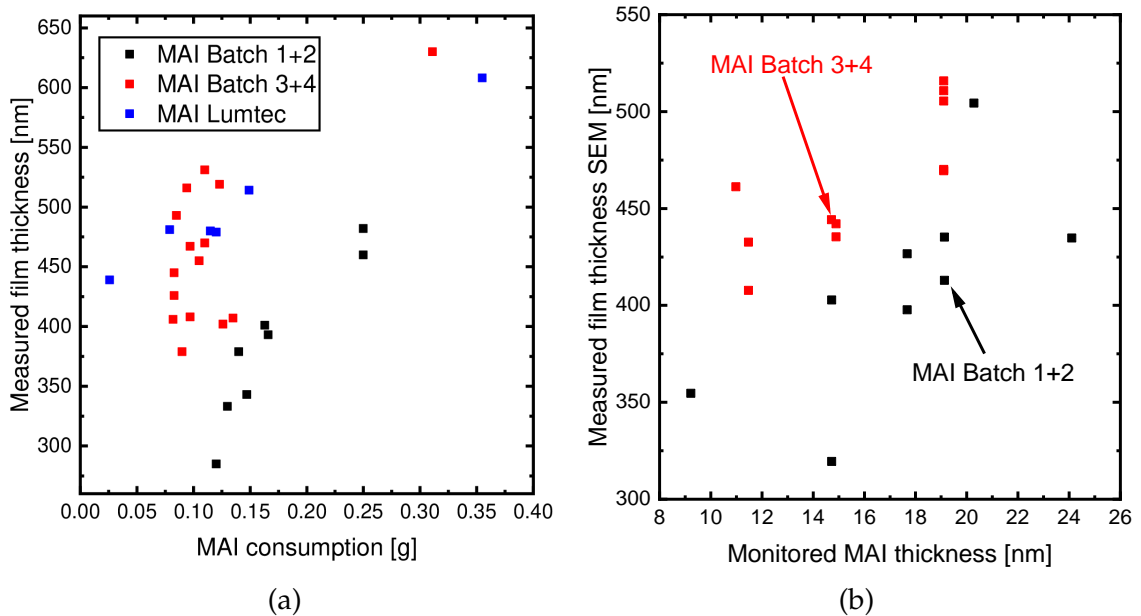


Figure 3.5: (a) Perovskite layer thickness in dependence of the MAI consumption for different batches of MAI. (b) Measured film thickness with SEM versus measured thickness on the MAI QCM.

### 3.1.3 Cross-Contamination

What further complicates the reproducibility of the process is the thickness measurement of  $\text{PbI}_2$ . As mentioned in section 2.2.4, the overall layer thickness is controlled by having a fixed deposition rate of  $\text{PbI}_2$  (typically  $1.08 \text{ \AA}/s$ ) and a fixed thickness of  $\text{PbI}_2$  (300 nm) in every process, which is monitored with a QCM. Since we deposit two materials simultaneously, it is important to block all MAI from reaching the  $\text{PbI}_2$  QCM for an accurate thickness measurement. We aim to achieve this by a metal shielding between the  $\text{PbI}_2$  and MAI crucible (schematically drawn in Figure 3.6). This blocks all material that is directly evaporated.

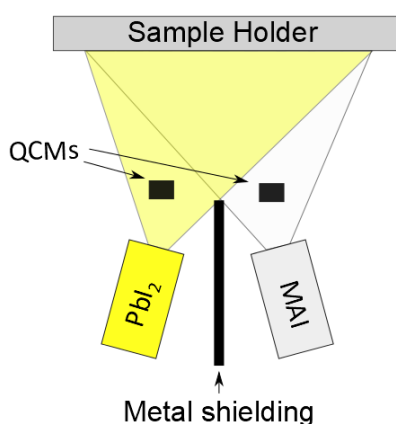


Figure 3.6: Schematic view of the metal shielding between the MAI and  $\text{PbI}_2$  crucible.

$\text{PbI}_2$  is deposited onto the  $\text{PbI}_2$  QCM (as well as the samples) when we evaporate from the  $\text{PbI}_2$  crucible. As soon as some MAI was deposited in the chamber, all following processes with  $\text{PbI}_2$  contain varying amounts of MAI (and form a perovskite), as can be seen from the color of the films, shown in Figure 3.8. Pure  $\text{PbI}_2$  has a distinct yellow color. Thin films containing  $\text{PbI}_2$  have a brownish color and thicker films are black even for pure  $\text{PbI}_2$  evaporations when MAI was evaporated prior. Figure 3.7b shows our evaporation chamber after MAI had been evaporated, showing that all areas where  $\text{PbI}_2$  coats the chamber (as can be seen Figure 3.7a) have completely turned black. Figure 3.7c shows the QCM of  $\text{PbI}_2$  after a co-evaporation process, showing that a perovskite layer is formed on the QCM as well.

This is the reason why several groups have developed systems that either minimize the diffuse evaporated MAI [84], or try to deal with the diffuse evaporation by adding additional QCMs [39] or tracking of the background pressure [90].

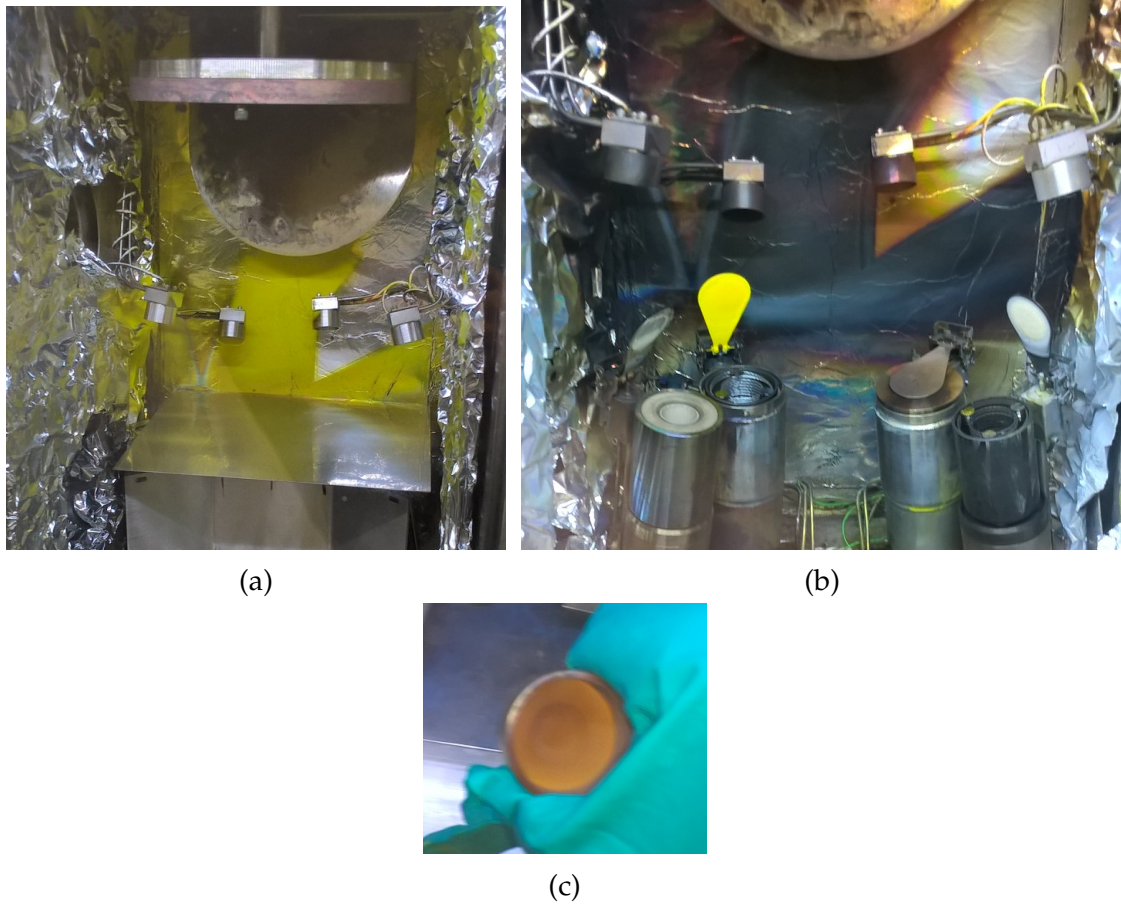


Figure 3.7: (a) Evaporation chamber after  $\text{PbI}_2$  deposition. The areas where  $\text{PbI}_2$  coats the chamber are clearly visible in yellow and have distinct edges, showing the direct path of the evaporated material. (b) Evaporation chamber after MAI (right crucible) and  $\text{PbI}_2$  (2nd crucible from left) were deposited prior. Only the crucible shutter of the  $\text{PbI}_2$  is not coated with MAI (yellow). All other parts where  $\text{PbI}_2$  attaches to the chamber have formed a perovskite layer (black). (c) QCM of the  $\text{PbI}_2$  crucible, showing a brownish color after co-evaporation.

There are reports of evaporated  $\text{MAPbI}_3$  solar cells with above 20% efficiency, that only use a temperature controlled process without any specialised chamber design [19].

All of these reports however do not feature the reproducibility of their process in terms of the perovskite thickness or resulting film stoichiometry. Additionally, all have in common that the contact layers are not deposited in the same chamber as the perovskite, likely to avoid contaminating the contact layers with MAI.

In the processes with MAI-Batch 1+2 we determined the tooling factor of  $\text{PbI}_2$  in an already MAI contaminated state, so that not only  $\text{PbI}_2$  but  $\text{PbI}_2$  and  $\text{MAPbI}_3$  were detected with the QCM. This likely caused a mistake in the tooling factor for  $\text{PbI}_2$ , leading to an overestimation of the  $\text{PbI}_2$  thickness and a lower overall layer

thickness of MAI-Batch 1+2 compared to the other groups shown in Figure 3.5a. Currently we use a temperature controlled perovskite deposition process at a substrate temperature of 25 °C. For processes with the same processing conditions the perovskite layer thickness varies in a range of approximately  $\pm 10\%$  of the average layer thickness, with a varying ratio of  $\text{PbI}_2$  to MAI. Some tolerance of the  $\text{PbI}_2$  to MAI ratio is reported for similar  $\text{MAPbI}_3$  solar cells with 16 to 20% efficiency [20, 39]. Since the ratio of  $\text{PbI}_2$  to MAI and film thickness heavily affects the current output of a thin film solar cell (see chapter 5.3.1), the precise control of perovskite thickness and  $\text{PbI}_2$  to MAI ratio is however crucially important for two-terminal tandem solar cells, that require current matching between top and bottom cell and solar modules because of the series connection in a module.

### 3.2 Influence of $\text{PbI}_2$ to MAI ratio

Although we do not know the exact ratio of  $\text{PbI}_2$  to MAI in each perovskite layer, a relative distinction of the amount of MAI in each sample is already visible to the eye. As is shown in Figure 3.8, for an approximately 300 nm thick  $\text{PbI}_2$  layer with varying amounts of MAI on a glass substrate the sample color changes from yellow (pure  $\text{PbI}_2$ ) to brown ( $\text{PbI}_2$  rich  $\text{MAPbI}_3$ ) to black (stoichiometric  $\text{MAPbI}_3$ , equal amount of MAI to  $\text{PbI}_2$ ). For MAI excesses, the samples start to turn dull and grey once exposed to air (or for high amounts even inside the glovebox). The dull surface on the MAI rich samples is caused by roughness [111, 112].

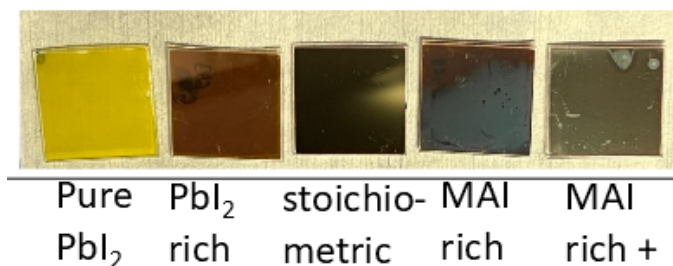


Figure 3.8: Color change of perovskite layers with 300 nm of  $\text{PbI}_2$  with varying amounts of MAI.

As already discussed in chapter 2.1.4, MAI is hydrophilic and perovskites with free MAI draw moisture during air exposure [70]. The dull surface of our MAI rich perovskites is likely formed by the incorporation of water into the perovskite as well. To further investigate this and other properties of the perovskite, we perform XRD measurements to analyse the crystal properties of the perovskite layers. We also use SEM measurements for a further look into roughness and grain



## 3.2. INFLUENCE OF $\text{PbI}_2$ TO MAI RATIO

size of the perovskite crystals as well as photoluminescence (PL) to determine how the properties measured with XRD and SEM influence the band gap and recombination. XRD measurements were performed using a Empyrian diffractometer from Malvern Panalytical with  $\text{Cu K}\alpha$  radiation in  $\theta$ - $2\theta$  configuration, SEM measurements with a Hitachi SEM with 2 keV incident electron beam energy and PL measurements using a Labram HR Evolution from Horiba with an incident photon energy of 633 nm. Additionally in chapter 5, I will show ellipsometry measurements to measure the complex refractive indices of  $\text{PbI}_2$  rich perovskite layers and I also perform optical simulations for perovskite solar cells with varying layer thicknesses and amounts of  $\text{PbI}_2$  excess.

### 3.2.1 Crystal properties and hydrate formation in $\text{MAPbI}_3$

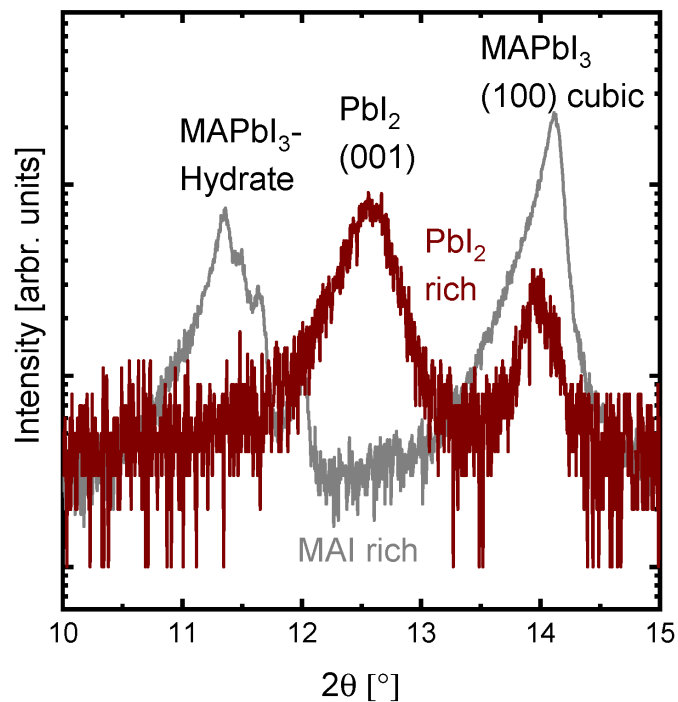


Figure 3.9: Diffractogramm of a  $\text{PbI}_2$  rich (dark red), as well as a MAI rich (grey) perovskite layer.

If we take a look at the x-ray diffraction patterns of MAI rich (grey) and  $\text{PbI}_2$  rich (dark red) perovskite films, which are displayed in Figure 3.9, the  $\text{PbI}_2$  rich perovskite films show peaks at a diffraction angle  $2\theta$  of  $12.5^\circ$  and  $14^\circ$ , coming from the  $\text{PbI}_2$  (001) and cubic  $\text{MAPbI}_3$  (001) crystal plane [51, 113]. MAI rich perovskites do not have the  $\text{PbI}_2$  peak, but do contain a number of peaks around  $11.5^\circ$ . These originate from a dihydrate of  $\text{MAPbI}_3$  ( $(\text{CH}_3\text{NH}_3)_4\text{PbI}_6 \cdot 2\text{H}_2\text{O}$ ) [114].

Since we perform the XRD measurements in ambient atmosphere, these hydrate phases confirm that the MAI rich perovskite film does in fact incorporate moisture once exposed to air.

Although the diffraction pattern of  $\text{PbI}_2$  rich perovskite films contains a  $\text{PbI}_2$  and a  $\text{MAPbI}_3$  peak, the absolute and relative intensities of both peaks differ from deposition to deposition and are also at least partially substrate dependent.

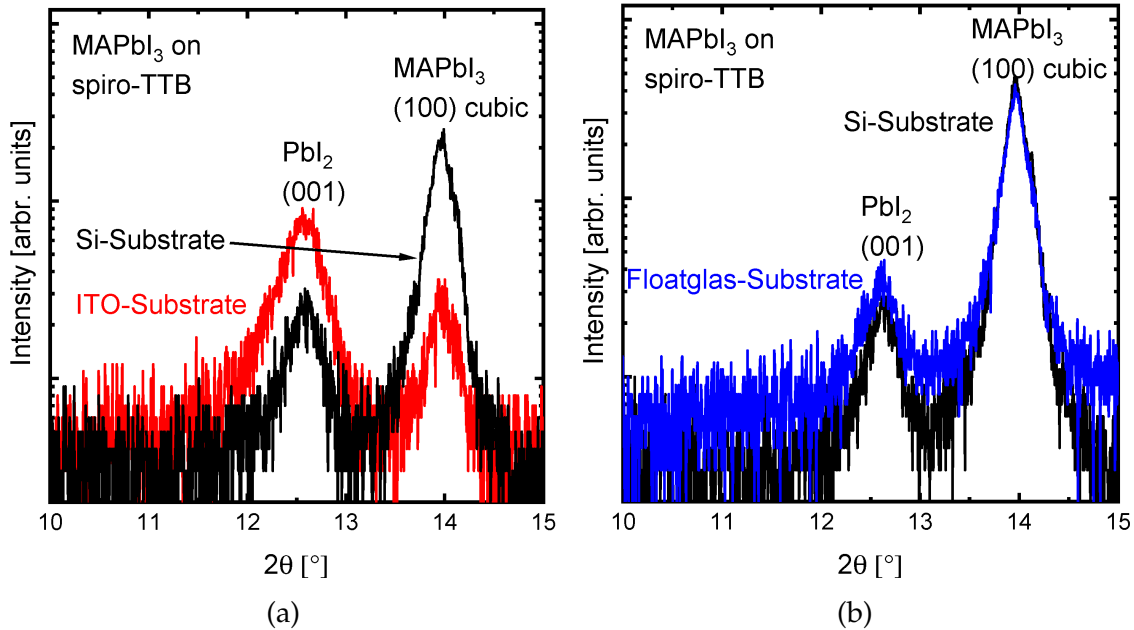


Figure 3.10: Diffractogramm of perovskite layers from the same deposition on top of spiro-TTB on a silicon (Si) and (a) ITO-coated glass or (b) float glass substrate.

Figure 3.10a and Figure 3.10b each show two samples from the same evaporation of  $\text{MAPbI}_3$ , where we first deposited spiro-TTB and then  $\text{MAPbI}_3$ . Although we evaporated all  $\text{MAPbI}_3$  layers on top of spiro-TTB, the substrate still has an effect on the peak height of the  $\text{PbI}_2$  and  $\text{MAPbI}_3$  reflexes for the silicon compared to the ITO substrate displayed in Figure 3.10a. Figure 3.10b shows no difference of the XRD diffraction pattern for a silicon and a float glass substrate. For the same substrate material, the diffraction peaks typically do not differ for one perovskite deposition. For the absolute height or ratio of both the  $\text{PbI}_2$  as well as the  $\text{MAPbI}_3$  peak we do not find any clear correlation related to the amount of  $\text{PbI}_2$  excess, the substrate, or other perovskite properties like grain size, photoluminescence or solar cell parameters.

$\text{PbI}_2$  is reported to form at grain boundaries [79], but to which parts it is crystalline or amorphous and how this affects cell performance is still heavily discussed [77, 67, 91].



### 3.2.2 Morphology and grain size of $MAPbI_3$

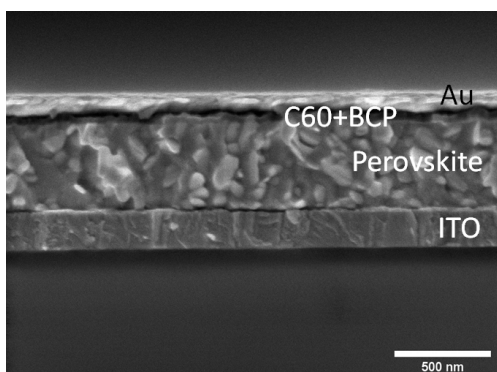


Figure 3.11: Cross section of a typical perovskite solar cell in the SEM.

For a more in-depth look at the morphology of the perovskite layer we use scanning electron microscopy (SEM) imaging to investigate the cross section of our films. Although many groups try to aim for large grain sizes, especially for wet-chemically processed perovskite solar cells [115], several publications also claim that recombination at grain boundaries is not a limiting factor for perovskite solar cells [46]. Whether or not the morphology measured with SEM affects the

optoelectronic properties of the perovskite at all is still in debate [116].

A typical cross section of one of our perovskite solar cells is displayed in Figure 3.11. The perovskite is deposited on top of the ITO (between perovskite and ITO is 10 nm spiro-TTB, which is not visible in the SEM image) and has a polycrystalline morphology. On top of the perovskite is the ETL (23 nm C60 and 8 nm BCP) as well as the electrode (60 to 100 nm Au).

For perovskites with varying amounts of  $PbI_2$  excess, we observe an increase in grain size of the perovskite layer with increasing MAI content as displayed for three perovskite solar cells in Figure 3.12. A similar behaviour for evaporated perovskite layers has been reported by Roß et al. recently [83]. A mechanism for bigger grains with increasing MAI content could be that  $PbI_2$ , that is located at the grain boundaries, gets incorporated into the perovskite grains when more MAI is present.

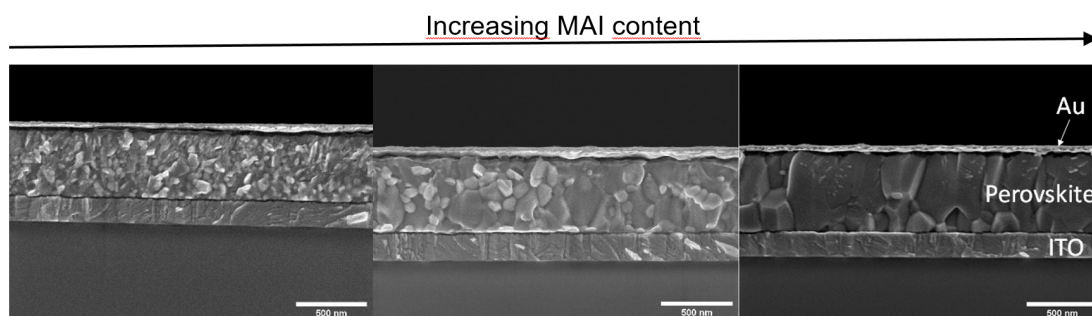


Figure 3.12: Perovskite layer with high (about 50%  $PbI_2$ , left) and low (about 15%  $PbI_2$ , middle) excess of  $PbI_2$  as well as a stoichiometric  $MAPbI_3$  (right) .

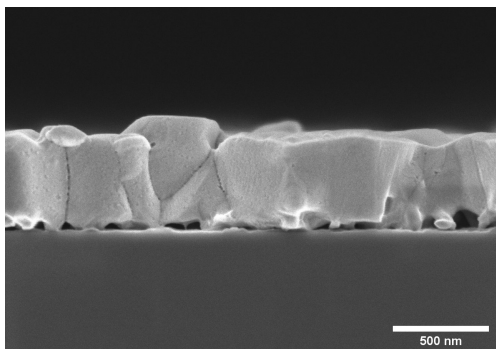


Figure 3.13: Cross section of  $\text{MAPbI}_3$  on a silicon substrate with a slight excess of MAI.

A further increase of the MAI content (MAI excess) leads to even larger grain sizes as we can see in Figure 3.13. During investigation under the electron beam in the SEM these layers start to form small holes, especially at the grain boundaries. If we increase the MAI content even further, to where the layer starts to turn dull when exposed to air, the layer morphology starts to turn rough and bigger holes start to form during exposure in the electron beam, as is displayed in Figure 3.14.

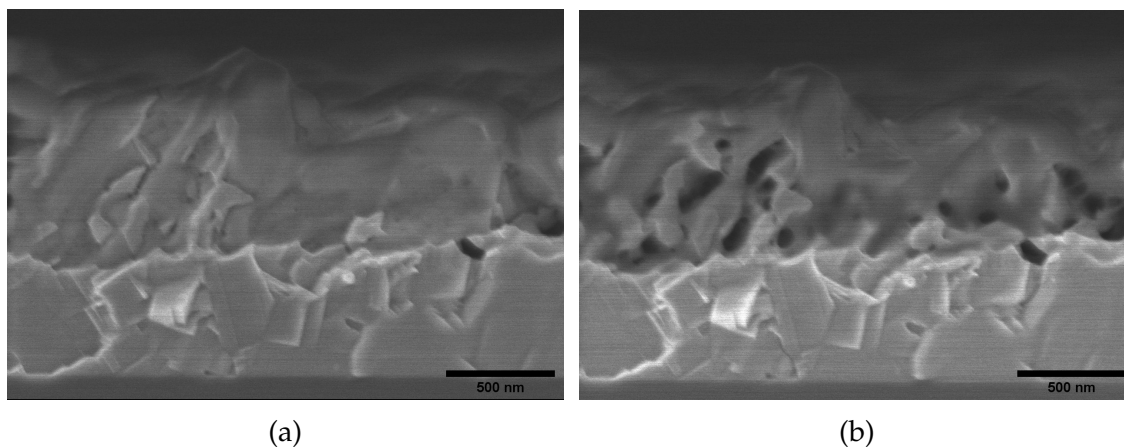


Figure 3.14: Hole formation in a  $\text{MAPbI}_3$  layer on silicon in the SEM. (a) Before and (b) after exposure to the electron beam.

The hydrate formation confirmed with XRD, the dull surface once exposed to air and the formation of holes in the SEM can all be explained by incorporation into and evaporation of water from the perovskite layer. The likely process is, that water diffuses into MAI rich perovskites, which increases the layer volume once exposed to a water source (ambient atmosphere). Thus the surface turns rough and dull. When the perovskite is then brought into a SEM, where an electron beam targets a specific area with a high amount of energy in a vacuum environment, the water inside the perovskite layer evaporates. This causes the hole formation due to the decreasing layer volume of the perovskite.

For the  $\text{PbI}_2$  rich perovskites, we do not detect a formation of holes in the SEM. There are however still variances in the morphology of the perovskite, beyond the

### 3.2. INFLUENCE OF $\text{PbI}_2$ TO MAI RATIO

general grain size distribution shown in Figure 3.12. Figure 3.15 shows the SEM images of two  $\text{PbI}_2$  rich perovskite layers from different depositions. If we look at the crystal size distribution in both perovskites, the perovskite in Figure 3.15a has small grains at the substrate interface and bigger grains at the interface to air as well as a relatively rough surface. The perovskite layer in Figure 3.15b shows the complete opposite behaviour with a decrease in grain size from substrate to surface interface. We currently do not know what causes these differences in morphology.

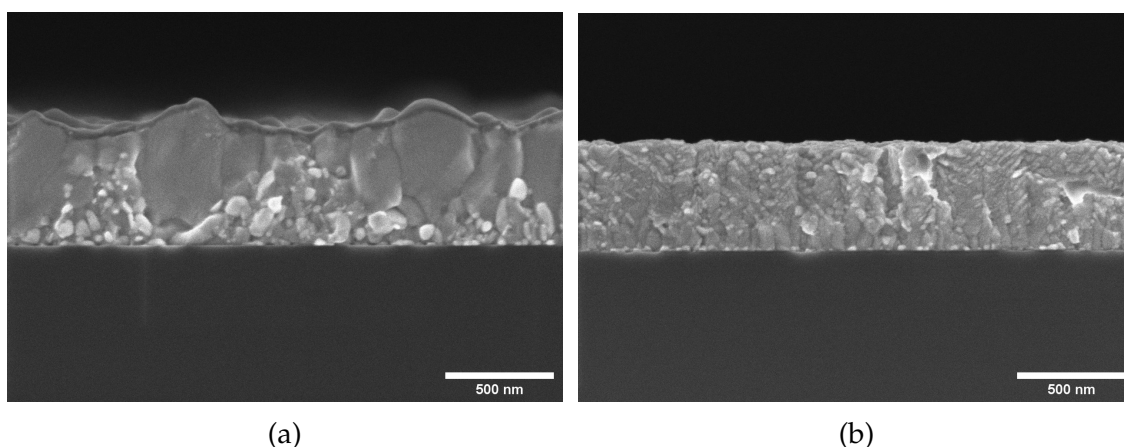


Figure 3.15: Two  $\text{PbI}_2$  rich  $\text{MAPbI}_3$  layers on silicon from different deposition processes.

If we look at two  $\text{PbI}_2$  rich perovskites from the same deposition, the perovskite layers typically look relatively similar, as can be seen in Figure 3.16 (a) and (b) for two perovskite solar cells from the same deposition process. Both samples were measured as a solar cell in air prior to the SEM measurement.

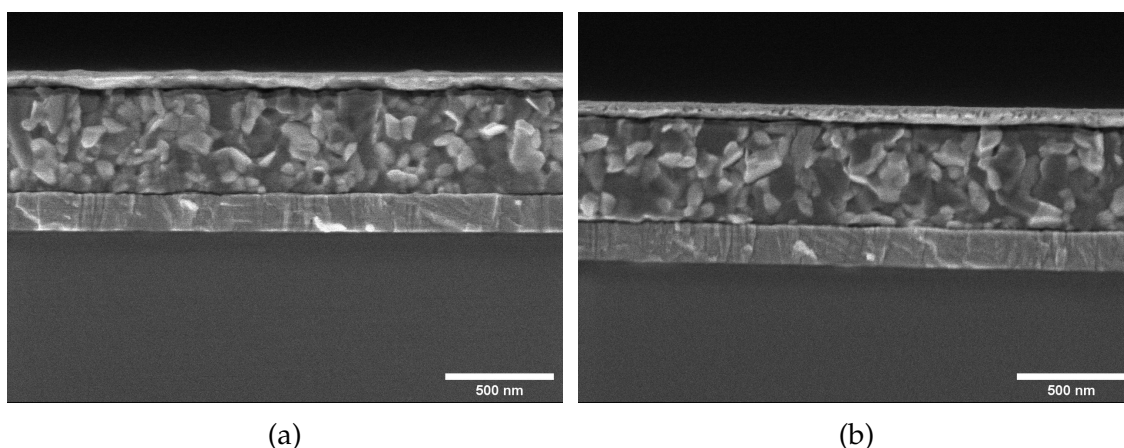


Figure 3.16: Two  $\text{PbI}_2$  rich perovskite solar cells from the same deposition.

An example that the measurement itself can have an effect on the morphology of the perovskite is presented in Figure 3.17. Here, we can see two  $\text{PbI}_2$  rich per-

ovskite solar cells from the same deposition processes, both after being measured as a solar cell in air, as in the example above. Not only is the grain size of the perovskite layer in Figure 3.17b bigger compared to Figure 3.17a, but the actual layer thickness has increased as well (from around 480 to 550 nm). We can also see a void formation at the perovskite/ITO interface at Figure 3.17b, which is not changing under electron beam exposure, contrary to the holes in the MAI rich films and likely not caused by water incorporation. This change in morphology was likely caused by negative bias voltages which were applied to the solar cell in Figure 3.17b. The impact of negative bias voltages on our solar cells was investigated in the master thesis of Max Richter [117]. These measurements demonstrate that even for perovskites without MAI excess the morphology of the perovskite layer is altering between different perovskite depositions and can change even after the deposition.

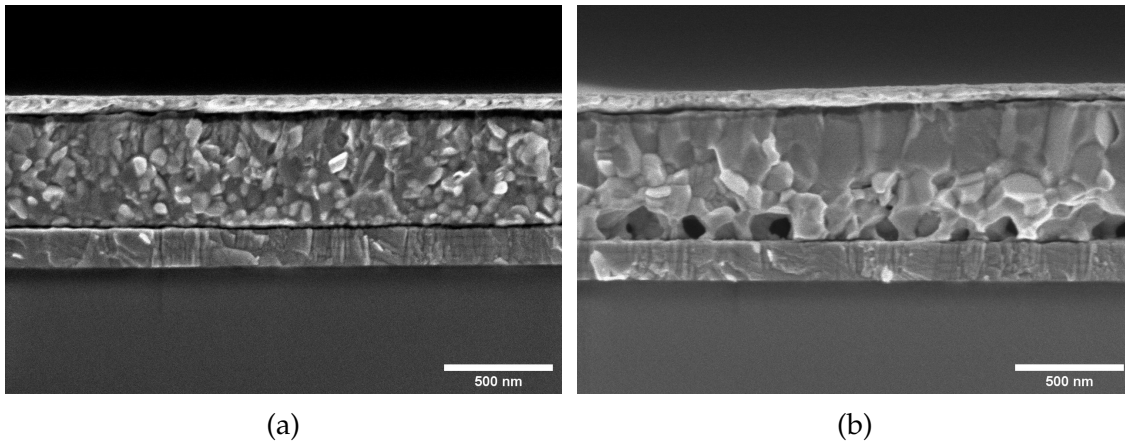


Figure 3.17: Two  $\text{PbI}_2$  rich perovskite solar cells from the same deposition, with (b) being negatively biased prior to the SEM investigation.

### 3.2.3 Photoluminescence and recombination

In addition to the morphology and crystal properties as well as the complex refractive index (see chapter 5) we can investigate the photoluminescence (PL) of our perovskite layers. This gives us insight into the amount of radiative recombination in the perovskite. There is a distinction between photoluminescence measurement methods, one is to measure the wavelength-dependent intensity, the other to measure the time-resolved decay of the intensity called time-resolved photoluminescence (TRPL). The PL intensity and decay time are however related, because both depend on how much non-radiative recombination is occurring in the perovskite layer [118]. In this work, we mainly take a look at the intensity and

### 3.2. INFLUENCE OF $\text{PbI}_2$ TO MAI RATIO

wavelength dependence of the photoluminescence. TRPL measurements for our perovskites with different contact layers are presented in the master thesis of Nils Evert [119]. In the following part, I will explain a few basic photoluminescence properties of  $\text{MAPbI}_3$  perovskite layers that we deposit on silicon substrates.

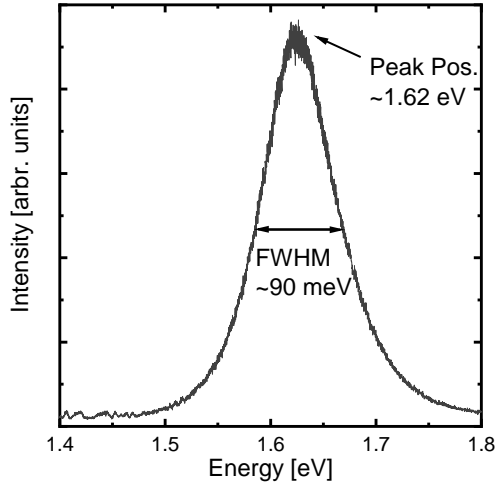


Figure 3.18: Typical photoluminescence spectrum of a  $\text{MAPbI}_3$  layer measured at ISFH.

(MAI/ $\text{PbI}_2$  ratio of 2/1) shows a shift in the peak position from 1.62 to 1.68 eV. In addition, we see that the peak width of the sample with the PL maximum at 1.68 eV is higher than that of the other samples. The peak position shift to higher energies could be explained by a change of the crystal structure in  $\text{MAPbI}_3$  as well as doping similar effects [121, 122]. Additional measurements after storage in the glovebox, which are displayed in Figure 3.19b, show that the PL position and intensity changes after storage, revealing that these layers are not stable at room temperature, even in inert gas atmosphere.

Figure 3.20a shows several photoluminescence spectra of  $\text{PbI}_2$  rich perovskites from different depositions, normalised to the same peak intensity. For perovskites that are  $\text{PbI}_2$  rich, we do not observe a significant shift in the photoluminescence maximum or peak width. The intensity of the photoluminescence differs in several orders of magnitude for perovskites from different processes, as is shown in the non-normalised photoluminescence spectra in Figure 3.20b. Since both the  $\text{PbI}_2$  rich as well as the MAI rich samples show a large variety in terms of luminescence intensity, we currently do not know to which extent the photoluminescence intensity in our samples is related to any other material properties like grain size or  $\text{PbI}_2$  to MAI ratio for example.

A typical  $\text{MAPbI}_3$  photoluminescence spectrum is displayed in Figure 3.18, where we can see a photoluminescence peak with a peak position of around 1.62 eV. In addition, I added the full-width-half-maximum (FWHM), or peak width into this image. The FWHM is an additional information about structural disorder in the material, with higher FWHM resulting from less homogeneous materials [120].

For MAI rich samples, we can see an increase in the intensity of the photoluminescence with increasing MAI content as is shown in Figure 3.19a. One sample

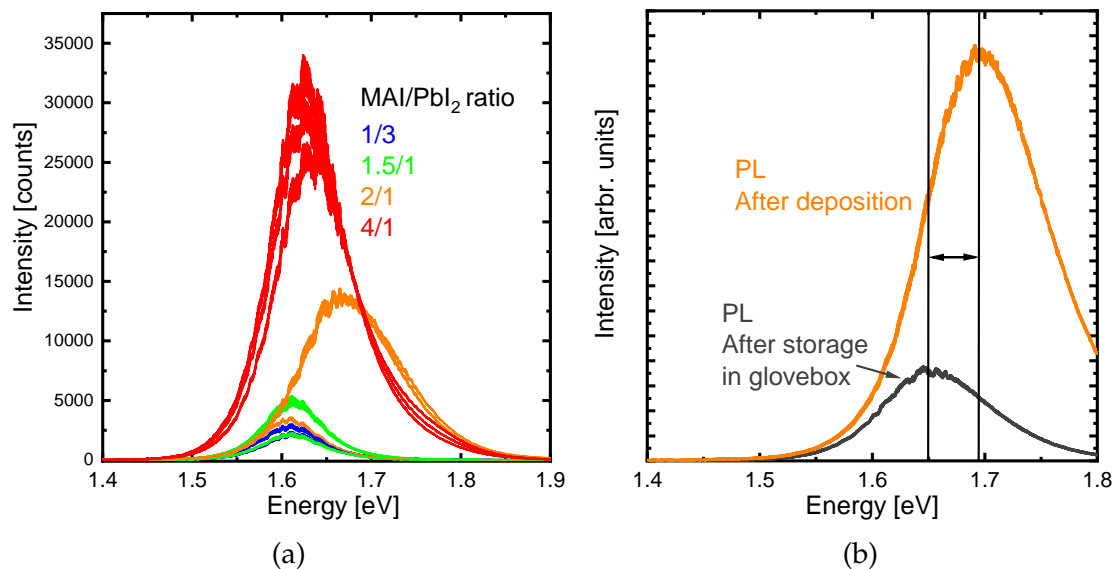


Figure 3.19: (a) PL intensity of MAPbI<sub>3</sub> depositions with a varying PbI<sub>2</sub>/MAI rate ratio during deposition. (b) PL intensity of MAPbI<sub>3</sub> layer with a 2/1 MAI/PbI<sub>2</sub> precursor ratio directly after deposition and after storage in a glovebox for about three weeks.

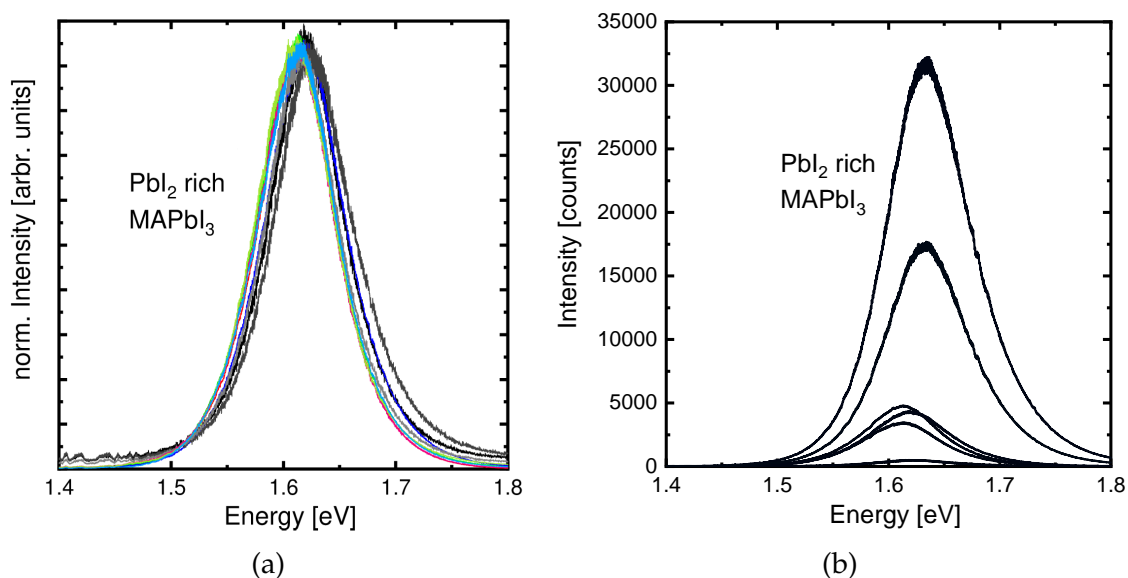


Figure 3.20: (a) Normalised and (b) as measured PL intensity of several depositions of PbI<sub>2</sub> rich MAPbI<sub>3</sub> with similar deposition parameters.

### 3.2. INFLUENCE OF $PbI_2$ TO MAI RATIO

In the following experiment, we use ITO-coated glass and float glass (BF) as substrate and spiro-TTB as well as different self-assembled monolayers (SAMs) [84, 30] as HTL and deposit  $PbI_2$  rich  $MAPbI_3$ . Originally we only wanted to make a qualitative assessment of the interface of several HTLs to our perovskite by measuring the photoluminescence intensity, as proposed by Stolterfoht et al. [47].

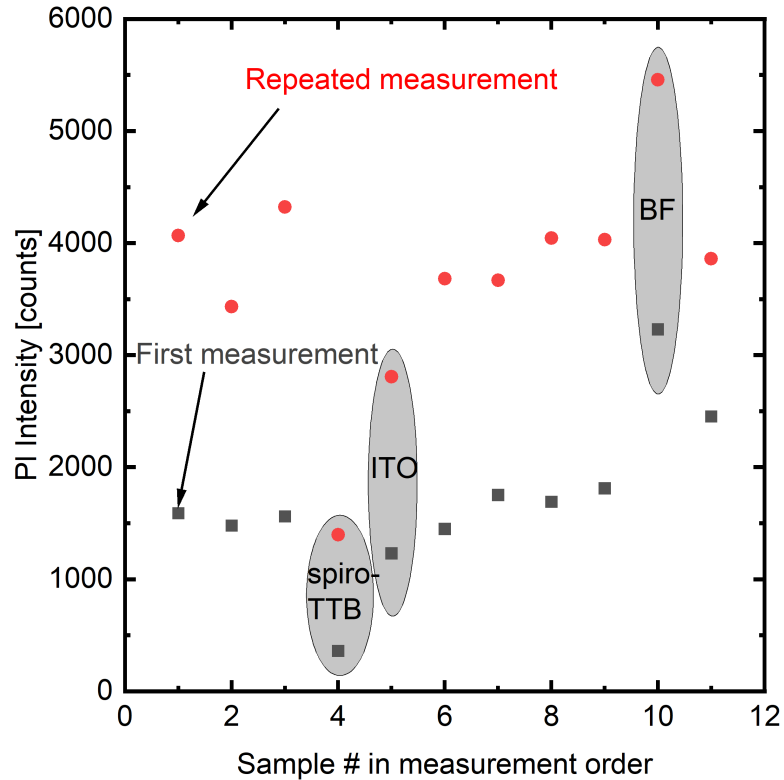


Figure 3.21: PL intensity of  $MAPbI_3$  from one deposition process deposited on ITO, float glass (BF), spiro-TTB or different SAMs (not marked).

Figure 3.21 shows the PL intensity for each sample in the measurement order. After measuring the PL on each sample, which takes about two hours for the twelve samples, we repeat the measurement. The trend of the photoluminescence intensity in our measurements is quite similar compared to published data by Stolterfoht, showing that perovskite on bare floatglas achieves the highest photoluminescence, followed by the SAMs, then the ITO and lastly the spiro-TTB [11]. The reason why the photoluminescence on bare ITO is not the lowest as in the Stolterfoht publication is likely because no good contact between ITO and the perovskite is formed, leading to poor carrier mobility at the interface, similar to BCP on perovskites [34, 40]. The main difference between our samples and the ones in literature is that our layers are evaporated and not annealed and the layers in the

Stolterfoht publication are wet-chemically processed and annealed. This result illustrates the importance of the perovskite and contact layer deposition conditions on important properties for solar cell operation. Similar experiments, showing a decrease of the photoluminescence intensity for perovskite layers deposited on test structures with C60 and spiro-TTB compared to no contact layer, were performed in the master thesis of Nils Evert [119].

The PL intensity of every sample in Figure 3.21 increases from first to repeated measurement, and in many cases more than doubles. The difference between first and repeated measurement is mainly the increased amount of ambient exposure. These results show, that even for  $\text{PbI}_2$  rich perovskites from the same deposition, the photoluminescence intensity is not only influenced by the interface material, but also by exposure to ambient atmosphere.

### 3.3 Summary: Air exposure and reproducibility

For all measurements presented here (XRD, SEM and PL), the measured properties of the perovskite layers from different depositions vary significantly. Even for samples from one deposition we still see differences. These can be caused by aging under ambient atmosphere or from specific prior measurements, especially for MAI rich perovskites but for  $\text{PbI}_2$  rich perovskites as well. In practice, this makes any assessment of specific planned variations (for example variations in the CTL, annealing steps etc.) difficult. Currently, comparing variations between several perovskite depositions is not feasible at all and the perovskite deposition process needs to be improved in future to be more reproducible. For most measurements, the samples are exposed to ambient atmosphere since the measurement tools are not within a glovebox. For some measurements like photoluminescence, reflection or transmission the samples can be encapsulated (see chapter 2.2.6) inside a glovebox, which eliminates at least the factor of air exposure time. This is however not possible for SEM or XRD measurements. For SEM the samples need to be broken, which is not possible once encapsulated (and once broken, the sample surface would still be exposed to ambient atmosphere for some time). In XRD measurements, the x-rays cannot penetrate the encapsulation.



## 4 Cell measurements of PSCs

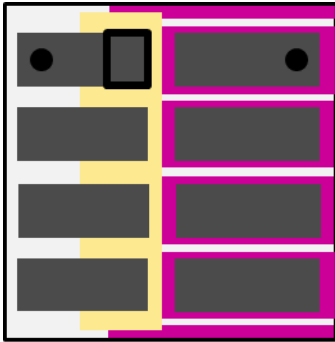


Figure 4.1: Points (black circles) where the PSC is contacted for cell measurement.

So far, I have only discussed the reproducibility of our perovskite deposition process and non-cell perovskite properties. In this chapter I will now explain all relating cell properties in detail, illustrating also how the reproducibility of our deposition processes affects cell performance. Additionally, I will discuss which factors are currently limiting for our cell efficiencies and how to improve them in future. The cell design we use is the one I showed in Figure 2.7 in chapter 2.2.1. We contact each cell at the outer metallisation as is shown with the black spots in Figure 4.1. We illuminate the cell through the glass side to make current-voltage (IV) measurements. Typi-

cally we use a measurement chuck where all four cells on a substrate are simultaneously contacted and separately measured.

Due to some clearance of the masks at the different depositions, the cell area is not exactly  $3 \times 4 \text{ mm}^2$ . To only illuminate a defined area we use a black paper mask that is taped on top of the cell during illumination with an area of approximately  $2 \times 3 \text{ mm}^2$  ( $0.061 \text{ cm}^2$  to be precise). We perform the solar cell measurements with a LOANA system by pvttools in ambient atmosphere.

In most cases I will only show results from the light current voltage (light-IV) measurement of the solar cell, but typically we additionally measure the current voltage characteristics in the dark (dark-IV) and also perform a  $J_{SC}$ - $V_{OC}$  measurement [123]. For some solar cells we also perform differential quantum efficiency as well as reflection measurements to quantify the external and internal quantum efficiency of the solar cell. In the following I will show data of the most important solar cell parameters for specific subsets of our perovskite solar cells, namely short-circuit current density ( $J_{SC}$ ), open-circuit voltage ( $V_{OC}$ ), fill factor ( $FF$ ) and efficiency ( $\eta$ ). These are all directly measured values from the light-IV curve. Figure 4.2 shows a light-IV curve of a perovskite solar cell (PSC).  $J_{SC}$  and  $V_{OC}$  are

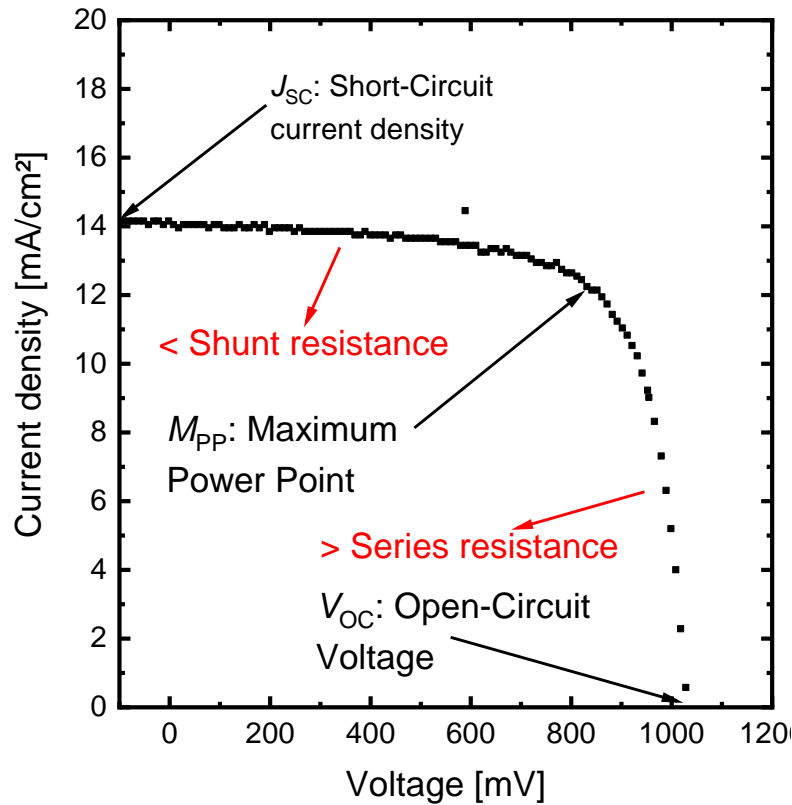


Figure 4.2: Measured light-IV curve of a PSC (black dots) with the most important cell parameters. Black values: Directly measured, Red values: Extracted by fit of the IV curve.

defined where the voltage (or current) is 0 and can be immediately read from the light-IV measurement. The point at which the power output (the product of current  $J$  and voltage  $V$ ) is the highest is called the maximum power point ( $m_{pp}$ ). The fill factor ( $FF$ ) is defined as  $J_{mpp} \cdot V_{mpp} / (J_{sc} \cdot V_{oc})$  and the efficiency  $\eta$  is the maximum power output of the cell  $J_{mpp} \cdot V_{mpp}$  divided by the initial power input of the AM 1.5G sun spectrum (which is defined as  $1000.4 \text{ W/m}^2$ , so about  $100 \text{ mW/cm}^2$ , according to ASTM G173-03).

## 4.1 Cell reproducibility and influence of process conditions

### 4.1.1 Refilled MAI and effect of MAI excess

As explained in 3.1.1 and 3.1.2, initially we used the MAI in the MAI crucible for several processes and only refilled the crucible when it was nearly empty. Figure 4.3 shows the average efficiencies of perovskite solar cells from 9 consecutive perovskite depositions following the above procedure and a rate controlled MAI deposition, as well as the MAI consumption in each process. The average cell efficiency of each deposition varies significantly, with depositions 1 and 9 having the highest efficiencies of around 10% each and 4,5,6 and 8 below 2% efficiency. The amount of MAI consumed in each process does not correlate with the measured efficiencies, we see however that the two highest efficiency processes were after refilling the MAI crucibles with fresh MAI.

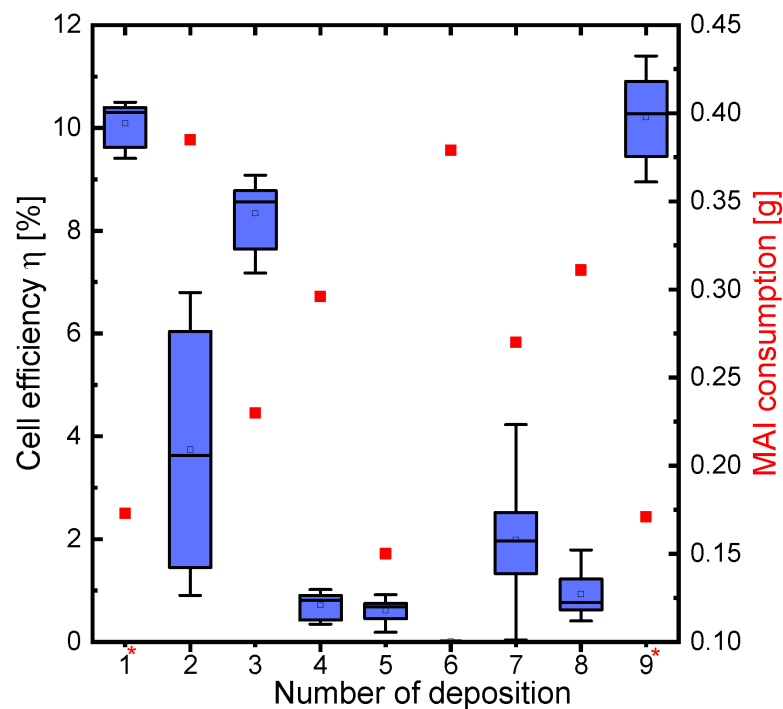


Figure 4.3: Cell efficiencies of nine consecutive rate controlled perovskite depositions. MAI was refilled before deposition 1 and 9.

Many of the low (or non) performing solar cells of these experiments have a slightly dull surface after air exposure. The light-IV curves of these solar cells often do not have any measured light generation and are therefore not even evaluable in terms of solar cell parameters mentioned above (see Figure 4.4 for an ex-

ample) and otherwise are poor performing (efficiency below 2%). As I explained

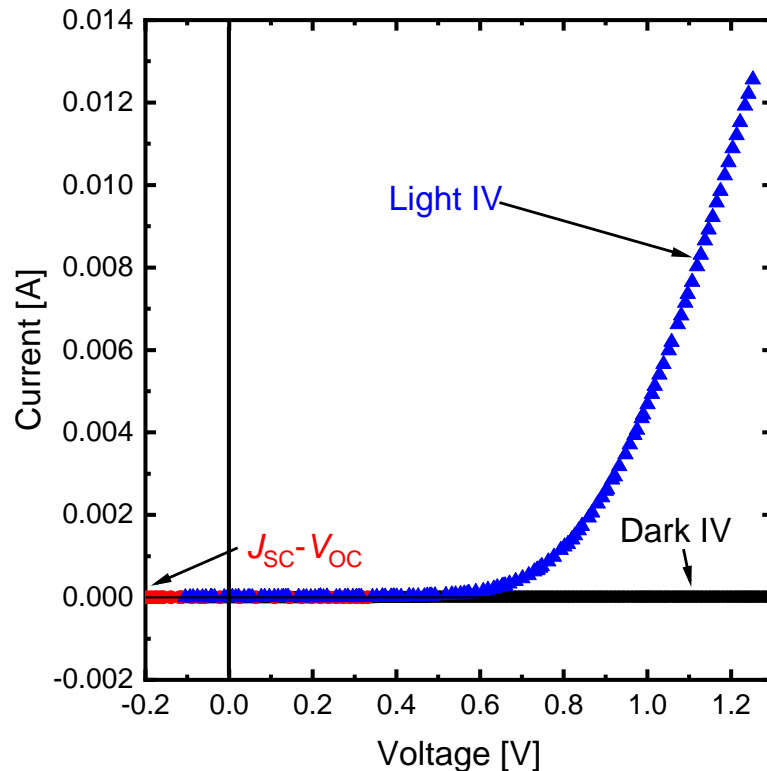


Figure 4.4: Light-IV, dark-IV and  $J_{sc}$ - $V_{OC}$  measurement of a PSC with dull surface that has no current generation under illumination.

in chapter 3 the dull surface likely stems from the diffusion of water into MAI rich perovskites [70, 114]. The detrimental effect of this water diffusion on cell performance could either be purely caused by the increased roughness after the perovskite and C60/BCP deposition, leading to a mechanical destruction of the ETL. The formation of water related species (like water soluted MAI or perovskite hydrates, especially at the interface of perovskite/ETL) could be another explanation for the poor performance. Both mechanisms are schematically shown in Figure 4.5.

The detrimental effects on cell performance are however still visible for slightly dull samples that do not exhibit much roughness when looking at them in the SEM (see Figure 4.6). This result implies, that water induced species like hydrates are detrimental even when the ETL is still intact. One possibility to remove excess MAI would be a rinsing step with isopropanol before ETL deposition that is performed for wet-chemical processed perovskites [81]. In practice, this would complicate the whole processing and would likely require several additional processing steps (exposure to moisture, rinsing, annealing etc.) and additional working

#### 4.1. CELL REPRODUCIBILITY AND INFLUENCE OF PROCESS CONDITIONS

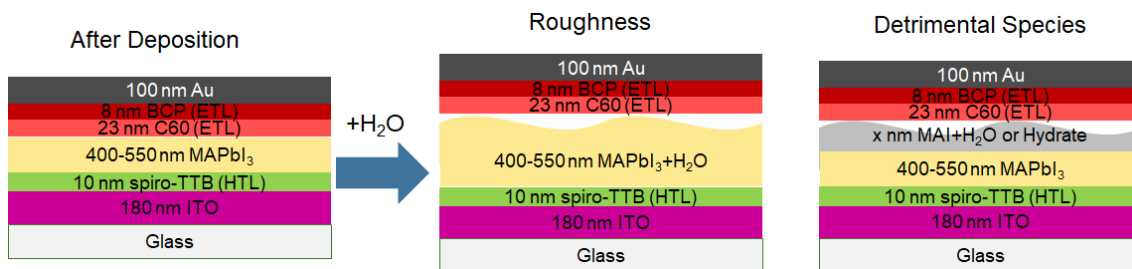


Figure 4.5: Water incorporation in MAI rich perovskites could cause only roughness (middle) or roughness and the additional formation of perovskite hydrates or soluted MAI (right).

space in a glovebox to perform these processing steps. This whole procedure is not reported for any evaporated perovskites. We therefore take the more practical solution to this problem and aim to be always on PbI<sub>2</sub> rich processing conditions where this problems does not seem to occur.

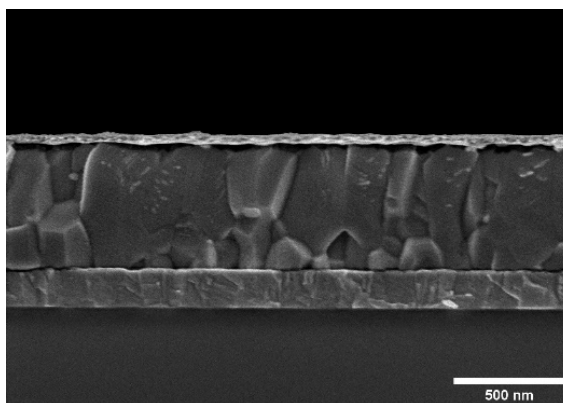


Figure 4.6: SEM image of a non-working PSC with a slightly dull surface, exhibiting no visible roughness or ETL destruction in the SEM.

#### 4.1.2 Fresh MAI and temperature controlled processes

For the temperature controlled processes we only use fresh MAI (typically 0.5 g) in every process and aim for a deposition process window on the PbI<sub>2</sub> rich side, as explained above. Figure 4.7 shows the average cell efficiencies for 22 perovskite depositions with MAI Batch 1 and 2.

Eight of these 22 processes show an average cell efficiency of above 10%, with the best cells achieving over 13% efficiency and only one of the processes below 2% efficiency. This is a significant improvement to the solar cell efficiencies with the refilled MAI (Figure 4.3). Not only are the average and top efficiencies increased, but we also have significantly less (1 out of 22 compared to 4 out of 9)

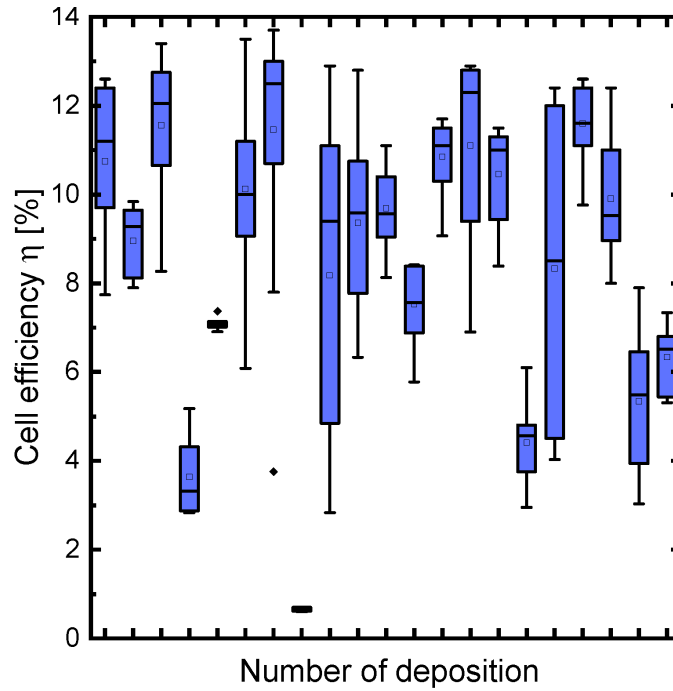


Figure 4.7: Cell efficiency  $\eta$  of 22 perovskite depositions with MAI Batch 1 and 2.

processes where the solar cells are barely working (below 2% efficiency). None of the samples shows any dull surface after air exposure, which means none of the perovskites have a significant amount of excess MAI. If we take a deeper look into the solar cell parameters  $V_{OC}$ ,  $J_{SC}$  and  $FF$  (see Figure 4.8), we can see that most solar cells have a  $V_{OC}$  in the range of 1000 to 1100 mV, the  $FF$  ranges from 30 to 65% and  $J_{SC}$  from 10 to 20 mA/cm<sup>2</sup> with a few outliers each. Figure 4.8d shows the champion device from MAI Batch 1+2 with a cell efficiency of 15%. If we compare these results to the highest performing co-evaporated MAPbI<sub>3</sub> cells in literature [84, 39], these also report only low differences in  $V_{OC}$  but a higher spread in both  $J_{SC}$  and  $FF$  for non-stoichiometric perovskite layers. Both groups do not measure this much variance in  $J_{SC}$  and  $FF$  for stoichiometric perovskites, however they both only measure the deposition rate and are not reporting anything about the reproducibility of their process, the stoichiometry or the thickness range of the resulting perovskite layers.

The mechanisms behind the large spread in  $J_{SC}$  and  $FF$  are currently not understood [39].

Refined ways for a loss analysis at each interface/material that are established for silicon solar cells [124] are not established for perovskite solar cells and the instability of the processing and solar cell stability are a main hindrance to even develop such systems.

#### 4.1. CELL REPRODUCIBILITY AND INFLUENCE OF PROCESS CONDITIONS

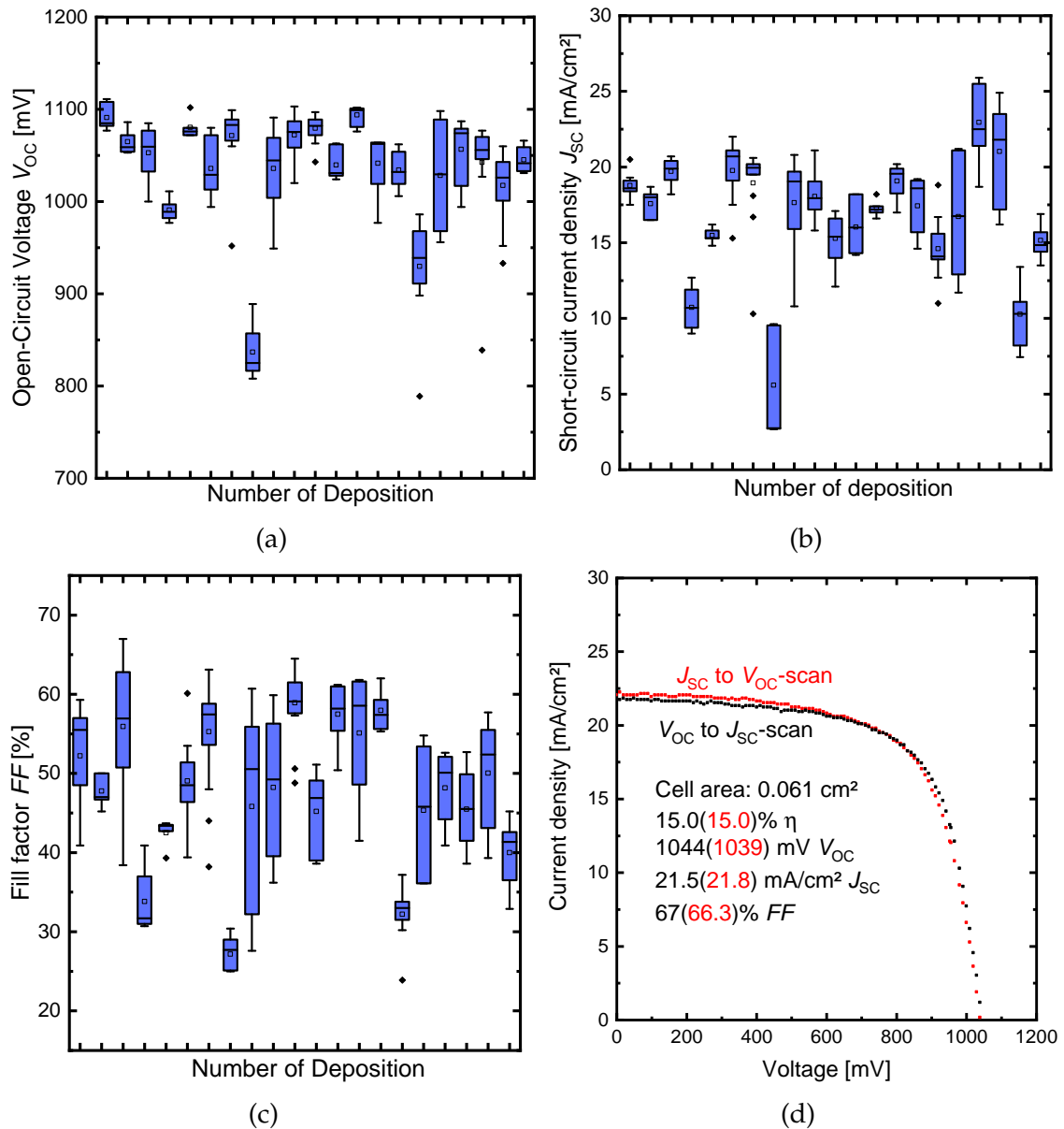


Figure 4.8: Cell parameters of the solar cells from MAI Batch 1+2. (a)  $V_{OC}$ , (b)  $J_{SC}$  (c)  $FF$  (d) Light-IV of the highest performing cell.

#### 4.1.3 Chamber cleaning

As I explained in chapter 2.2, we evaporate the contact layers in the same chamber as the perovskite, contrarily to the groups that process the highest efficiency PSCs. MAI has a diffuse evaporation that coats the evaporation chamber and permanently evaporates once deposited, which causes all  $PbI_2$  films to contain at least some amount of MAI after the first MAI deposition. This can additionally cause a cross-contamination during evaporation of the contact layers. To investigate, whether or not this cross-contamination of the processing chamber plays

a significant role for the measured cell parameters, we process perovskite solar cells directly after we mechanically cleaned the chamber. We perform these experiments with MAI Batch 3+4.

Figure 4.9 shows the cell parameters of the respective perovskite solar cells. The number of deposition in this case is based on how many perovskite deposition processes we performed after the chamber cleaning. We achieve the highest efficiencies with up to 16% in the processes shortly after cleaning the evaporation chamber. Although we again see a large variation in the short-circuit current density (about 5 to 20 mA/cm<sup>2</sup>) and fill factor (about 45% to 75%), both have a decreasing trend with increasing number of depositions.

The open-circuit voltage again remains relatively stable around 1050 mV, with no significant trend regarding the number of depositions.

If we compare the current density of these solar cells (Figure 4.9b) with the ones from MAI Batch 1+2 (Figure 4.8b), where the chamber was not cleaned prior to the experiments the current density of the solar cells made with MAI Batch 1+2 is higher and does not vary that significantly. This is likely due to a higher amount of MAI in the perovskites from MAI Batch 1+2 (see chapter 3.1.2, Figure 3.3), leading to a more stoichiometric perovskite with higher absorption in average. In chapter 5 I will explain how current losses could be caused by parasitic absorption at the HTL/perovskite interface, which could be more severe for more PbI<sub>2</sub> rich perovskites as well.

If we take a look at the fill factors (Figure 4.9c) we can see that for the first depositions with MAI Batch 3+4 these often exceed 70% and decrease to around 50 to 60% with increasing deposition number. For the perovskite solar cells deposited with MAI Batch 1+2 we only see fill factors up to 60%. This could be an indication that cleaning the chamber actually increases the fill factor, due to less MAI contaminations in the contact layers and a more efficient charge carrier extraction. For proper investigations of this it is however necessary to completely separate the deposition of the contact layers from the deposition of the perovskite, what currently (Q1/2022) has not been accomplished yet at ISFH.



#### 4.1. CELL REPRODUCIBILITY AND INFLUENCE OF PROCESS CONDITIONS

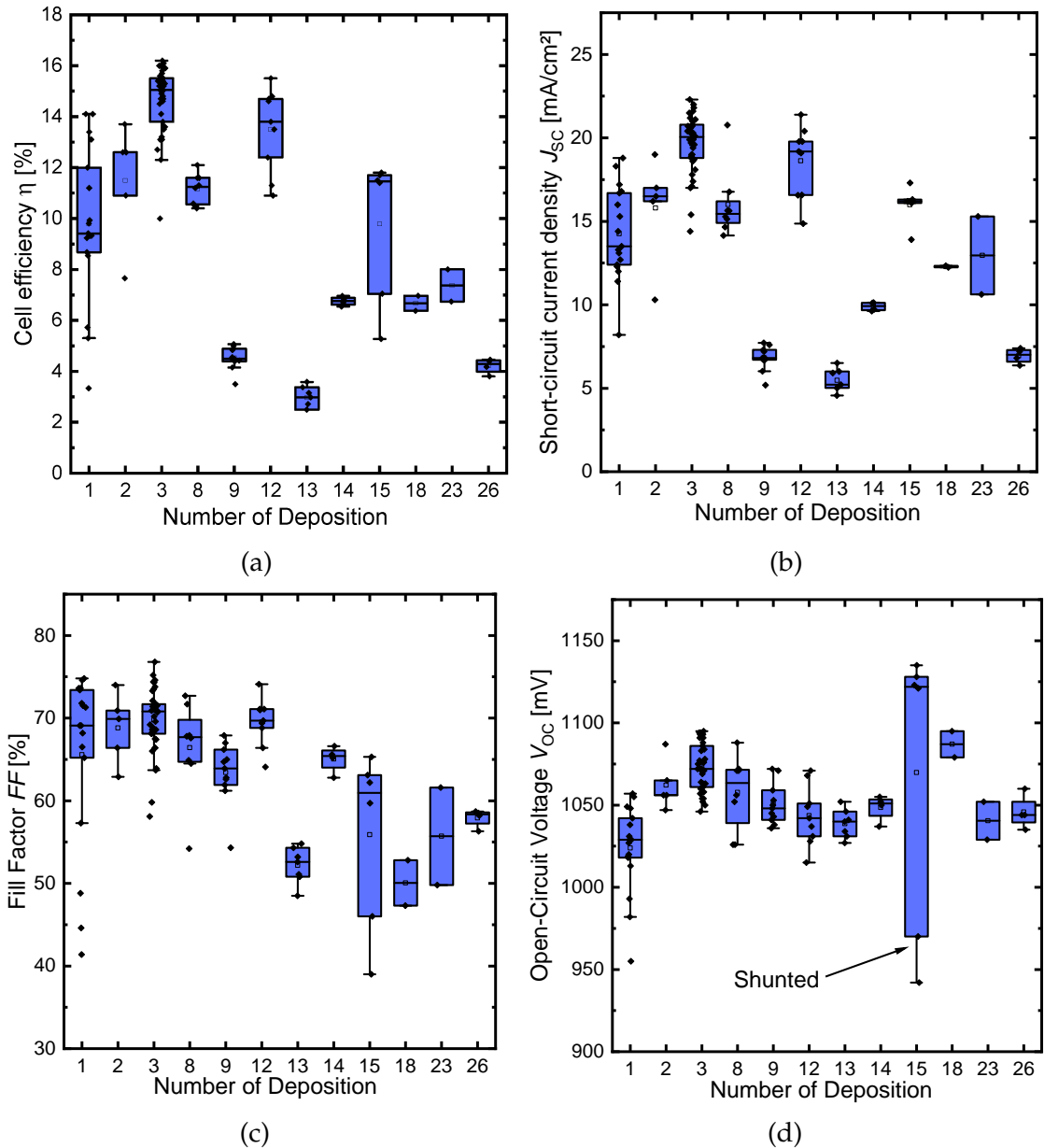


Figure 4.9: Cell parameters of the solar cells from MAI Batch 3+4. (a)  $\eta$ , (b)  $J_{sc}$  (c)  $FF$  (d)  $V_{oc}$ .

#### 4.1.4 Dark-IV and Shunts

So far I have only presented the light-IV results of solar cells that are (mostly) not shunted. In Figure 4.9d we see a large discrepancy in the open-circuit voltage of over 150 mV for solar cells from deposition 15. If we take a look at the dark-IV measurement of two of these solar cells, shown in Figure 4.10, we can see that one of the cells has a noticeable shunt with a shunt resistance of about  $2000 \text{ Ohmcm}^2$ , whereas the other solar cell shows no shunt.

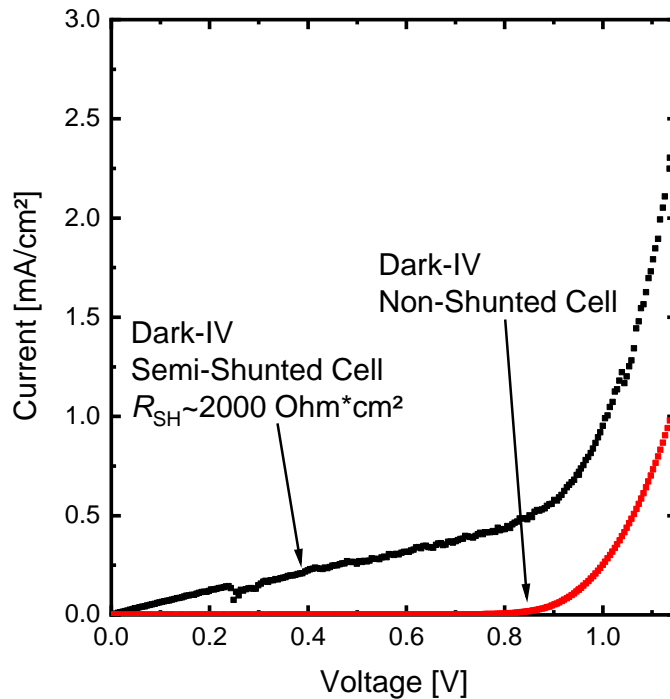


Figure 4.10: Dark-IV measurements of two PSCs on the same substrate, revealing a leakage current for one of the solar cells.

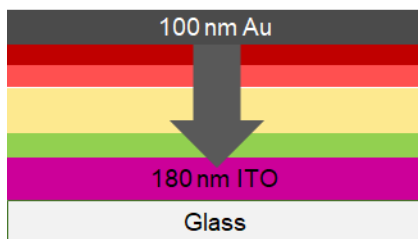


Figure 4.11: Shunts in the PSCs are caused by a damage in the CTLs and perovskite, causing a direct connection between the electrode and ITO (grey arrow).

Both of these solar cells are on the same substrate. The reason of this difference in shunt resistance are therefore not differences in perovskite or CTL properties etc. The main reason for shunts in perovskite solar cells is that almost any physical contact of the soft perovskite and contact layers with for example a tweezer leads to a local destruction of the layers. When the solar cell is then contacted, this causes a direct connection between ITO (p-contact) and the metal on the n-contact, short-circuiting the cell, as is exemplarily depicted in Figure 4.11. Although there are some reports about this behaviour for wet-chemically processed perovskites with local holes after perovskite deposition [125], even reports that focus on the amount of shunts do not consider mechanical stability or give any numbers about how damages during the processing influence the amount of shunts [126]. Typically, the amount of shunted cells is not reported and just not considered in any evaluation of process optimisation.

For the PSCs we process at ISFH approximately 20 to 70% of the solar cells are

#### 4.1. CELL REPRODUCIBILITY AND INFLUENCE OF PROCESS CONDITIONS

completely shunted with a shunt resistance typically in the range of 10 to 20  $\text{Ohmcm}^2$ , showing only resistance like behaviour with no difference in light-IV to dark-IV. This number varies a lot, because it depends on the person itself processing and measuring the solar cells for example.

This is one of the main reasons, next to the series resistance in the TCO (see section 2.2.5), why we and other groups mostly process very small cells with several cells on each substrate. An industrialisation of the cell design used in this work is unrealistic due to the issues with cell size and shunts. Its main application is the comparison of different materials and processes for cell development on small proof-of-concept devices.

##### 4.1.5 Influence of $\text{PbI}_2$ excess on processing stability

For solar cells from the same perovskite and contact layer deposition process, the cell parameters ( $\eta$ ,  $J_{SC}$ ,  $FF$ ,  $V_{OC}$ ) quite often differ significantly, even for cells that are not shunted. As I discussed already the processing conditions heavily influence the cell performance in perovskites. We deposit the electrode (Au) in a different processing tool than the perovskite and CTL which is located outside of a glovebox. This means that the solar cells come in contact with ambient atmosphere before and after the deposition of the electrode material. During the gold evaporation the temperature on the samples is varying by a maximum between 100 to 130°C for different evaporations (see the Bachelor thesis of Niko Mielich for more details about the temperature behaviour [97]). Perovskite solar cells with MAI Batch 1+2 from different gold depositions but the same deposition process for the perovskite and contact layers are different in terms of efficiency, as displayed in Figure 4.12. This adds another layer of uncertainty to any analysis of our perovskite solar cells, because not only do the cell efficiencies alter between different perovskite and CTL evaporations but between different electrode evaporations as well.

As I displayed in Figure 3.3 the MAI consumption for a perovskite deposition with MAI Batch 1+2 is about 200 mg, whereas for MAI Batch 3+4 it lies in the range of 100 mg. If we analyse the reflection measurements of perovskite solar cells made from the different batches (see section 5.3.1 and 5.3.4 for the method and uncertainty of this method), we can estimate an average  $\text{PbI}_2$  content in the perovskite layer of about 20% for MAI Batch 1+2 and 40% for MAI Batch 3+4. The amount of MAI consumption varies however for every deposition.

For MAI Batch 3+4 the first deposition of the processes in Figure 4.9 has a MAI

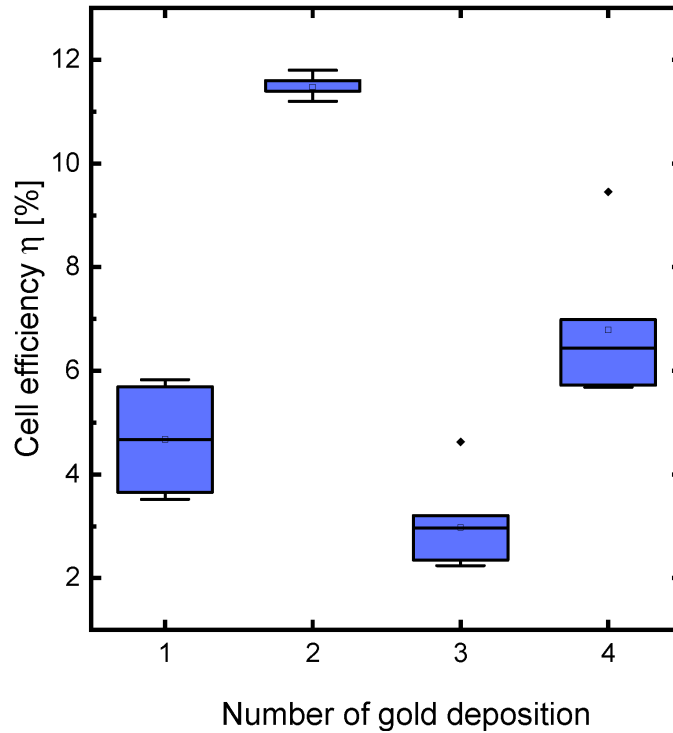


Figure 4.12: Average cell efficiencies of PSCs from one perovskite+CTL but four different gold depositions.

consumption of 205 mg, similar to the average of MAI Batch 1+2. We compare the solar cells of this perovskite deposition to one where the MAI consumption is only 132 mg. The solar cells with the higher MAI consumption have an estimated  $\text{PbI}_2$  amount of around 23% (low  $\text{PbI}_2$  excess), compared to 45% (high  $\text{PbI}_2$  excess) for the solar cells with the lower MAI consumption. We process solar cells from both groups (low and high  $\text{PbI}_2$  excess) in a total of four metallisations, with solar cells from each group being in a total of three metallisations, with two metallisations containing cells from both groups. If we take a look at the different cell parameters of both groups ( $\eta$ ,  $J_{SC}$ ,  $FF$ ,  $V_{OC}$ , see Figure 4.13 and Figure 4.14), we can see that the cells with high  $\text{PbI}_2$  excess are more stable in every cell parameter compared to the cells with low  $\text{PbI}_2$  excess. As before, the relative differences in  $J_{SC}$  and  $FF$  are much higher than for  $V_{OC}$  in both groups, confirming the results previously displayed. One mechanism to explain this behaviour could be that even though both perovskite layers have a  $\text{PbI}_2$  excess, free MAI is still incorporated to some extent. By increasing  $\text{PbI}_2$  excess the amount of free MAI decreases, leading to less reactions with for example moisture in the perovskite layers during exposure to air which causes the cells to be more stable.

#### 4.1. CELL REPRODUCIBILITY AND INFLUENCE OF PROCESS CONDITIONS

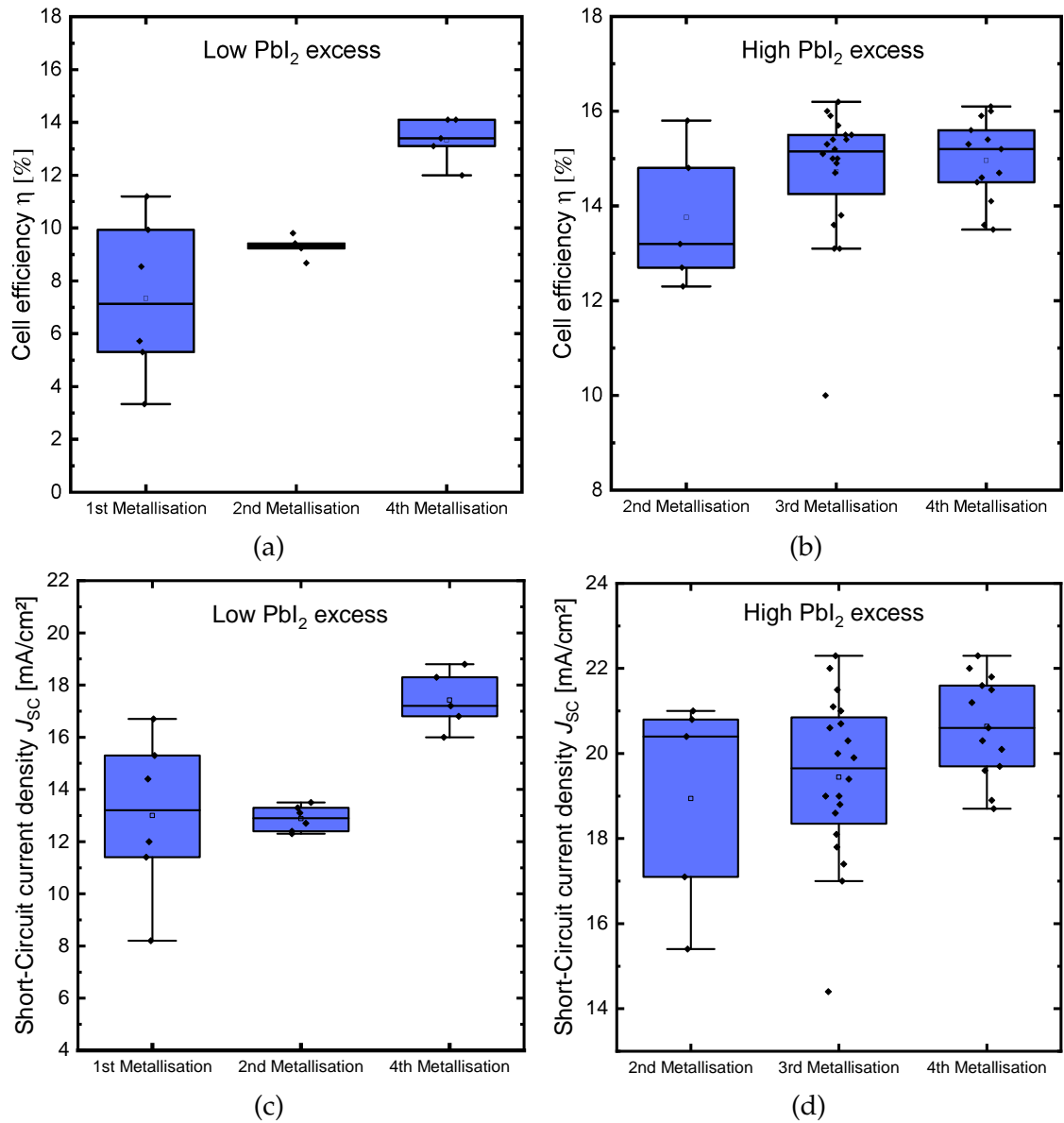


Figure 4.13:  $\eta$  and  $J_{sc}$  for PSCs from different metal evaporations for low and high  $\text{PbI}_2$  amounts.

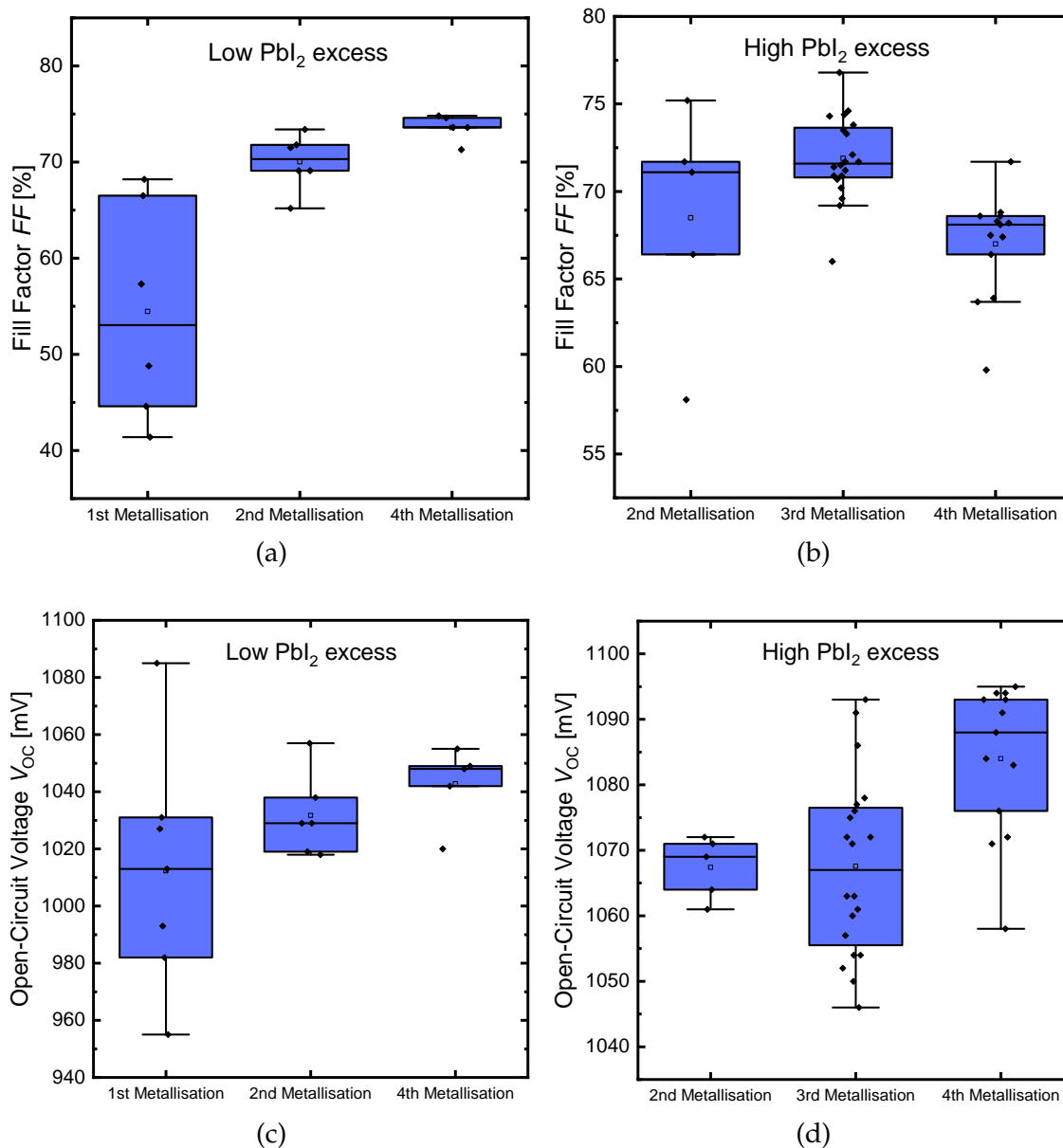


Figure 4.14:  $FF$  and  $V_{OC}$  for PSCs from different metal evaporations for low and high  $\text{PbI}_2$  amounts.

### 4.1.6 Processing and measurements without ambient atmosphere and efficiency potential

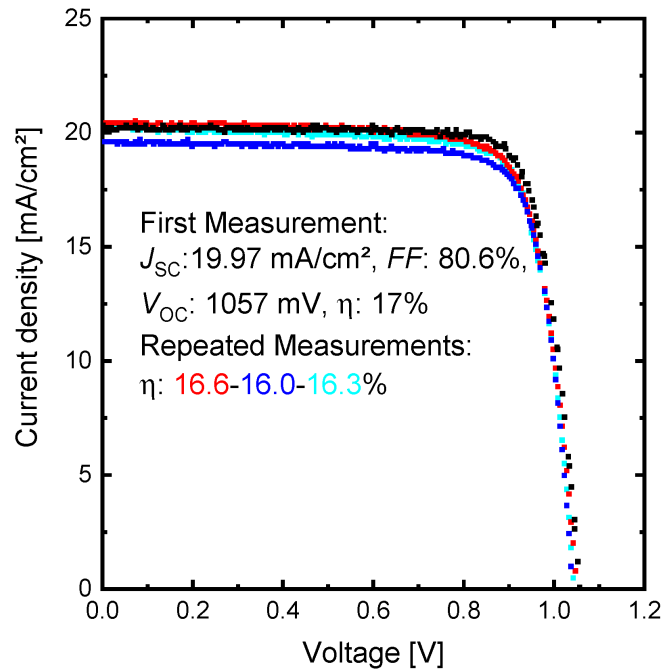


Figure 4.15: Light-IV measurement of one of the highest performing PSCs processed at ISFH to date (Q1/2022).

Ideally, the perovskite solar cells are not exposed to ambient atmosphere before deposition of the metal electrode. Just recently, we got a new deposition tool inside a glovebox for the metal evaporation (Lesker NANO36) where we use copper (Cu) as electrode material, which is more scratch-resistant and much cheaper than gold. Additionally, with the encapsulation method presented in section 2.2.6 we are able to seal our solar cells after the metal deposition to perform the cell measurements outside a glovebox atmosphere without diffusion of water into the perovskite layer. With these improvements the first results of perovskite solar cells with a near stoichiometric perovskite (still slightly  $\text{PbI}_2$  rich) are displayed in Figure 4.15. These results are quite promising, showing an efficiency of 17% in the first measurement, with the most noticeable improvement being the high fill factor (80.6%) of the solar cell.

If we consider that we already demonstrated a  $V_{OC}$  of around 1100 mV on several perovskite solar cells, and can achieve a  $J_{SC}$  of up to 21.78  $\text{mA}/\text{cm}^2$  with this cell design (see section 5.3.2), cell efficiencies of about 19.3% are potentially

possible, which is similar to the recently reported best solar cells with this exact layer sequence [91]. Further improvements can be accomplished by more effective transport layers for the HTL, leading to a higher  $V_{OC}$  and  $FF$  [39, 84] or by optical improvements presented in chapter 5.3.2.

The cells processed with the NANO36 and afterwards encapsulated inside a glove-box however still suffer from high amounts of shunts and an optimisation of the processing is needed.

As we can see in Figure 4.15, repeating the solar cell measurement (without any new contacting between each measurement) leads to variations in the cell efficiency (in this example, perovskite-typical mostly in  $J_{SC}$  and  $FF$ ). So far, most cell results displayed here were from the first measurement of the solar cell. If the power output of the cell is not constant however, this raises the question how to reliably measure the power output of our solar cells.

## 4.2 PSC solar cell stability and measurement

### 4.2.1 Ionic charge transport, charge accumulation and hysteresis

Ideally, a solar cell has a stable power output (ideally over 25+ years) and measuring the light-IV curve repeatedly should yield the same result every time. As we can see in the example above (Figure 4.15), this is not the case for our cells.

One of the major reasons for instability of perovskite cell performance (next to sensitivity of perovskites to moisture etc.) is the ionic transport of charge carriers in perovskites. Contrary to electrons or holes, that move through the perovskite to the contacts in a timeframe below one microsecond, ions diffuse through the perovskite layer with a much lower speed of several milliseconds and above [127]. Especially iodide ions, which is the by far most mobile ion species in  $\text{MAPbI}_3$ , affect the solar cell performance [128]. Iodide ions not only move relatively slowly through the perovskite when an external voltage is applied to the solar cell, but iodide ions or vacancies accumulate at the interfaces to the hole or electron contacts, causing an electrical field that is detrimental for the solar cell [46].

The slow ionic movement additionally causes an effect described in the perovskite community as hysteresis of the IV curve, meaning that measuring the IV curve from  $J_{SC}$  to  $V_{OC}$  (forward scan) leads to a different result than measuring from  $V_{OC}$  to  $J_{SC}$  (reverse scan) [129]. A good summary of the mechanisms causing



#### 4.2. PSC SOLAR CELL STABILITY AND MEASUREMENT

hysteresis in perovskite solar cells was published by Wolfgang Tress in 2018 [66]. To reduce hysteresis one option is to measure the IV curve using a slow scanning

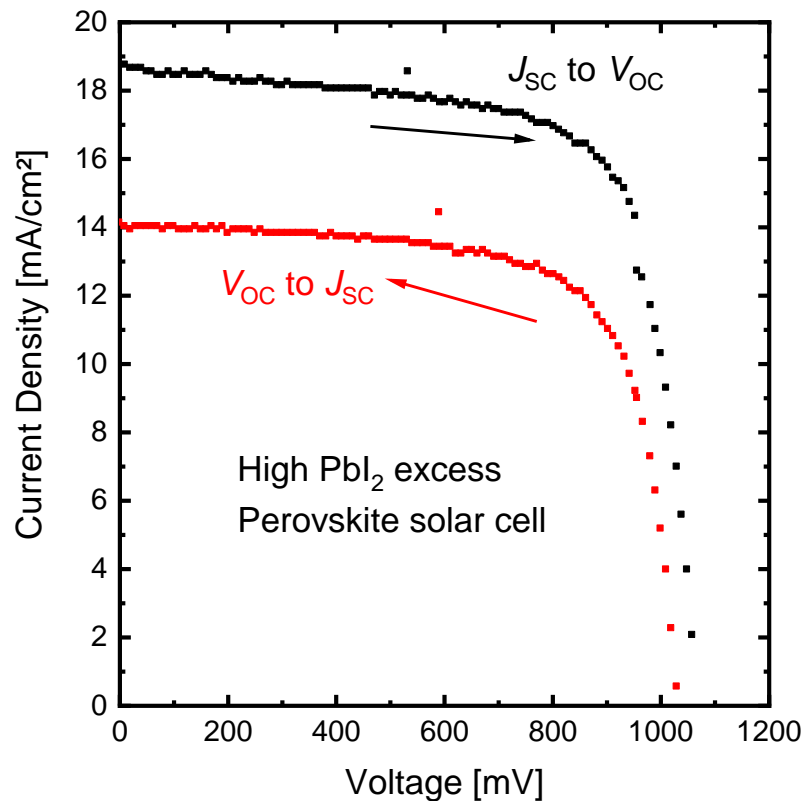


Figure 4.16: Light-IV measurement of a PSC with significant inverted hysteresis (from MAI Batch 3+4).

rate. There are several publications claiming a scan rate of 25 mV/s and several forms of pre-conditioning of the solar cell (applying a certain voltage under illumination for some time before the measurement) to be ideal [130, 131]. For the highest efficient co-evaporated MAPbI<sub>3</sub> perovskite solar cells with no hysteresis a higher scan rate of 300 to 600 mV/s has already been reported [90, 39, 83]. In measurements of tandem solar cells with wet-chemical perovskites with efficiencies above 29% a fast scan rate of 250 mV/s was reported as well [11]. The proper solution for hysteresis or ion movement in perovskite solar cells is therefore to improve the perovskite layer and charge carrier extraction so that the effect of ion movement on cell performance and reliability is minimized by reducing the density of mobile ions [46, 132]. At ISFH, we measure both the light- as well as the dark-IV curve with a scan speed of 140 mV/s or 25 mV/s in steps of 10 mV or 5 mV.

Not all perovskite solar cells at ISFH show significant hysteresis. Figure 4.15

shows an almost hysteresis free PSC for example. Hysteresis measurements of several PSCs processed at ISFH can be found in the master thesis of Moritz Engl [65]. Especially for the solar cells with a high amount of  $\text{PbI}_2$  excess most cells show a significant hysteresis as is shown in Figure 4.16.

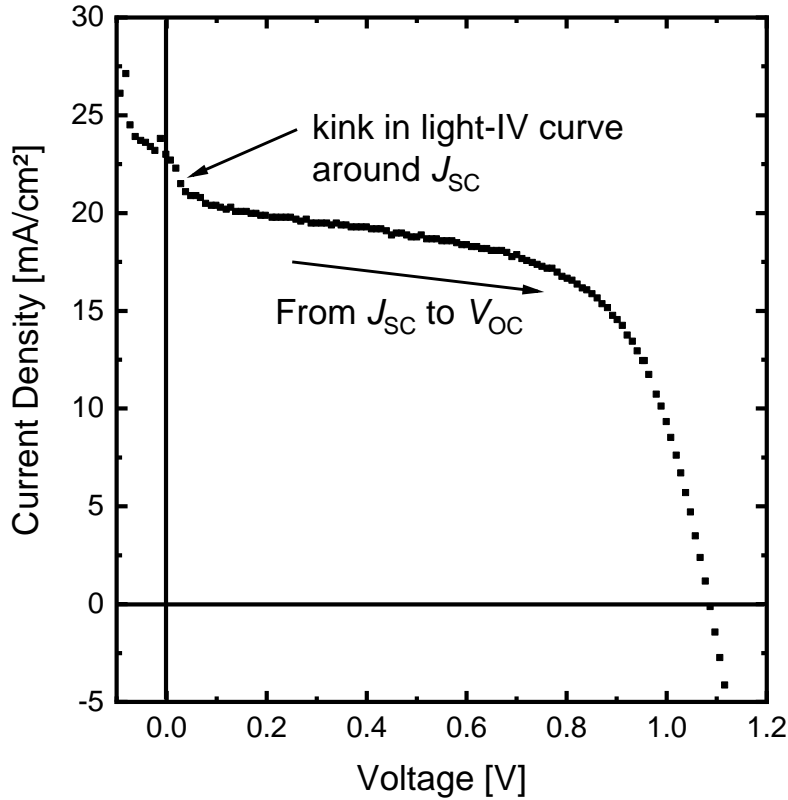


Figure 4.17: Light-IV measurement of a PSC from  $J_{SC}$  to  $V_{OC}$  showing a kink around  $J_{SC}$ .

This exact form of hysteresis is actually called inverted hysteresis [133] and rather uncommon. We cannot directly measure the ion movement or density that causes this type of hysteresis in our cells.

Additionally, the light-IV curve from  $J_{SC}$  to  $V_{OC}$  often shows a sort of kink around  $J_{SC}$  (Figure 4.17), leading to unrealistically high (see chapter 5.3.3)  $J_{SC}$  values [134]. This is why we currently use a scan direction from  $V_{OC}$  to  $J_{SC}$  as standard, where this behaviour does not occur. We have already discussed that a high amount of  $\text{PbI}_2$  excess is detrimental for several reasons (low absorption, reproducibility etc.). Therefore it is not viable to further optimise the measuring conditions for  $\text{MAPbI}_3$  with  $\text{PbI}_2$  excess but to optimise the perovskite deposition process for a perovskite layer with a lesser amount of ionic movement. The first results of the encapsulated PSC with stoichiometric (or only slightly  $\text{PbI}_2$  rich)  $\text{MAPbI}_3$  displayed in Figure 4.15 shows almost no hysteresis. This result is

## 4.2. PSC SOLAR CELL STABILITY AND MEASUREMENT

promising, showing that with improvements in processing we can likely achieve hysteresis free perovskite solar cells at ISFH as well.

### 4.2.2 Cell stability, aging and s-shape

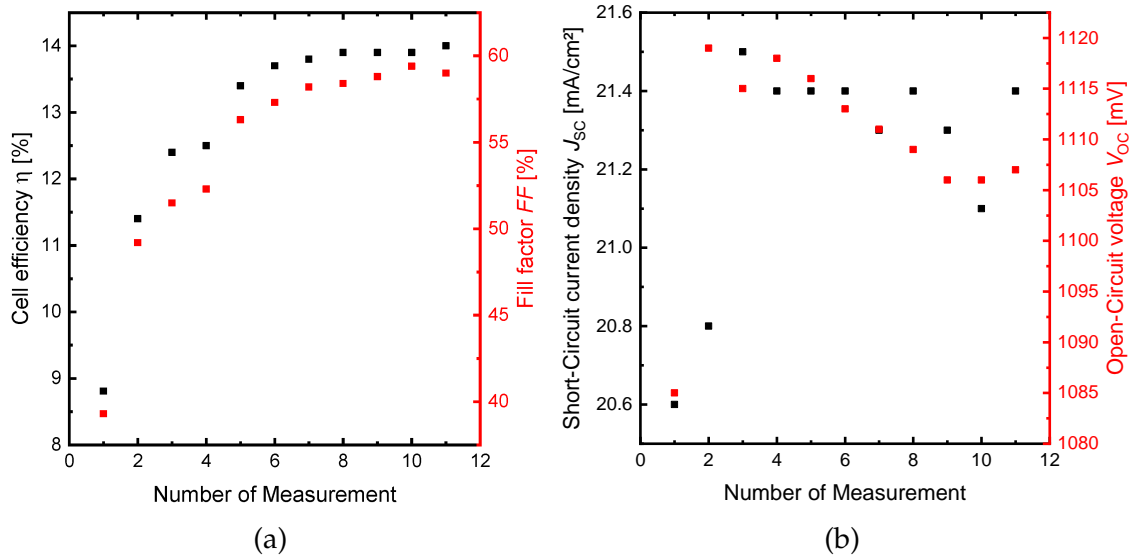


Figure 4.18: Repeated light-IV measurements showing the (a)  $\eta$  and  $FF$  and (b)  $J_{sc}$  and  $V_{oc}$  of a PSC from MAI Batch 1+2

Another factor to consider is how stable our solar cells are when exposed to ambient environment and light exposure during the solar cell measurement. A simple way to measure this is to just repeat the light-IV measurement on the same solar cell and see how the different cell properties change, without new contacting. This type of measurement is displayed in Figure 4.18 for a perovskite solar cell made with MAI Batch 1+2. We can see that the fill factor strongly increases in the first measurements from 40 to almost 60%, leading to an increase in cell efficiency.  $J_{sc}$  and  $V_{oc}$  only alter on a way lesser magnitude and after a sharp increase from the first to second or third measurement they start to decrease again. Most solar cells do not show this much variance in the fill factor though and better performing solar cells are typically more stable under illumination, as is displayed for our champion cell, where no significant change in fill factor occurs and for four light-IV measurements the absolute efficiency varies by only one percent.

Most of our solar cells are measured shortly after the metallisation. In some cases, a certain timeframe of several days to sometimes weeks or months between the deposition of the perovskite and contact layers and the metal deposition can occur, for example when we use older samples as a reference. We store the cell

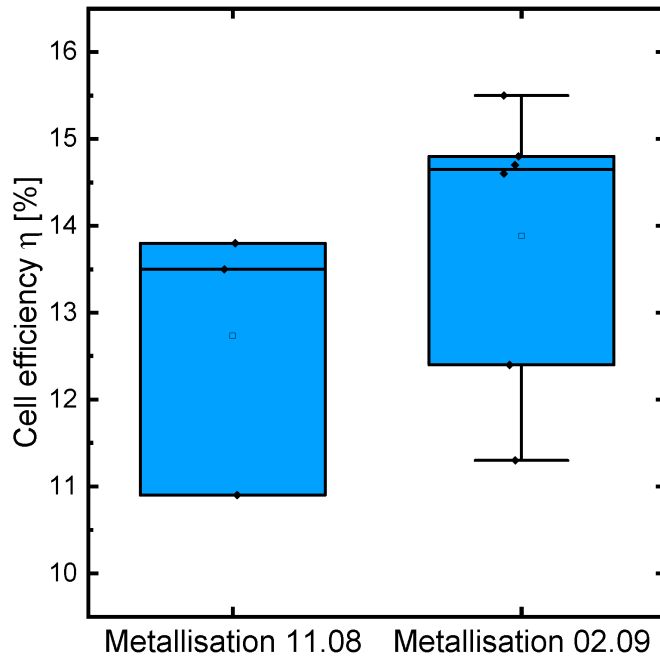


Figure 4.19: Average cell efficiency of several PSC from MAI Batch 3+4 from the same deposition process for the perovskite and CTL, but with different electrode depositions.

precursors after the perovskite deposition in a nitrogen-filled glovebox to avoid degradation due to moisture or oxygen. Figure 4.19 shows the cell efficiencies of the metallisation of two samples each from the same perovskite and HTL deposition on 28.07.2021 (deposition 12 from MAI Batch 3+4). The metallisations were performed at 11.08.2021 and 02.09.2021, thus about 15 days and over a month after deposition of the perovskite. We do not see any decrease in cell performance for the cells that were stored longer prior to the metallisation. The solar cells from this deposition are among the highest performing solar cells of MAI Batch 3+4. Storing the solar cell precursors in a glovebox before the metallisation likely does not lead to any performance losses for at least a month, at least for the type of perovskite solar cell presented in this work.

If we put the solar cells in a glovebox after metallisation and store them they start to degrade in most cases as shown in Figure 4.20. Not only does the  $J_{SC}$  and  $FF$  decrease, but the shape of the IV curve can alter to something called an s-shape. If we measure our solar cells directly after the metallisation, almost no cell exhibits any form of s-shape, however after a couple months inside a glovebox, we can see this behaviour relatively often. The mechanism causing the s-shape is explained by degradation of the interfaces in the solar cell, causing barriers for charge carriers [135]. The reason for this interface barriers to form is, similar to

## 4.2. PSC SOLAR CELL STABILITY AND MEASUREMENT

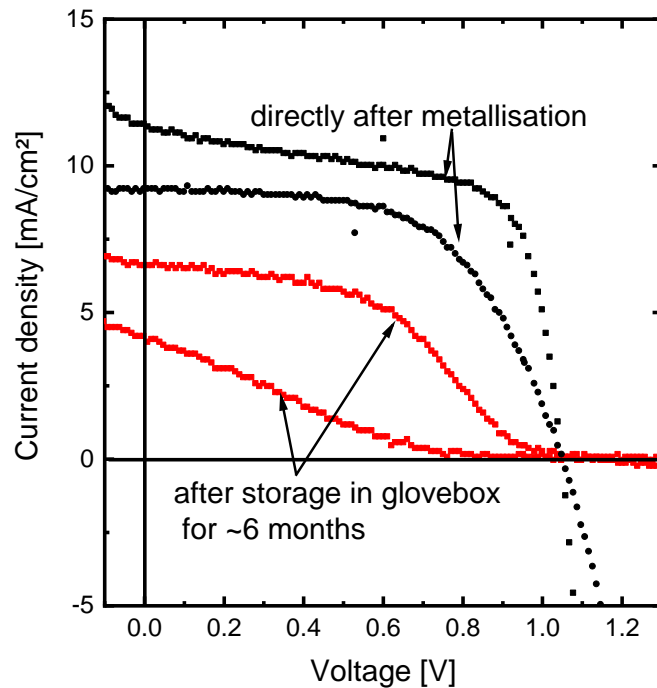


Figure 4.20: Light-IV measurement from two PSCs directly after deposition (black) and after about six months storing in a nitrogen-filled glovebox (red).

the hysteresis, accumulation of ions at the interfaces [136].

### 4.2.3 Ionic movement and how to measure perovskite solar cells

As I have explained above, both hysteresis and s-shape like behaviour occur for our solar cells and are detrimental to cell efficiency and stability. Both effects are likely caused by ions that either slowly move through the perovskite during the light-IV (hysteresis) or accumulate and degrade the interfaces in a perovskite solar cell (s-shape). There are different methods discussed that mitigate ionic movement, such as specified doping of the perovskite, interface engineering or changing the perovskite composition [62, 63]. Still there is no sufficient solution found for this problem, which is one of the main issues why perovskite solar cells are not stable enough for commercial applications until now [137].

There are several publications discussing high amounts of excess  $\text{PbI}_2$  to be one of the main factors that causes ionic movement and degradation in  $\text{MAPbI}_3$  [77, 138]. Additionally, smaller grain sizes (that are typical for  $\text{PbI}_2$  rich perovskites as discussed in chapter 3.2.2) also correlate with increased hysteresis/ionic movement [139]. The metal interface is described as especially prone to degradation due

to irreversible ion accumulation and formation of insulating metal-iodide compounds [136]. This is likely why we see a degradation of our solar cells after metallisation but not if a cell precursor without metallisation is stored inside a glovebox.

Recent reports show excellent stability (even at elevated temperatures in presence of humidity) and no hysteresis even for  $\text{PbI}_2$  rich evaporated  $\text{MAPbI}_3$  solar cells [93, 140]. Other groups also report high efficient evaporated  $\text{MAPbI}_3$  solar cells without hysteresis with a similar layer stack to our cells [91, 84]. To achieve these kind of results here, the best way is to remove the influence of moisture by processing inside a glovebox and encapsulating our solar cells for measurements outside glovebox atmosphere. Since we know that the other layers (spiro-TTB, C60, BCP, copper or gold), which are used by other groups as well, are not the cause of ionic movement we can focus solely on optimising the  $\text{MAPbI}_3$  deposition to minimize ionic movement by observing hysteresis and long term cell stability.

The most suitable method to quantify hysteresis effects and the power conversion efficiencies of perovskite solar cells in general is to measure the steady-state efficiency or a maximum power-point (*MPP*) tracking of the perovskite solar cell [131, 141]. The steady-state efficiency (*SSE*) means that after performing a light-IV scan the solar cell is set to the voltage of the maximum power point ( $V_{mpp}$ ) of the light-IV. Then the current is measured for a specific timeframe, typically a couple of minutes. The maximum power-point tracking is quite similar, however the cell is operated at the maximum power point in this case, so the voltage has to be adjusted during tracking. This is making it a bit more complex in terms of the measurement, but more accurate as well for solar cells with a non-stable  $V_{mpp}$ . An external voltage causes ionic movement (since ions are charged). From the initial response of the solar cell to the applied voltage and light (timeframe until a stable power output is reached or the extent of instability at the start of the measurement) the amount and speed of ionic movement in the cell can be at least qualitatively assessed. From the long-term stability under *MPP*-conditions detrimental effects to cell performance (ion accumulation or the formation of metal iodide) can be investigated. *SSE* measurements or *MPP*-tracking are therefore crucial in the development of perovskite solar cells. Unfortunately, no stable algorithms for *MPP*-tracking or even *SSE* measurements are currently (Q1/2022) established at ISFH.

#### 4.2.4 QFLS, $V_{OC}$ and photoluminescence of perovskite solar cells

As discussed in chapter 2.1.3, photoluminescence measurements can yield insight into recombination losses in perovskite solar cells. Typically, the higher the photoluminescence, the lesser amount of nonradiative recombination in a semiconductor material, which results in higher  $V_{OC}$ s of the solar cells. The highest  $V_{OC}$  a solar cell can achieve is related to its quasi fermi level splitting (QFLS), which is effectively the band gap of the absorbing material (in our case the perovskite) minus losses to recombination. The QFLS is closely related to the radiative recombination (which equals the absolute photoluminescence) in a material [142, 143]. Although we cannot calculate the absolute value of the QFLS because we cannot measure the absolute value of the photoluminescence at ISFH, we can calculate the relative change in photoluminescence of different samples. If the  $V_{OC}$  of a solar cell is limited by recombination, a relative change in the photoluminescence intensity ( $\Delta PL = \text{Intensity PL}_1 / \text{Intensity PL}_2$ ) due to recombination correlates mathematically to a change in  $V_{OC}$  ( $\Delta V_{OC} = V_{OC,1} - V_{OC,2}$ ) as [144]:

$$q \cdot \Delta V_{OC} = kT \cdot \ln(\Delta PL) \quad (4.2)$$

with  $q$  being the elementary charge,  $k$  the boltzmann constant and  $T$  the temperature. This implies, that for  $T = 300$  K a tenfold increase in photoluminescence intensity will correspond to an increase in  $V_{OC}$  of about 60 mV for a recombination limited solar cell of the same material.

For our solar cells,  $V_{OC}$  is the most stable parameter, in relation to  $FF$  and  $J_{SC}$ . We measure the PL and  $V_{OC}$  of our perovskite solar cells in a wide range of  $V_{OC}$  from 950 to 1150 mV. We perform the PL measurement shortly (approximately 15 to 90 minutes) after measuring the  $V_{OC}$  to minimize effects of degradation and only use solar cells where no s-shape occurs in the light-IV, due to the uncertainty in the  $V_{OC}$  determination for these cells (see Figure 4.20).

The photoluminescence intensity (PL peakheight) in relation to the  $V_{OC}$  is displayed in Figure 4.21. We can clearly see, that in general the PL intensity increases with increasing  $V_{OC}$ , still there is a relatively large spread in the PL intensity for solar cells with similar  $V_{OC}$ . The red and blue lines are guides to the eye and represent the expected PL and  $V_{OC}$  correlation if the  $V_{OC}$  is limited only by recombination with a 60 mV increase in  $V_{OC}$  if the photoluminescence is tenfold higher. This result shows, that our  $V_{OC}$  is not only limited by nonradiative recombina-

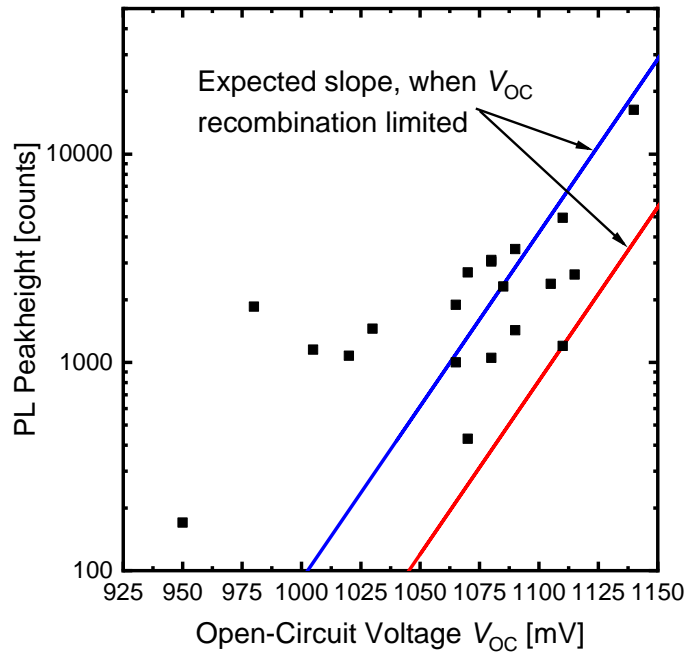


Figure 4.21: Photoluminescence intensity in respect to  $V_{OC}$  for different PSCs. The red and blue lines mark the slope of the expected increase according to Equation 4.2 for purely recombination limited solar cells.

tion. In comparison to the solar cell with the lowest PL peakheight compared to its  $V_{OC}$  (red line), which relates to the lowest amount of nonradiative losses in  $V_{OC}$ , the average (blue line) is about 40 mV lower. Some solar cells show  $V_{OC}$ s more than 100 mV lower compared to the  $V_{OC}$  potential of the red line in relation to their PL peakheight. The question arises, which factors contribute to the additional losses in  $V_{OC}$ .

Non recombination based losses in  $V_{OC}$  can stem from bad band alignment of the contact layers [145]. We use the same contact layers however for every cell (spiro-TTB as HTL, C60+BCP as ETL). This should result in a similar loss in  $V_{OC}$  for every cell and no variations between depositions are expected. There still is an uncertainty related to the photoluminescence measurement setup. The measured intensity could not be linear to the amount of emitted light. To investigate this, we perform measurements with a stable white light source in combination with different neutral density filters. The transmittance of the neutral density filters was measured with a Cary 5000 UV-VIS spectrophotometer beforehand, leading to a transmission of about 25%, 1% and 0.2% in the range of 700 to 800 nm. We then measured the light intensity of the white light source with our photoluminescence setup with and without the filters, leading to a wide range of photoluminescence intensities of about 35000 to 100 counts, so the measured intensity range displayed in Figure 4.21 is included. This measurements show a linear behaviour



#### 4.2. PSC SOLAR CELL STABILITY AND MEASUREMENT

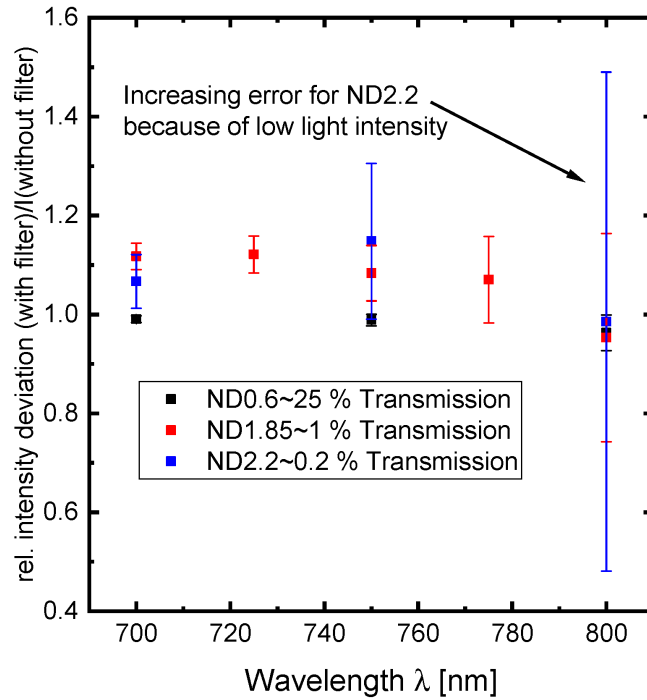


Figure 4.22: Intensity deviation of our PL setup for five different wavelengths from 700 to 800 nm. The relative intensity deviation (y-axis) was calculated as follows: Measured PL Intensity (with filter)/[Measured PL Intensity (without filter) · attenuation factor of the filter] and should be near to one.

of emitted light intensity to measured light intensity, as is shown exemplarily for the wavelength range of 700 to 800 nm in Figure 4.22. In addition, we measure the stability of the incident laser excitation (not shown here), which is also stable. We can therefore exclude that the measurement setup is responsible for the differences in photoluminescence intensity.

Unfortunately, we cannot identify which effects cause the varying loss in  $V_{OC}$  that is not caused by nonradiative recombination. There are however many reports showing that additional effects especially at the perovskite/contact layer interfaces are crucial for  $V_{OC}$  and device performance [118, 146]. Since we evaporate MAI in the same chamber as our contact layers, we could get an unintentional doping of the contact layers due to incorporation of MAI. Doping of contact layers is reported to affect the  $V_{OC}$  of the solar cells [147]. The photoluminescence measurements take place in ambient atmosphere, so diffusion of water from moisture can play a role as well. Additionally, mobile ion species, that we already identified to affect our solar cell performance, can influence the  $V_{OC}$  [142, 148].

#### *CHAPTER 4. CELL MEASUREMENTS OF PSCS*

This experiment shows again that optimising our processing and measurement methods and to remove as many uncertainty factors (e.g. moisture, MAI incorporation, ions etc.) as possible is crucial to understand the mechanics behind the cell parameter that is the most stable for our solar cells.

# 5 Optics of perovskite solar cells

In this chapter I will discuss several important aspects of optical simulations of perovskite solar cells.

The first part briefly explains the basic concept of optical simulations. It also includes an overview of main aspects of optical simulations using the perovskite solar cell design presented in this work.

In the second part I will discuss the extinction coefficient and refractive index of the materials in our solar cells, which we evaluate with spectroscopic ellipsometry and in some cases combined with transmission measurements.

The third part will be about optical simulations of our specific cells and discusses some limitations of our current measurements of the *EQE* of our solar cells.

In the fourth part, I will give a short outlook about planned tandem cell designs and their current generation and, for example, how front and backside texture improves tandem cell current.

## 5.1 Basics of optical simulation

Optical simulations, which we perform using either SunRays [149] or e-Arc [150], calculate the fraction of light of each wavelength that is transmitted, reflected or absorbed in the different layers of the solar cell.

The purpose of optical simulations for solar cells is to identify where light is absorbed or reflected and to optimise the layer structure for a maximum of absorbed light in one of the layers, in our case the perovskite. Light absorbed in the perovskite layer creates the charge carriers that produce the current generated by the solar cell. Because of the known photon density of the incoming sunlight, the AM1.5G spectrum, the absorbed light in the perovskite layer can be translated into the light generated current density of the solar cell.

Light absorbed in other layers than the perovskite can create charge carriers as well, these however do not account for the current generated in the solar cell. This process is called parasitic absorption. Light that is reflected or transmitted

does not increase the current density of the solar cell, too.

For the wavelength dependent absorption in the perovskite (or silicon in a silicon or tandem solar cell) the term external quantum efficiency ( $EQE$ ) is commonly used. The  $EQE$  multiplied with the AM1.5G spectrum yields the light generated current density of the solar cell.

In our optical simulations the light absorbed in the perovskite/silicon is treated as if every absorbed photon creates a pair of charge carriers that gets collected by the solar cells contacts. The actual (measured)  $EQE$  and current density of a solar cell is however also affected by non-optical parameters such as resistive losses or the diffusion length in the perovskite/silicon [151].

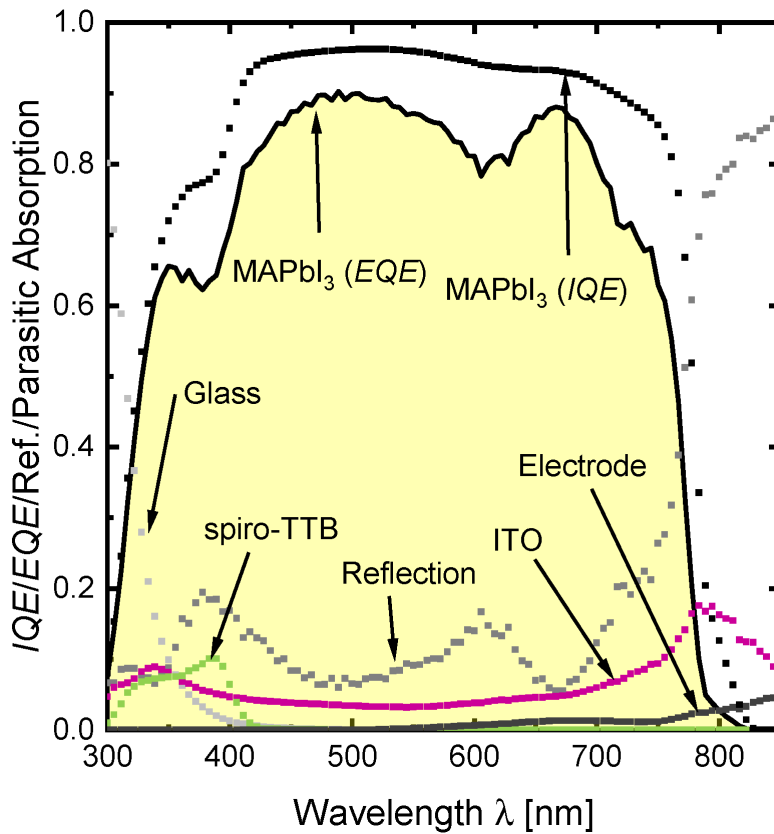


Figure 5.1: Optical simulation of our perovskite solar cell.

Our perovskite solar cell has the structure explained in chapter 2.2.1. The simulated fraction of light that is absorbed or reflected in each layer is depicted in Figure 5.1. The yellow area represents the fraction of light that is absorbed in the perovskite ( $EQE$ ). Additionally, the internal quantum efficiency ( $IQE$ ) is depicted, which is the fraction of light not reflected that is generating current in the solar cell ( $IQE = EQE / (1 - \text{Reflection})$ ).

## 5.2. COMPLEX REFRACTIVE INDEX

Layer	Reflection	Glass	SiO <sub>2</sub>	ITO	spiro-TTB
Current density [mA/cm <sup>2</sup> ]	6.18	0.14	0	2.06	0.14
Layer	MAPbI <sub>3</sub>	C60	BCP	Au	-
Current density [mA/cm <sup>2</sup> ]	21.75	0.01	0	0.21	-

Table 5.1: Total reflection and absorption in the different layers of a PSC processed in this work under AM 1.5G illumination.

Below a wavelength of 400 nm glass and spiro-TTB cause parasitic absorption. ITO creates parasitic absorption in the whole range from 300 to 850 nm and the electrode material from 600 to 850 nm. Reflection occurs at all wavelengths and increases to up to 80% for wavelengths above 700 nm.

For a solar cell with 700  $\mu\text{m}$  glass, 25 nm SiO<sub>2</sub>, 180 nm ITO, 10 nm spiro-TTB, 600 nm MAPbI<sub>3</sub>, 23 nm C60, 8 nm BCP and Au (Electrode) the total amount of absorbed or reflected photons is shown in Table 5.1 as current density. As depicted, the biggest current losses in our solar cell come from reflection due to the planar glass surface without an anti-reflective coating [152] and parasitic absorption inside the ITO. Glass, spiro-TTB and the electrode account for 0.5 mA/cm<sup>2</sup> and C60 and BCP for only 0.01 mA/cm<sup>2</sup> in total. Minimizing the reflection and the parasitic absorption in ITO is therefore the most effective way to improve the light generated current of our solar cells and will be discussed in chapter 5.3.2 .

## 5.2 Complex refractive index

For the optical simulation we need to know the complex refractive index of each material in our solar cell. To determine the complex refractive indices of the materials we perform spectroscopic ellipsometry measurements with a J.A. Wollam M-2000 ellipsometer and fit the data using WVase software. For each material we perform spectroscopic ellipsometry measurements on silicon and glass substrates and transmission and reflection measurements on glass substrates with a Cary 5000 UV-VIS photospectrometer. We check the resulting complex refractive indices and thicknesses of each material regularly (see e.g. chapter 2.2.3) after for example changes at the evaporation chamber with spectroscopic ellipsometry measurements on silicon substrates.

The typical thicknesses of spiro-TTB, C60 and BCP in our solar cells are 10, 23 and 8 nm and we can accurately describe films with these thicknesses with the complex refractive indices shown in Figure 5.2. All contact layers show semiconductor-

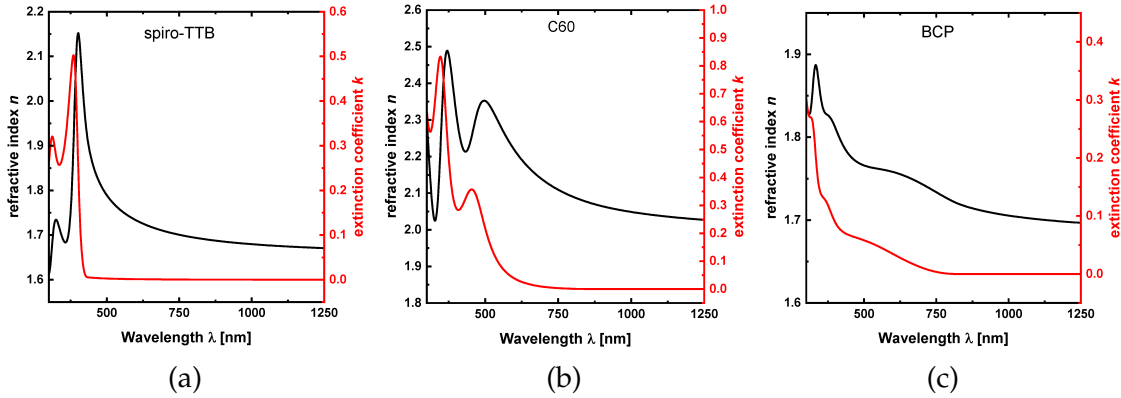


Figure 5.2: Complex refractive indices of (a) spiro-TTB, (b) C60 and (c) BCP

typical extinction in the UV-VIS range and no extinction in the infrared region. Similar data can be found in literature as well [153, 154, 155].

Small layer thicknesses can lead to an imprecise determination of the extinction coefficient. We therefore processed samples with about 100 nm of each material on a glass substrate and performed transmission and reflectance measurements to calculate the resulting absorption of each film (see Figure 5.3). Additionally the simulated absorption of 100 nm BCP with the complex refractive index determined from ellipsometry measurements (see Figure 5.2c) on a glass substrate is depicted. Simulated absorptions with the complex refractive indices for spiro-TTB, C60 and BCP all slightly differ from the actual absorption of the 100 nm thick films in Figure 5.3, with BCP being the most severe and therefore displayed.

However, deriving models from the 100 nm thick samples do not yield the correct complex refractive index to describe the typically deposited thinner contact layers. The most likely reason for these results is that the complex refractive index of the contact layers is not stable. We did not make any systematic assessment about how for example the source material for spiro-TTB, C60 and BCP, the layer thickness or prior depositions with MAI affect the refractive index.

The absorption in the contact layers in the solar cell only accounts for approximately  $0.15 \text{ mA/cm}^2$  in total for our current type of solar cells, mostly in spiro-TTB, as shown in Table 5.1. The deviations in the refractive index between the thicker and thinner films would only account for less than  $0.1 \text{ mA/cm}^2$  for our current solar cells, so we use the complex refractive indices shown in Figure 5.2. For other cell concepts or different thicknesses of the contact layers further experiments might be necessary, especially if C60 is used as a front contact.

For the optical simulations, we need the complex refractive indices of each ma-

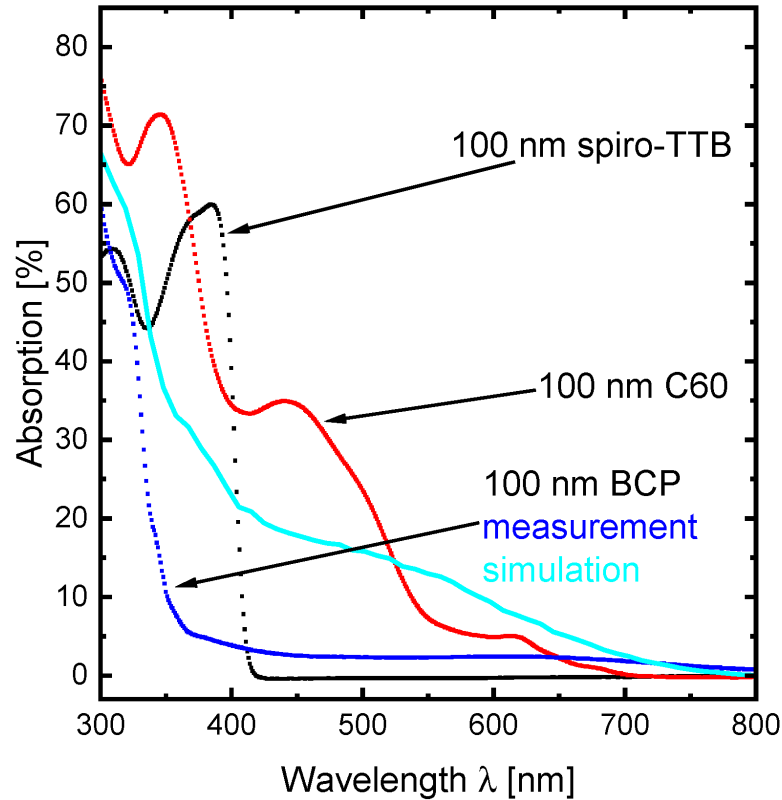


Figure 5.3: Measured absorption on 100 nm thick films of spiro-TTB, C60 and BCP and simulated absorption of 100 nm BCP using the data displayed in Figure 5.2c

material. We purchase the glass substrates coated with approximately 20 to 25 nm of  $\text{SiO}_2$  and 180 to 200 nm of ITO from PGO. We perform measurements to determine the refractive indices of the glass substrate itself and the ITO, shown in Figure 5.4. The supplier of the ITO coated glass processes the  $\text{SiO}_2$  and ITO in sequence and therefore we can not determine properties of this specific  $\text{SiO}_2$ . For the  $\text{SiO}_2$  we use data commonly used in literature [156]. We perform ellipsometry and transmission measurements on samples of several batches of ITO coated glass and there are no significant changes in the complex refractive index of the ITO.

The glass substrate is transparent above 350 nm, the ITO however absorbs light also in the visible and infrared region due to free carrier absorption common in TCOs [157].

For the electrode material (gold or copper), we use data from literature as well [158].

For the  $\text{MAPbI}_3$  perovskite several complex refractive indices, mostly for wet-chemical processed layers, are published [159, 160]. All of the published complex

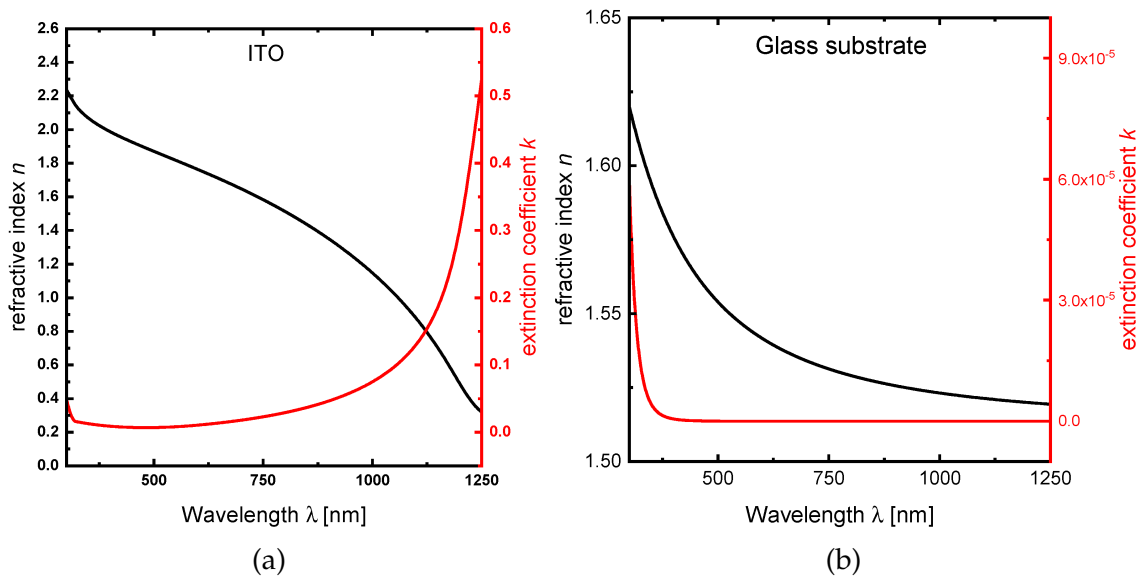


Figure 5.4: Complex refractive indices for (a) ITO and (b) the glass substrate for the ITO coated glass bought from PGO.

refractive indices differ a bit, which could be caused by uncertainties in determining the refractive indices with different ellipsometry models for example.

We perform ellipsometric measurements on coevaporated MAPbI<sub>3</sub> layers with MAI prepared at ISFH from different evaporation processes and the refractive index and extinction coefficient differs from process to process, as is shown in Figure 5.5.

These differences do not come from an uncertainty in the ellipsometry modelling. Rather, the complex refractive indices of the perovskites are not constant, likely due to varying PbI<sub>2</sub> excess and crystallinity of the material, as discussed intensely in chapter 3 and 4. There seems to be a maximum of the extinction coefficient from 500 to 800 nm. The best absorbing samples from ISFH and the literature data from Löper show this extinction [159]. The refractive index of the best absorbing MAPbI<sub>3</sub> measured at ISFH will be regarded as a stoichiometric perovskite in the following chapter for the sake of simplicity. The exact mechanisms behind the complex refractive index of perovskite thin films are complex and still not fully understood [161].

Another interesting aspect is the influence of the MAI source material, which I already discussed in chapter 3.1.2. For MAI that we bought from Lumtec and that is extensively used for high performing solar cells [39, 84] we measure very low extinction coefficients on many samples, as shown in Figure 5.6. The samples of process 1 to 3 were all processed with the same processing parameters, however



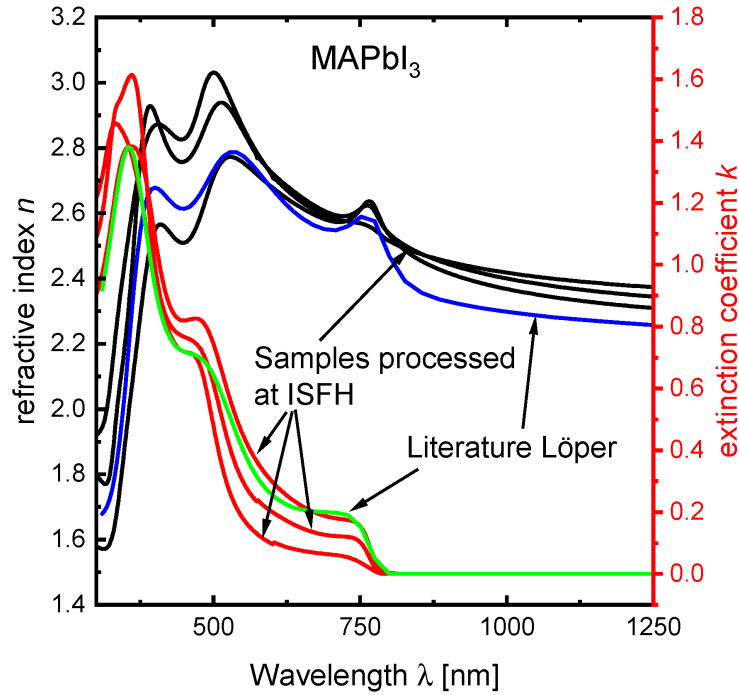


Figure 5.5: Complex refractive indices for  $\text{MAPbI}_3$  thin films processed at ISFH (red, black) and data published by Löper et al. ( $k$  green,  $n$  blue) [159].

the samples of process 2 and 3 (and of three other processes with Lumtec MAI not shown here as well) have basically no absorption below 550 nm. For process 3 we annealed the sample at 100 °C in  $\text{N}_2$  atmosphere after the first ellipsometry measurement. We can see that the sample of process 3 has a slightly higher absorption after annealing. We could not observe such a shift in extinction coefficient due to annealing in samples processed with our own MAI.

A possible explanation for this behaviour is that for the Lumtec MAI the  $\text{MAPbI}_3$  perovskite is not properly formed and the sample consists of MAI and  $\text{PbI}_2$  and we can partially convert the educts by annealing after the process. This is rather surprising, since other groups do not report any needed annealing step with Lumtec MAI for evaporated  $\text{MAPbI}_3$  [39, 84, 93]. Since the process parameters differed compared to our own MAI and the first cell results were underwhelmingly bad (below 1.5% efficiency) we did not make further experiments with Lumtec MAI.

### 5.2.1 Effective medium model

As stated above, for optical simulations of solar cells, the exact complex refractive index of each material is necessary. It is unfortunately not possible to derive the

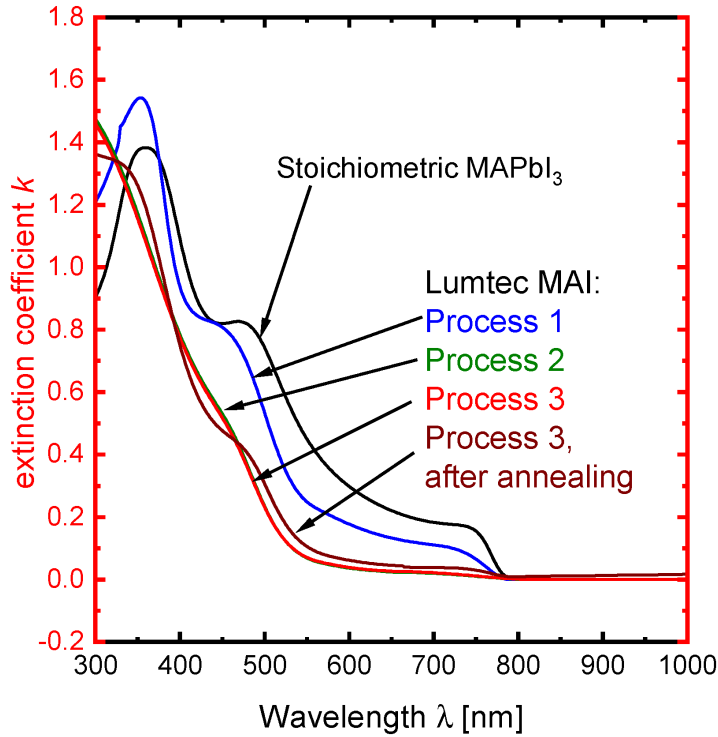


Figure 5.6: Extinction coefficient  $k$  for MAPbI<sub>3</sub> thin films processed at ISFH with MAI from Lumtec compared to stoichiometric MAPbI<sub>3</sub>.

exact complex refractive index of the perovskite layer in a solar cell without extra reference samples, which increases the processing and measuring time. To address the varying complex refractive indices of our deposited perovskite layers without the necessity of reference samples we use an effective medium model, which can describe the differences in extinction coefficients.

As discussed in chapter 3 and 4 the perovskites in our working solar cells have mostly an excess of PbI<sub>2</sub>. PbI<sub>2</sub> is transparent above 500 nm. The complex refractive index of PbI<sub>2</sub> compared to stoichiometric MAPbI<sub>3</sub> is displayed in Figure 5.7a. By using a linear combination for the complex refractive indices of PbI<sub>2</sub> and stoichiometric MAPbI<sub>3</sub> we can create an effective medium (EM) with different fractions  $x$  (with  $x$  from 0 to 1) of PbI<sub>2</sub> in MAPbI<sub>3</sub> to mimic the complex refractive index of a specific perovskite. The resulting refracting index  $n$  of the effective medium can be calculated with ( $k$  accordingly):

$$n_{EM}(\lambda) = (1 - x) \cdot n_{MAPbI_3}(\lambda) + x \cdot n_{PbI_2}(\lambda) \quad (5.3)$$

If we compare the resulting complex refractive index of an effective medium with about 50% PbI<sub>2</sub> to a perovskite with reduced absorption in the wavelength range of 500 to 800 nm (see Figure 5.7b) we can see that the extinction coefficients match

### 5.3. EQE MEASUREMENTS AND OPTICAL SIMULATIONS AT ISFH

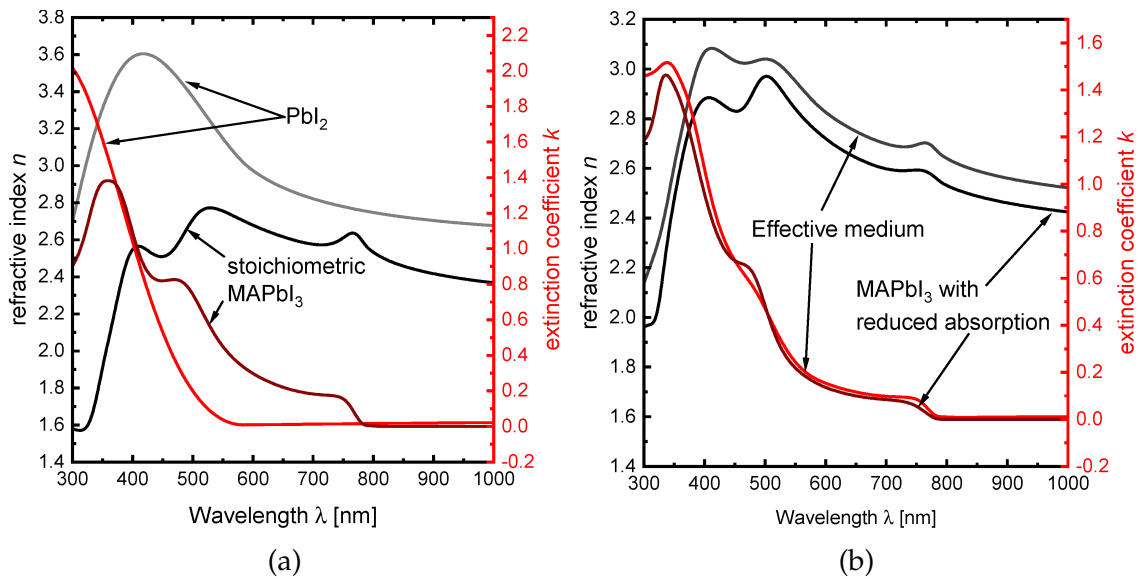


Figure 5.7: Complex refractive indices for (a)  $\text{PbI}_2$  and (b) an effective medium with 50%  $\text{PbI}_2$  compared to a measured perovskite with a similar extinction coefficient.

rather well. The refractive index of the effective medium is however higher than for the measured perovskite layer. This result indicates that the  $\text{PbI}_2$  rich perovskite layer is not only a combination of  $\text{PbI}_2$  and  $\text{MAPbI}_3$  but more complex. We can still use this approach for optical simulations of our solar cells, as I will show in 5.3.4..

## 5.3 EQE measurements and optical simulations at ISFH

### 5.3.1 Influence of the perovskite layer on current generation

We perform optical simulations for our cell design with a stoichiometric perovskite and an effective medium with a 50% excess of  $\text{PbI}_2$ , both being 600 nm thick, as depicted in Figure 5.8. The effective medium represents a perovskite layer with  $\text{PbI}_2$  excess. This results in a higher EQE and therefore possible solar cell current density of the stoichiometric  $\text{MAPbI}_3$  due to a higher absorption in the wavelength range of 550 to 800 nm. No differences occur for wavelengths lower than 500 nm, because all light that is not reflected or absorbed at the front side (glass, ITO, spiro-TTB) is absorbed in the perovskite layer in both cases. The differences in the longer wavelength range occur because the light is only partially absorbed in the perovskite layer in this region. This also results in a

higher reflection and parasitic absorption for wavelenths above 550 nm for the perovskite with  $\text{PbI}_2$  excess, due to more light being reflected at the electrode interface at the backside of the cell or absorbed in the C60, BCP or the electrode.

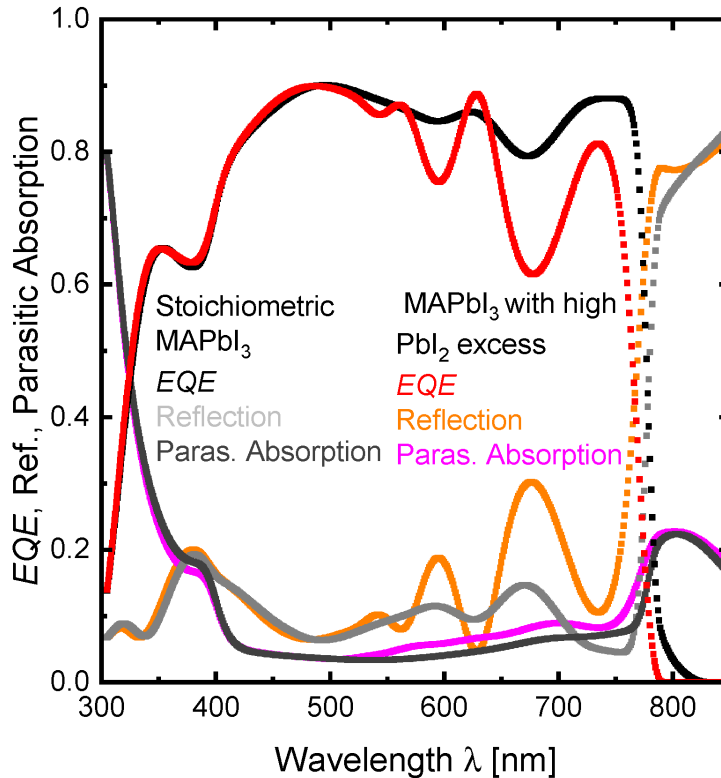


Figure 5.8: *EQE*, reflection and total parasitic absorption of a PSC with 600 nm stoichiometric  $\text{MAPbI}_3$  or a perovskite of the same thickness consisting of 50%  $\text{MAPbI}_3$  and 50%  $\text{PbI}_2$  (high  $\text{PbI}_2$  excess).

The possible current density of the perovskite with  $\text{PbI}_2$  ( $19.87 \text{ mA/cm}^2$ ) is about  $2 \text{ mA/cm}^2$  lower than of the stoichiometric  $\text{MAPbI}_3$  ( $21.75 \text{ mA/cm}^2$ ) mostly due to the increased reflection which increases by  $6.18$  to  $7.69 \text{ mA/cm}^2$ .

If we look at different perovskite thicknesses for both the stoichiometric  $\text{MAPbI}_3$  and the perovskite with  $\text{PbI}_2$  excess, which is displayed in Figure 5.9, we can see that the achievable current density increases for both with increasing perovskite layer thickness. The difference between both is decreasing with increasing layer thickness, however there still is a gap in possible current density of about  $1.5 \text{ mA/cm}^2$  at  $1000 \text{ nm}$  and about  $1 \text{ mA/cm}^2$  at  $10000 \text{ nm}$  (not displayed in the figure) perovskite thickness. Reaching  $22 \text{ mA/cm}^2$ , which we can reach with  $620 \text{ nm}$  of stoichiometric  $\text{MAPbI}_3$ , would require several  $\mu\text{m}$  thick layers of perovskite with  $\text{PbI}_2$  excess, which is not feasible. We therefore conclude that for a maximum current output stoichiometric  $\text{MAPbI}_3$  is needed and it cannot be adequately replaced by thicker  $\text{MAPbI}_3$  with  $\text{PbI}_2$  excess.

### 5.3. EQE MEASUREMENTS AND OPTICAL SIMULATIONS AT ISFH

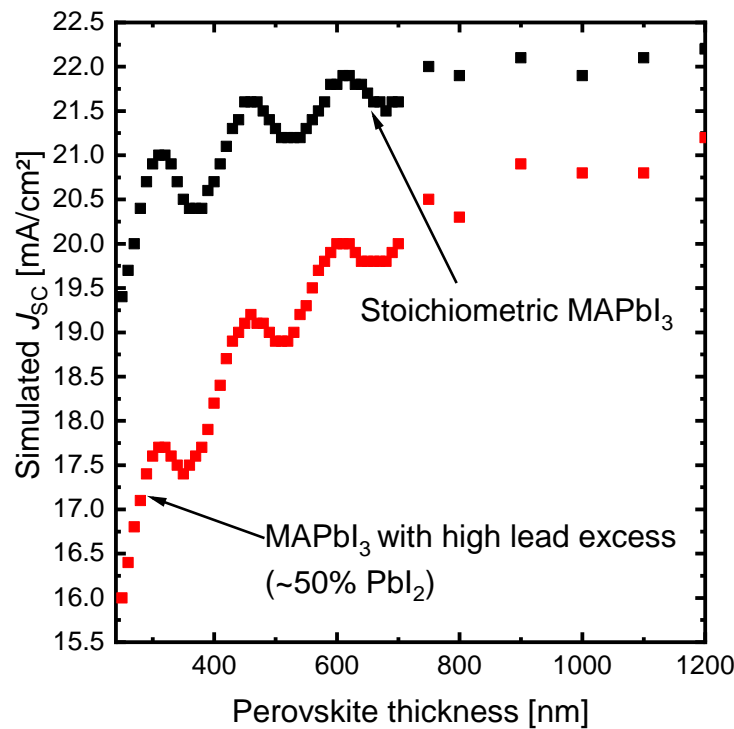


Figure 5.9: Achievable current density ( $J_{SC}$ ) for PSCs with stoichiometric MAPbI<sub>3</sub> and MAPbI<sub>3</sub> with 50% PbI<sub>2</sub> excess.

Further things to consider are the local maxima and minima of current density in Figure 5.9. These are caused by thin film properties of the perovskite film. As is displayed in Figure 5.10a, for different thicknesses of the perovskite the reflection and absorption in the perovskite near the band gap is heavily changing. The thin films of the PSC act as an anti-reflective coating of the electrode interface. Therefore changing the layer thickness of the perovskite produces maxima and minima of reflection at different wavelengths. The local maxima of current density in respect to the perovskite thickness in Figure 5.9 are produced by a minimum of reflection near the perovskite band gap (at about 780 nm), the minima vice versa. The overall reflection is decreasing with increasing perovskite thickness due to more light being absorbed in the perovskite and less light being reflected at the electrode interface. For increasing perovskite thickness the reflection decreases for wavelengths of 550 to 800 nm. Figure 5.10b shows this behaviour for PSCs with a minimum in reflection near the band gap. Controlling the perovskite thickness for optimised current gain is hence the more important, the thinner the perovskite gets, because the local maxima and minima are more pronounced.

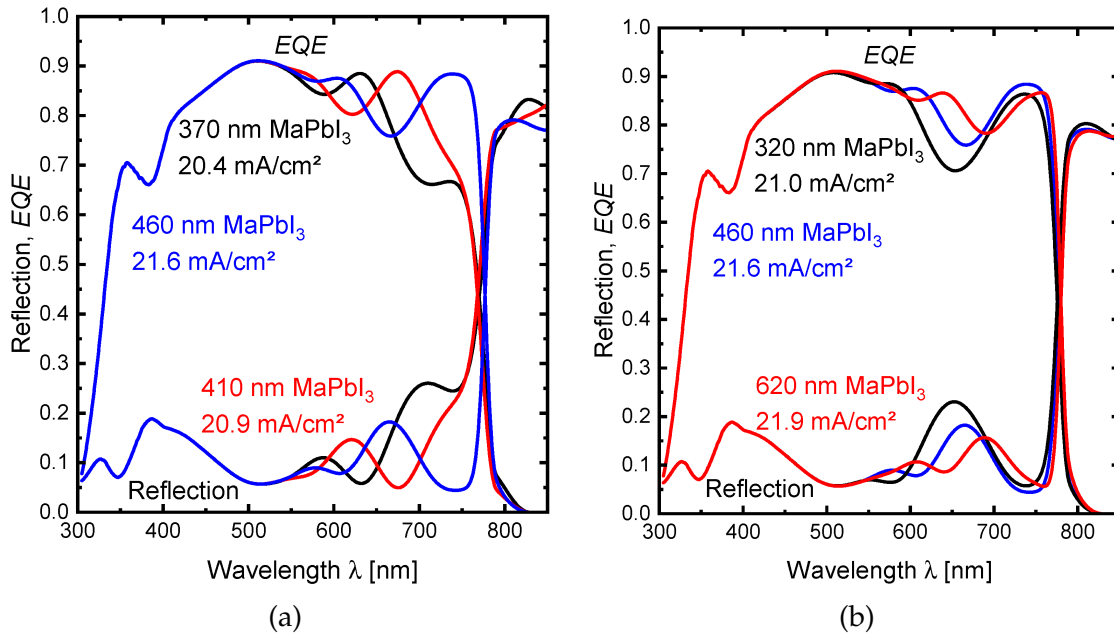


Figure 5.10: Simulated *EQE* and reflection of PSCs for (a) thicknesses producing local minima (370 nm) and maxima (460 nm) in the current output and (b) three consecutive local maxima (320 nm, 460 nm, 620 nm) in the current output.

### 5.3.2 Simulation study for optimised current generation

So far, I have primarily discussed the effects of the perovskite layer on current generation and concluded that a high absorption in the perovskite layer reduces backside reflection and parasitic absorption in the C60, BCP and electrode. To increase the possible cell current further, improvements on the front side (above the perovskite) are necessary. To reduce the front side reflection different methods for texturing the glass surface are discussed [20]. Another additive option is to deploy an anti-reflective coating (ARC) on the glass surface [152].

For the simulations here, since we have not developed any methods for texturing the glass surface, only the effect of the anti-reflective coating is considered. To reduce parasitic absorption we have to look at the different layers above the perovskite. The overall absorption in the glass is relatively small (about 0.15  $\text{mA}/\text{cm}^2$ ) and we only have one type of glass substrate because we purchase the ITO-coated glasses so no differences in material are evaluated here. The 10 nm thick spiro-TTB, which also accounts for 0.1 to 0.15  $\text{mA}/\text{cm}^2$  parasitic absorption, can be replaced by a self-assembled monolayer (SAM), which is considered to cause no parasitic absorption [30]. The ITO, which is attributing for about 2  $\text{mA}/\text{cm}^2$  of parasitic absorption is needed for current transport in the solar cell. Reducing the ITO thickness would increase the series resistance in ITO (as discussed in chapter 2.2.5), so a gain in current of the solar cell will cause losses in the fill factor.

### 5.3. EQE MEASUREMENTS AND OPTICAL SIMULATIONS AT ISFH

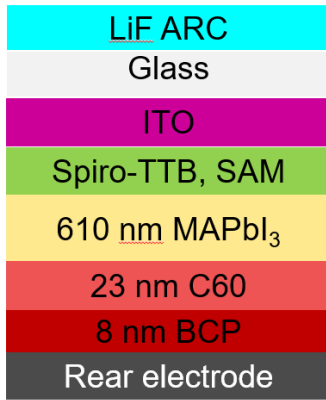


Figure 5.11: Simulated cell stack for the current optimisation for our PSCs.

We perform optical simulations with and without anti-reflective coating and with spiro-TTB or SAM to look at the individual effects of each. For the cells with anti-reflective coating we perform simulations with thinner ITO as well. For every simulation we use  $700 \mu\text{m}$  glass, 610 nm stoichiometric perovskite, 23 nm C60, 8 nm BCP and an Au electrode. The ITO thickness for the standard ITO is considered to be 180 nm, for the thin ITO about 50 nm, which is the optimum for both reduced reflection and parasitic absorption. The thickness of the anti-reflective coating (LiF, complex refractive index measured by me as well, but not shown in this work) is about 96 nm.

If we compare the different effects, we can see that replacing the spiro-TTB

Cell type #	1: No ARC, spiro-TTB, 180 nm ITO	2: No ARC, SAM, 180 nm ITO	3: ARC, spiro-TTB, 180 nm ITO	4: ARC, SAM, 180 nm ITO	5: ARC, spiro-TTB, 50 nm ITO	6: ARC, SAM, 50 nm ITO
Current density [mA/cm <sup>2</sup> ]	21.78	21.94	22.43	22.59	23.71	23.84
Difference to 1 [mA/cm <sup>2</sup> ]:	0	0.16	0.65	0.81	1.93	2.06
Difference to 2 [mA/cm <sup>2</sup> ]:	-0.16	0	0.49	0.65	1.77	1.9
Difference to 3 [mA/cm <sup>2</sup> ]:	-0.65	-0.49	0	0.16	1.28	1.41
Difference to 4 [mA/cm <sup>2</sup> ]:	-0.81	-0.65	-0.16	0	1.12	1.25
Difference to 5 [mA/cm <sup>2</sup> ]:	-1.93	-1.77	-1.28	-1.12	0	0.13
Difference to 6 [mA/cm <sup>2</sup> ]:	-2.06	-1.9	-1.41	-1.25	-0.13	0

Figure 5.12: Achievable current densities of our PSC with reduced reflection due to an anti-reflective coating and reduced parasitic absorption due to a thickness reduction in ITO or replacement of spiro-TTB with a SAM.

with a SAM yields a current gain of approximately 0.13 to 0.16 mA/cm<sup>2</sup>, an anti-reflective coating yields a current gain of 0.65 mA/cm<sup>2</sup> and lowering the thickness of the ITO increases the current by 1.25 to 1.28 mA/cm<sup>2</sup>.

In future, a more complex approach, which considers electrical parameters of the solar cell as well, is needed for optimisation of cell performance. The here presented approach only covers the optimisation of short circuit current for our lab-scale perovskite solar cells that we could reach with the tools currently available

at ISFH. The highest performing published evaporated PSC with  $\text{MAPbI}_3$  has a  $J_{SC}$  of  $22.43 \text{ mA/cm}^2$  [84], which we could exceed with the methods presented here.

### 5.3.3 EQE measurements of perovskite solar cells at ISFH

So far, we have only discussed optical simulations with the material properties of our solar cell stack. To perform simulations of actual solar cells we need the *EQE* and reflectance data as well.

The reflectance is a purely optical measurement and therefore relatively straightforward, when provided with the right tools, and will not be further discussed here. The *EQE* measures the ratio of generated charge carriers to incoming photons of each wavelength. It is not purely optical, but relies on other electrical properties of the solar cell as well, for example the diffusion length in the charge carrier generating material (which can exceed  $100 \mu\text{m}$  in  $\text{MAPbI}_3$  [162] and is mostly neglected due to the much thinner layer thickness of less than one micrometer).

The *EQE* is more complex to measure as well. For the commonly used differential *EQE* a bias light (white light) is applied to the solar cell at short circuit and for each wavelength a small amount of monochromatic light is added to this bias light [163]. The difference in solar cell current between pure bias light and bias light plus the monochromatic light is then measured for each wavelength.

The result of this measurement gives a differential quantum efficiency, which has to be normalised to the short circuit current density of the actual solar cell. The in-device normalisation of the *EQE* measurement setup is adjusted for a reference silicon solar cell, which might not be correct for perovskite solar cells. As I discussed in chapter 4.2.2, the short circuit current density of our solar cells is not constant for the current measurement conditions.

In this chapter I will discuss which information we can extract from the *EQE* measurement for a better understanding of our solar cells. A more detailed analysis purely about the *EQE* measurements at ISFH was done in the master thesis of Moritz Engl [65]. Most of the experiments shown here are from samples of MAI Batch 1+2, with a light-IV measurement from  $J_{SC}$  to  $V_{OC}$ .

To determine the optimal bias-light conditions we perform *EQE* measurements on a perovskite solar cell for different bias light intensities. The solar cell depicted in Figure 5.13 shows the highest *EQE* for a bias light of 0.05 suns and no significant change of the *EQE* shape for all bias lights. Other cells show a similar



### 5.3. EQE MEASUREMENTS AND OPTICAL SIMULATIONS AT ISFH

behaviour in regard to the shape, but have the highest  $EQE$  at different bias light intensities [65]. We therefore assume that the shape is correct and the wavelength dependent quantum efficiency is measured correctly.

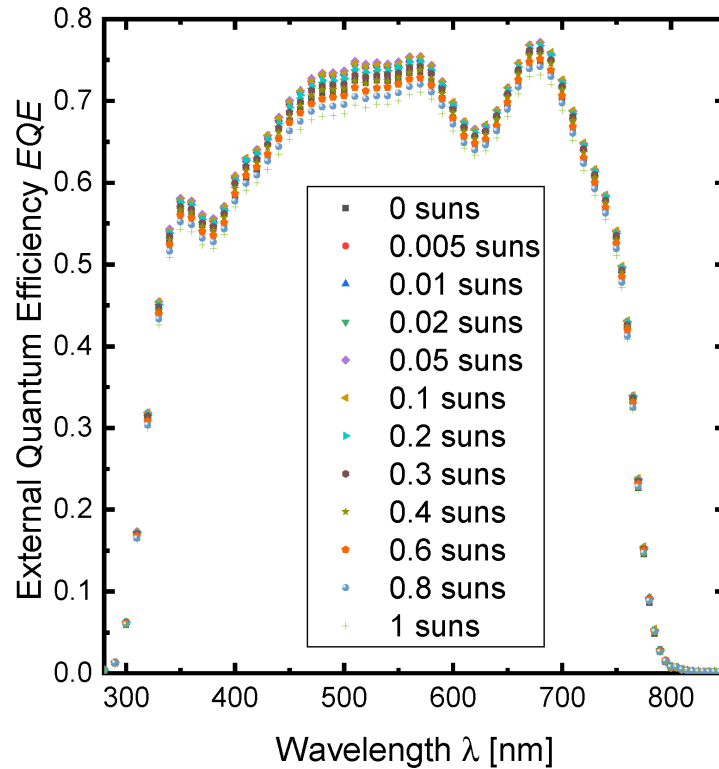


Figure 5.13: Differential  $EQE$  of one PSC measured at ISFH for different bias light intensities, measured from 0 to 1 suns without any further measurements in between.

If we scale the measured  $EQE$  to the  $J_{SC}$  extracted from the light-IV curve measured in forward direction we often get a scaled  $EQE$  with the  $EQE$  exceeding 1 for some wavelengths, as illustrated in Figure 5.14a, which is not possible. This is an indication that the measured short circuit current is often overvalued and not correct. Currently (Q1/2022), due to the lack of high performing cells and the heterogeneity of their behaviour as well as their degradation during air exposure or measurements (likely due to moisture or ions), no way to accurately determine the  $J_{SC}$  could have been established at ISFH and is still work in progress. An accurate description of the  $J_{SC}$  (and the  $EQE$  as well) from the light-IV measurement will only be possible when the solar cells have a stable current output and do not degrade during the measurement, which means that as long as we measure a significant hysteresis or a decrease in current output over time [65], no quantitative determination of the  $J_{SC}$  or  $EQE$  is possible.

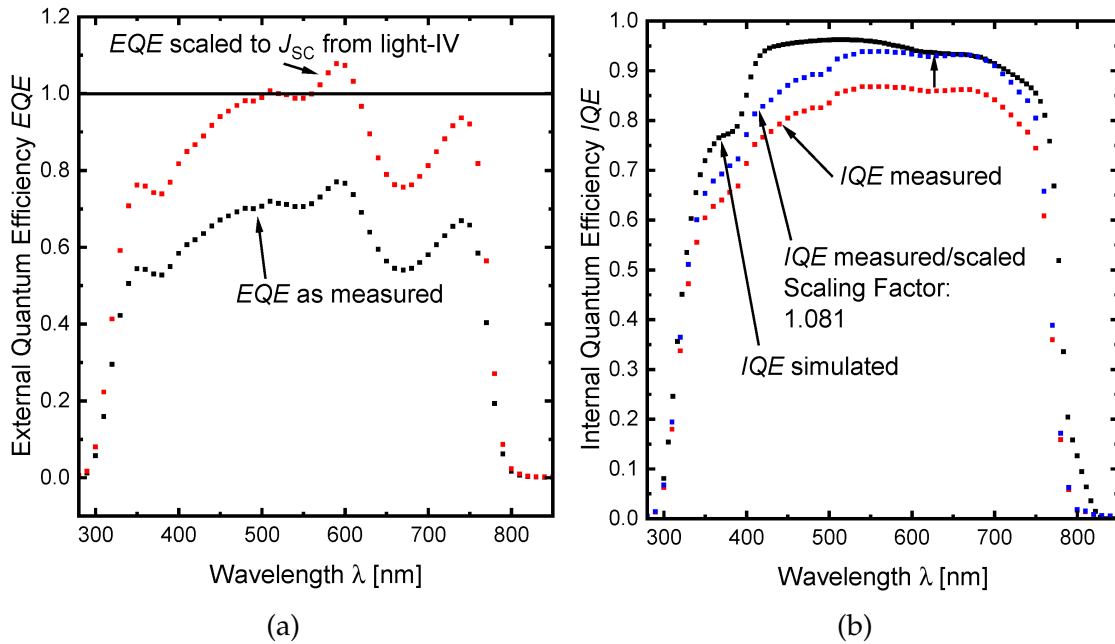


Figure 5.14: (a) Measured  $EQE$  scaled to the  $J_{SC}$  from the light-IV measurement of one of our PSCs. (b) Measured, simulated and scaled measured  $IQE$  of one of our PSCs.

A quantitative use of the  $EQE$  for simulation purposes is therefore currently not meaningful. We can still qualitatively assess the  $EQE$ , though. The  $EQE$  is formed by the incoming light minus the reflected light (which can be directly measured and is considered in the optical simulation as well), the parasitic absorbed light (featured in the optical simulation) and the light absorbed in the  $MAPbI_3$  that does not contribute to the solar cells current.

If we look at the internal quantum efficiency ( $IQE$ ), the reflection is already subtracted out and we can qualitatively check for additional current losses by comparing the measured to a simulated  $IQE$ . To account for the changing perovskite thicknesses and refractive indices (see chapter 3.1.2 and 5.2), we use the measured reflection data for the device simulation, which will be explained in 5.3.4 in detail.

To estimate a maximal reasonable scaling factor of the measured  $IQE$  we scale the measured  $IQE$  up until it matches the simulated  $IQE$  at one wavelength, which is shown in Figure 5.14b. This way, we can identify where the main current losses besides the parasitic absorption in the optical simulation occur. The scaling factor determined by this method is the upper limit of a scaling factor for the  $IQE$ , because the simulated  $IQE$  has no current losses besides the parasitic absorption in the other layers.

### 5.3. EQE MEASUREMENTS AND OPTICAL SIMULATIONS AT ISFH

We can learn from this method that the biggest loss in quantum efficiency in the measured solar cell compared to the simulation is in the wavelength range of 300 to 500 nm, which indicates a current loss at the front side.

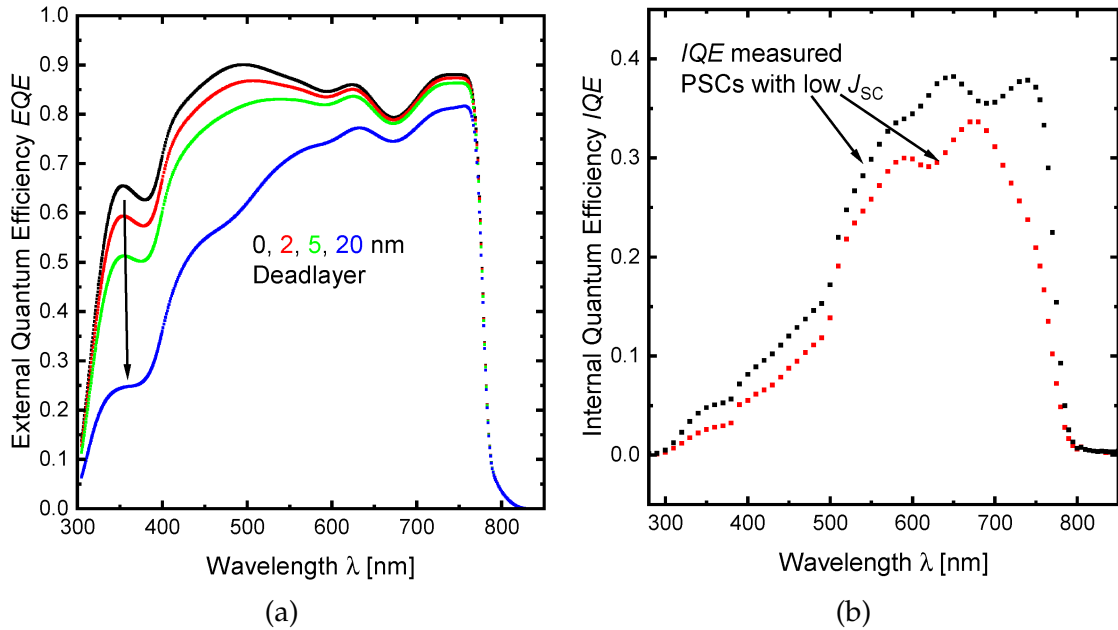


Figure 5.15: (a) Simulated  $EQE$  for a PSC with different thicknesses of a perovskite deadlayer at the perovskite/spiro-TTB interface causing parasitic absorption instead of contributing to the  $EQE$ . (b) Measured  $IQE$  of two PSCs with a  $J_{SC}$  below  $10 \text{ mA/cm}^2$ .

To describe this current loss, the front side of the perovskite between spiro-TTB and the bulk perovskite is treated as if it would cause parasitic absorption due to charge carriers generated in that layer instantly recombining. The effect of this so called deadlayer on the  $EQE$  of our perovskite solar cell is shown in Figure 5.15a. A detailed explanation with several example solar cells can be found in the master thesis of Dennis Winter [164]. This deadlayer concept is also used in literature for other thin-film [165, 166] and perovskite solar cells [167].

For bad performing solar cells with measured short circuit current densities of  $10 \text{ mA/cm}^2$  or lower in the light-IV measurement this effect gets even more pronounced, as depicted in Figure 5.15b. For these devices, the non-scaled  $IQE$  is also much lower across the whole measurement range in comparison to for example the cell displayed in Figure 5.14b. At this point, we could not clearly identify a particular reason for the varying current densities of different solar cells. The most likely causes are degradation of the contact layer interfaces, especially at the front side due to interface contamination with e.g. MAI or  $\text{PbI}_2$ , or effects due to

moisture or ionic movement. It is however important to note that this effect is not caused by the spiro-TTB/perovskite interface in general but due to our improper processing and measurement conditions [91].

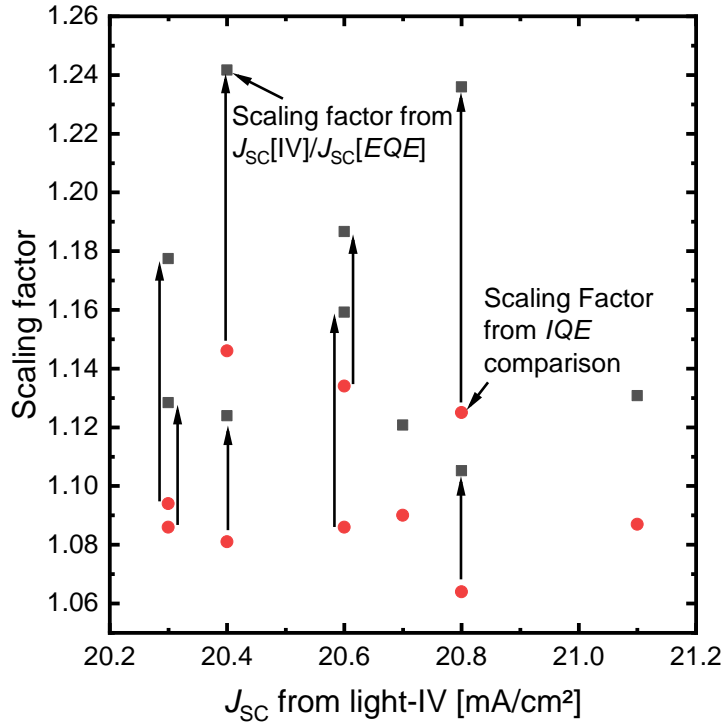


Figure 5.16: Scaling factor from  $J_{sc}(EQE)$  scaled to the measured  $J_{sc}$  from the light-IV (grey) and maximum possible scaling factor of the same cells in comparison to optical simulations (red). PSCs where the scaled  $EQE$  would exceed 1 were not considered in this evaluation.

If we compare the scaling factor from the comparison of measured and simulated  $IQE$  for different solar cells with the scaling factor we get from using the short circuit current density  $J_{sc}$  from the light-IV measurement, which is displayed in Figure 5.16, we can see that for every single solar cell the scaling with the light-IV exceeds the maximum possible scaling factor from the comparison to the simulated  $IQE$ .

This means that the light-IV measurement from  $J_{sc}$  to  $V_{OC}$ , which measures from -0.1 to 1.3 V, systematically overestimates the short circuit current by at least 5-15%. Measuring from  $V_{OC}$  to  $J_{sc}$  (1.3 to -0.1 V) does overestimate the  $J_{sc}$  from comparisons with the  $IQE$  as well in some cases.

The overall shape of the  $EQE$  of all of our cells is similar to the ones shown in Figure 5.13 and Figure 5.15b. Cells with a high  $J_{sc}$  are looking more like in Figure 5.13 and cells with a low  $J_{sc}$  more like in Figure 5.15b. It is also not clear if

### 5.3. EQE MEASUREMENTS AND OPTICAL SIMULATIONS AT ISFH

our cells degrade during the *EQE* measurement. In the master thesis of Moritz Engl the *EQE* seemed rather stable in comparison to the  $J_{SC}$  from the light-IV [65]. Unfortunately most cells he measured in his work were low performing with efficiencies rarely exceeding 10%, which makes the significance of this measurements questionable for higher performing cells. Any effort to correctly quantify the *EQE* is futile when the generated current density in our solar cells is not stable.

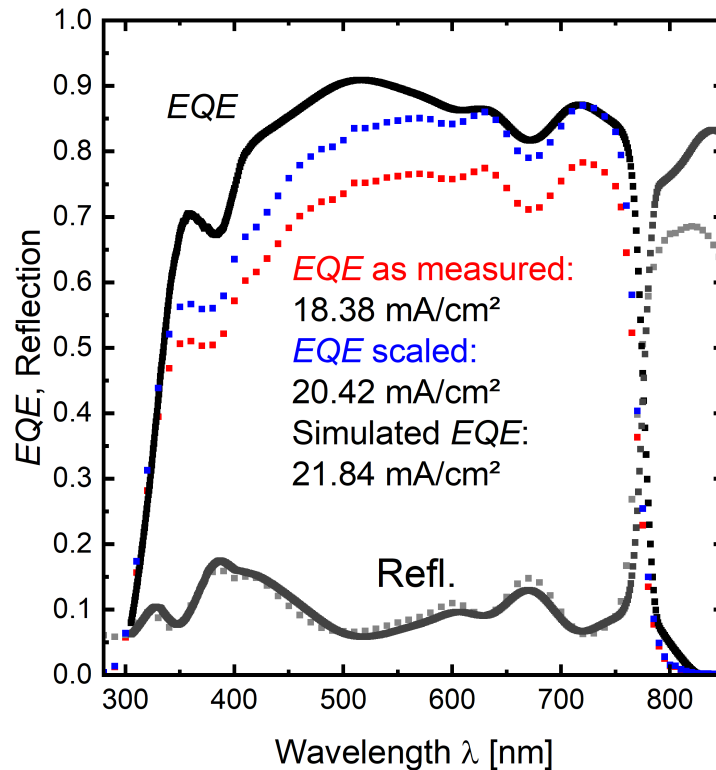


Figure 5.17: Measured, simulated and scaled measured *EQE* and measured and simulated reflection of the champion PSC in this work.

If we look at our current champion cell with up to 17% efficiency (see chapter 4.1.6), the  $J_{SC}$  in four light-IV measurements is 19.97, 19.98, 19.97 and 19.28  $\text{mA}/\text{cm}^2$ . The third measurement was in  $J_{SC}$  to  $V_{OC}$ , the other in  $V_{OC}$  to  $J_{SC}$  direction. Figure 5.17 shows the measured, the measured scaled to the maximal reasonable current and simulated *EQE* as well as measured and simulated reflection of this solar cell. From this we can see that the measured  $J_{SC}$  (19.98  $\text{mA}/\text{cm}^2$  or lower) is actually in the possible range of  $J_{SC}$  (max. 20.42  $\text{mA}/\text{cm}^2$ ) with this *EQE*, regardless of the measurement direction, contrary to all solar cells in Figure 5.16. The current generation is still limited to current losses on the front side. These results highlight that by improving our solar cell processing to high efficient cells with less stability issues due to moisture and ions we can likely achieve

a quantitative description of the EQE as well.

### 5.3.4 Approach to optical simulation for PSCs

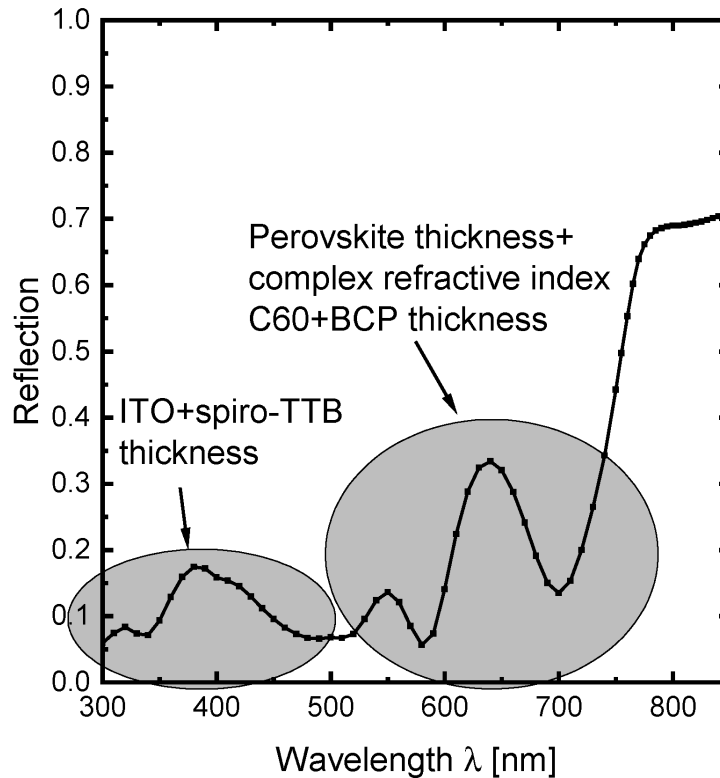


Figure 5.18: Reflection measurement of a PSC with wavelength ranges marked that we can use for the thickness determination of each layer in our solar cells.

As discussed in chapter 3.1.2 and chapter 5.2 the perovskite layer in our solar cells has a varying thickness and absorption and we can determine both by using the reflection measurement of a solar cell. For our common single-junction cell stack (see chapter 2.2.1) we can deduce the thicknesses of the different layers by looking at the interference pattern at different wavelengths, which is displayed in Figure 5.18. For wavelengths below 500 to 550 nm all light that is transmitted in the perovskite layer is absorbed in the perovskite, hence interference only occurs due to reflection at the interfaces up to the spiro-TTB/perovskite interface. In our present solar cells the spiro-TTB thickness is also constant in respect to the accuracy of the optical simulation and only the ITO thickness needs to be adjusted and ranges from 180 to 195 nm. For wavelengths of 550 to 780 nm the light is partially transmitted through the perovskite layer and reflected up to the electrode interface. Therefore, all layers contribute to the interference pattern. Since we have already determined the front side thicknesses (ITO and spiro-TTB) only the

### 5.3. EQE MEASUREMENTS AND OPTICAL SIMULATIONS AT ISFH

perovskite layer and the C60 and BCP remain. The thickness of C60 and BCP is constant in respect to the accuracy of the optical simulation as well. The thickness variation in the deposition of spiro-TTB, C60 and BCP is 1 to 2 nm, which is displayed exemplarily for spiro-TTB in chapter 2.2.3.

The remaining free parameters are only the perovskite thickness and its complex refractive index.

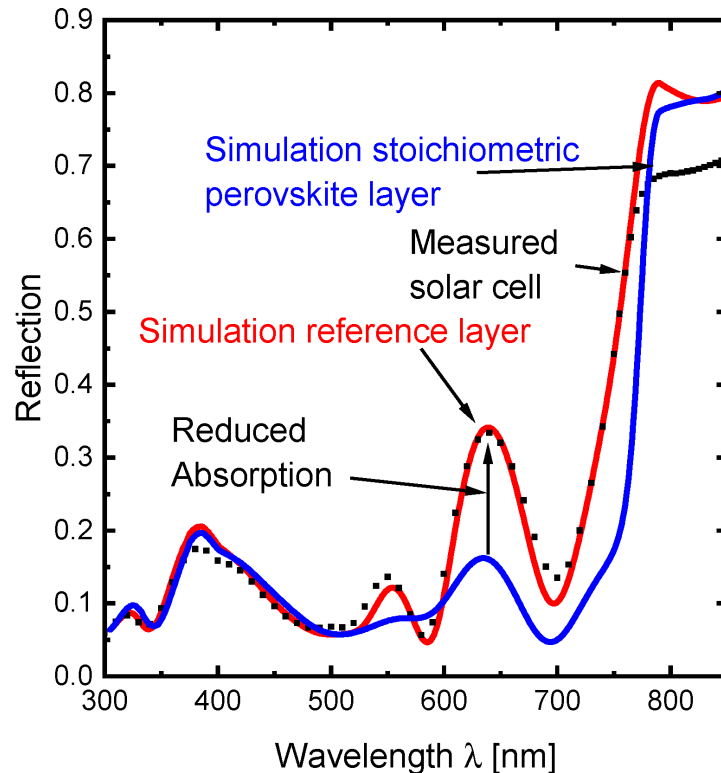


Figure 5.19: Reflection measurement of a PSC (black) compared to simulations with a stoichiometric perovskite (blue) or a reference sample from the same perovskite deposition (red).

Figure 5.19 shows the measured reflection of a perovskite solar cell in comparison to simulations with both a stoichiometric perovskite and a reference perovskite from the same perovskite deposition as the solar cell. Both have a similar thickness but a different complex refractive index.

We can see that up to 500 nm, the simulated reflection of both perovskites is similar. For higher wavelengths the stoichiometric perovskite has a reduced reflection due to its higher absorption. As shown in Figure 5.10 previously, the perovskite thickness mainly attributes to where minima or maxima of reflection occur due to the different optical path length in the material. We can then fit the measured reflection of each solar cell by matching the interference pattern for the correct

perovskite thickness first and then use the effective medium approach (see chapter 5.2.1) to specify the perovskite absorption.

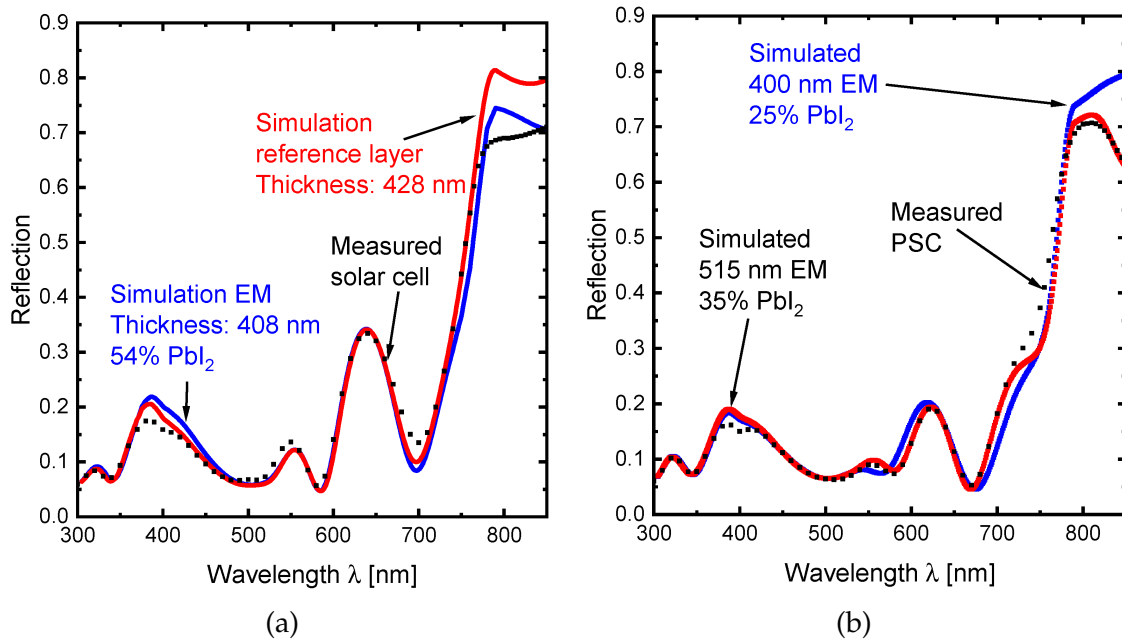


Figure 5.20: (a) Measured reflection of a PSC (black), compared to a simulation with a reference layer (red) or the effective medium (blue). (b) Measured reflection of a PSC (black) with two possible perovskite thicknesses from simulation approaches using an effective medium with different amounts of  $\text{PbI}_2$  (red, blue).

If we compare simulations with a reference layer to simulations with an effective medium, as is displayed in Figure 5.20a, we can see that the short wavelength reflection is increased in the effective medium in comparison to the reference layer. This is due to the higher refractive index of the effective medium compared to the reference layer, which increases the reflection at the spiro-TTB/perovskite interface. This effect occurs at all wavelengths. However, for the longer wavelengths it is superimposed by the varying absorption in the perovskite layer.

The higher refractive index of the effective medium also decreases the perovskite thickness in the simulation. Maxima and minima in the reflection are dependent on the optical path length in the perovskite thin film and a higher refractive index causes the same optical path length for a thinner film.

Taking both the higher reflectance at the interface and the optical path length into account, the effective medium overestimates the  $\text{PbI}_2$  amount by up to 5% (from comparing the difference in interface reflection of spiro-TTB and different perovskites to the difference in reflection due to different  $\text{PbI}_2$  amounts in the effective medium) and underestimates the layer thickness by up to 10% (from



### 5.3. EQE MEASUREMENTS AND OPTICAL SIMULATIONS AT ISFH

comparing the simulated layer thicknesses to SEM measurements or ellipsometry measurements of reference layers) for the so far simulated solar cells. The effect gets more severe, the more  $\text{PbI}_2$  is used in the effective medium.

When we use the reflection measurement to determine the perovskite thickness with optical simulations using an effective medium, we can get similar looking results for a thinner perovskite with higher absorption (less  $\text{PbI}_2$  in the effective medium) and for a thicker perovskite with lower absorption, as shown in Figure 5.20b. The sample thickness should in these cases be determined with SEM measurements.

In many of the images shown in this chapter, the simulated and measured reflection do not match accurately for wavelengths above 780 nm, respectively the perovskite band gap. In most cases, the simulated reflection is higher than the measured reflection. Since the optical parameters of every layer in the cell are known, the most likely explanation for this behaviour is parasitic absorption at the electrode. Since this parasitic absorption presumably also happens for shorter wavelengths but is superimposed by the variance in perovskite absorption an overestimation of the perovskite absorption in the simulation could occur.

This effect is however very differently pronounced for different cells, for example the ones in Figure 5.20b and Figure 5.17, where the first one has a good agreement of simulation and measurement for the long wavelength range and the latter one has more than 10% difference in the measured and simulated reflection.

#### 5.3.5 Thickness gradient

As mentioned in chapter 2.2.2, due to the processing geometry of our perovskite evaporation chamber, there is a thickness gradient in the deposited layers. The electron and hole transporting layers are too thin to see this effect in reflection measurements of our solar cells, but for the perovskite layer we can actually quantify the thicknesses of each solar cell on a substrate.

Figure 5.21 shows the measured reflection of four perovskite solar cells on the same substrate. We can see that the long-wavelength interference pattern shifts, which is caused by a thickness gradient in the perovskite layer. In this example, there is approximately a 23 nm thickness gradient, which is about 5% of the overall thickness.

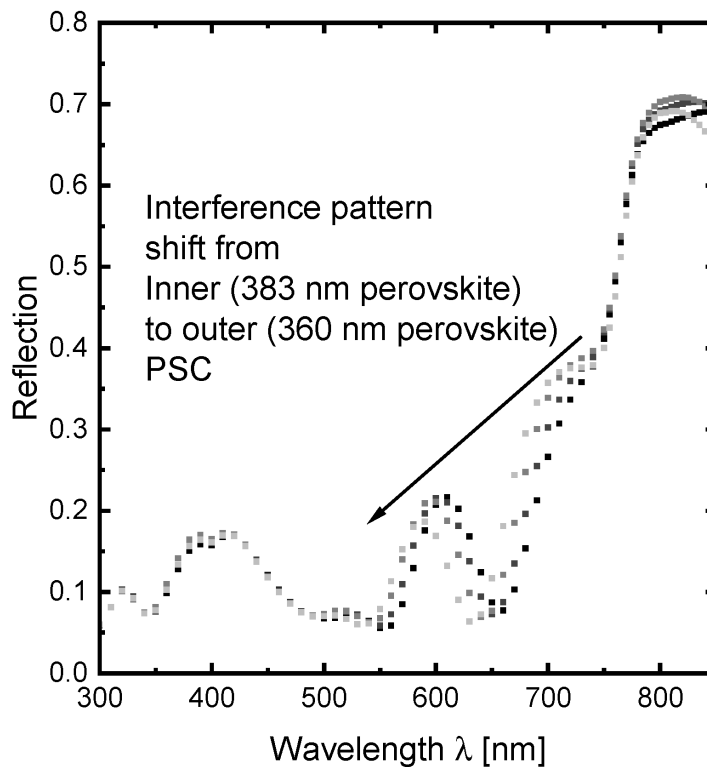


Figure 5.21: Reflection measurements of four solar cells on the same substrate, showing a switching reflection pattern caused by a thickness gradient in the perovskite layer.

### 5.3.6 EQE and reflection - long term stability

As discussed in 4.2.2, our solar cells degrade over time after metallisation, not only in ambient but in a glovebox atmosphere as well. We can see this behaviour not only in the light-IV measurement, but in the *EQE* as well. Figure 5.22 shows the measured (unscaled) *EQE* as well as the reflection of the same solar cell. The first measurement was taken immediately after the metal deposition, the second measurement after approximately one month of storing in a  $N_2$ -filled glovebox. We can see that the *EQE* dropped by about 30% over almost the whole wavelength range, with a more pronounced decrease in the shorter wavelength range (350 to 550 nm) and less decrease near the perovskite band gap (700 to 780 nm). The reflection was relatively similar even after one month, which means that the perovskite (or contact layers) did not drastically change in their bulk properties. This indicates that the degradation occurs mainly at the interfaces or due to increased ion concentrations, which I already discussed in chapter 4.2.2 as a common problem of perovskite solar cells [62, 63]. Since the *EQE* loss is more pronounced for shorter wavelengths, a degradation at the perovskite/HTL interface is likely.

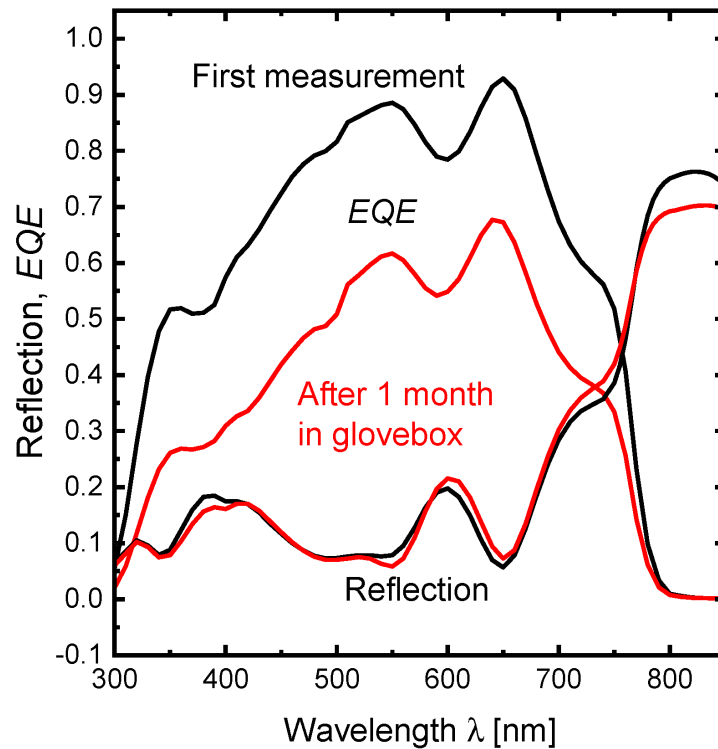


Figure 5.22: Measured *EQE* and reflection of the same PSC directly after metallisation (black) and after storage (red) in a glovebox for about a month.

The most noticeable difference in the reflection is below the perovskite band gap for the solar cell measured after one month. As already discussed in 5.3.4 this is likely caused by additional parasitic absorption not accounted in the optical model. At this point we do not know for certain what causes this parasitic absorption. The most likely cause for this is the formation of metal iodide at the electrode [136], as discussed in chapter 4.2.2 and/or the diffusion of metal into the ETL [34, 38].

In future, a better understanding of the degradation processes at the interfaces is crucial for the development of efficient solar cells. Long-term *EQE* and reflection measurements could help to identify degradation processes, as shown exemplarily here.

### 5.3.7 Different perovskite band gaps

For perovskites with different band gaps due to different perovskite compositions, so called multi-cation and/or multi-anion (MKMA) perovskites [168], with the methods presented so far, reference samples for each band gap are needed. Determining the complex refractive index of the perovskite for each process will

likely not be a practical solution, though.

A workaround for a perovskite with unknown complex refractive index is to use the complex refractive index of a known perovskite and to shift the complex refractive index until it matches the band gap of the unknown perovskite. A similar concept is published for CIGS solar cells [167]. For the two co-evaporated perovskites MAPbI<sub>3</sub> and FAPbI<sub>3</sub>, which differ in band gap by approximately 0.1 eV or 50 nm (1.5 eV or 830 nm for FAPbI<sub>3</sub>, 1.6 eV or 780 nm for MAPbI<sub>3</sub>), the initial and shifted extinction coefficient is depicted in Figure 5.23a.

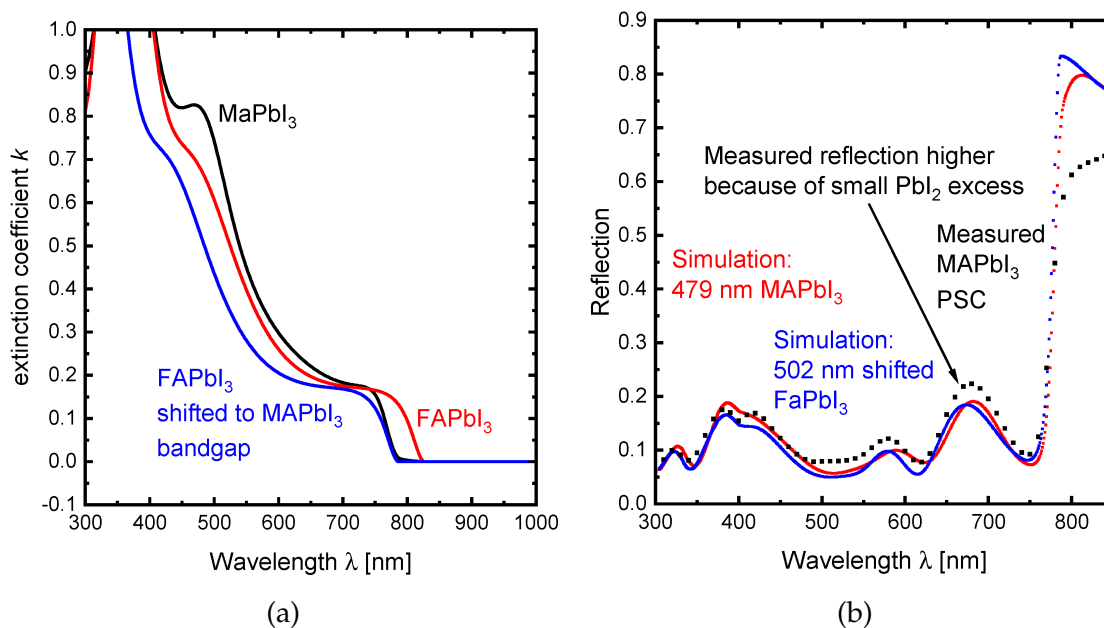


Figure 5.23: (a) Extinction coefficient of MAPbI<sub>3</sub>, FAPbI<sub>3</sub> and FAPbI<sub>3</sub> shifted to the band gap of MAPbI<sub>3</sub> (b) Measured reflection of a PSC simulated with either MAPbI<sub>3</sub> or shifted FAPbI<sub>3</sub> as perovskite layer.

With this shifted band gap for FAPbI<sub>3</sub>, we can fit the reflection pattern of a MAPbI<sub>3</sub> solar cell (see Figure 5.23b). With this approach it is possible to get a relatively good estimation of the band gap of the perovskite as well as the approximate thickness and amount of absorption of the perovskite. This information can then be used to optimise the perovskite processing.

We can see from the figure that the thicknesses of both perovskites differ about 5%, which is due to the higher refractive index of MAPbI<sub>3</sub> (not shown here). In future, a viable trade-off between the number of reference samples and the amount of band gap shifting has to be determined for MKMA perovskites processed at ISFH.

## 5.4 Optical simulation of tandem cells

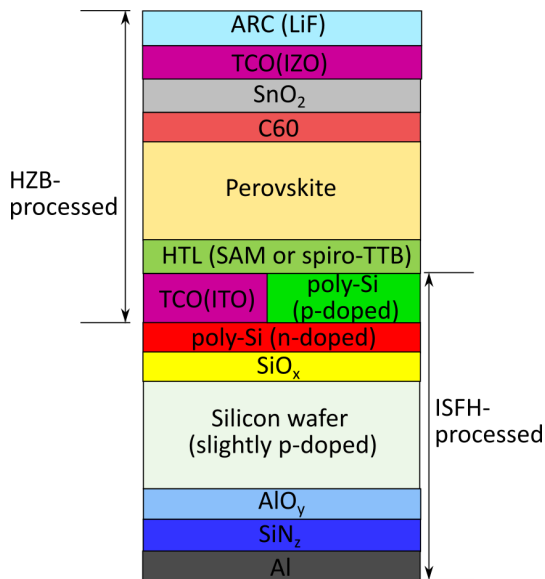


Figure 5.24: Tandem cell stacks simulated in this work.

Unfortunately, at the time of writing this thesis, there have been no tandem cells with the top (perovskite) cell made at ISFH. This is due to issues with short-circuiting and the lack of necessary deposition tools, as mentioned in the introduction. Tandem solar cells with ISFH bottom cells and the top cell made at HZB were recently published [169]. In this chapter, I will discuss the influence of textured/non-textured silicon surfaces on front and back side and the impact of the recombination junction between top and bottom solar cell on the current generation of the tandem solar cell. The bot-

tom cell featured in this approach has a design based on a PERC solar cell, with polycrystalline (poly) silicon on the front contact [12, 100, 170]. For the top cell the recently reported cell design of HZB is used, which could reach efficiencies of over 29% combined with a SHJ solar cell [11]. The material properties of the different layers in the top cell were given to us by Silvia Marotti from HZB within the framework of the P3T project and are not further shown or discussed here.

Figure 5.24 shows the tandem cell stack for the optical simulations performed in this chapter. Lithium fluoride (LiF, 100 nm) serves as anti-reflective coating, indium zinc oxide (IZO, 100 nm) as front contact, tin oxide ( $\text{SnO}_2$ , 20 nm) as protection layer for C60 and the perovskite, 18 nm C60 as ETL and the MKMA perovskite (varying thickness for current matching, about 300 to 450 nm) as top cell absorber with 10 nm spiro-TTB or a SAM as HTL. 20 nm ITO or p-doped poly-silicon in combination with n-doped poly-silicon (50 nm) serve as recombination layer and electron contact of the bottom cell. These are followed by a thin silicon oxide (1.5 nm  $\text{SiO}_x$ ), 160  $\mu\text{m}$  of silicon as bottom cell absorber, and the rear side passivation of 15 nm aluminum oxide ( $\text{AlO}_y$ ) and 100 nm of silicon nitride ( $\text{SiN}_z$ ). For the solar cells with rear side metallisation we use a 100 nm thick aluminum layer on the back side. There are a few approximations in this simulation that deviate from a functioning solar cell. The silicon solar cell has laser contact openings on the rear side that create an aluminum back surface field for example

[171], which is not included in this simulations for the sake of simplicity.

### 5.4.1 Impact of texture and parasitic absorption

An industrial PERC solar cell features a textured front side and planar back side [100]. For the top cell processing, which is often done with a wet-chemical approach, a planar front side is common to smoothly deposit the top cell stack [11]. Currently, different concepts of top and bottom cell texturing are discussed, but a texture is needed to minimize reflective losses [103, 172]. To investigate the effect of a textured surface we perform optical simulations for planar, rear side (RS), front side (FS) and both side (BS) textured perovskite-silicon tandem solar cells. To achieve current matching between both subcells for each structural type, we adjust the perovskite thickness so that the current in top and bottom cell is similar. We perform both simulations for a metallised and non-metallised rear side. The resulting cell current and reflection and transmission losses are displayed in Figure 5.25.

Structure	Current top cell mA/cm <sup>2</sup>	Current bottom cell mA/cm <sup>2</sup>	Reflection mA/cm <sup>2</sup>	Transmission mA/cm <sup>2</sup>
Planar, w/o RS metallisation	17.13	17.11	2.97	6.29
Planar, w RS metallisation (Al)	17.75	17.78	7.5	0
RS textured, w/o RS metallisation	18.87	18.83	3.41	1.55
RS textured, w RS metallisation (Al)	18.82	18.72	3.71	0
FS textured, w/o RS metallisation	19.51	19.59	2.84	0.37
FS textured, w RS metallisation (Al)	19.51	19.44	2.71	0
BS textured, w/o RS metallisation	19.22	19.16	0.45	3.54
BS textured, w RS metallisation (Al)	19.91	19.9	1.17	0

Legend: RS: rear side, FS: front side, BS: both side

Figure 5.25: Simulated current density for planar and textured tandem solar cells with the cell stack depicted in Figure 5.24. The current density in the solar cells is color coded from low (red) to high (green).

As we can see in comparison to the planar structure, we achieve an increase in current of about 1 mA/cm<sup>2</sup> with a rear side texture, an increase of about 1.7 mA/cm<sup>2</sup> with a front side texture and an increase of about 2.1 mA/cm<sup>2</sup> with a both side textured solar cell.

A rear side metallisation increases the current density by about 0.7 mA/cm<sup>2</sup> for the planar and both side textured cell types and has only a small effect on the one

side textured cells.

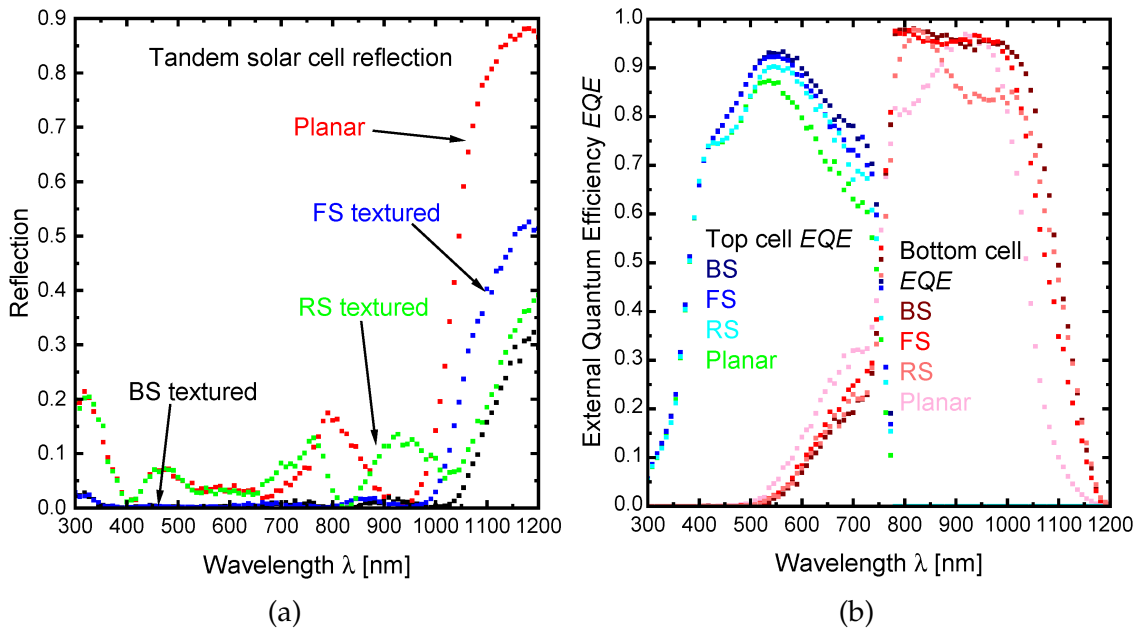


Figure 5.26: Simulated (a) Reflection and (b) *EQE* for the tandem solar cells with planar, FS, RS and BS texture with full area rear side metallisation.

If we look at the losses due to reflection in Figure 5.26a, we can see that a rear side texture does decrease the reflection for wavelengths above 900 nm compared to a planar structure. The reflection up to 900 nm only changes because of the changes in perovskite thickness. There is both reflection at the front side of the cell as well as reflection due to the perovskite/silicon solar cell interface, which we will discuss in detail in chapter 5.4.2.

The light trapping effect of the texture affects only the long-wavelength photons that are not absorbed in the first passing of the cell stack for the rear side texture, in comparison to the front side texture or both side textured solar cells.

The front side textured solar cells and the both side textured solar cells have therefore both almost no reflection below a wavelength of 1000 nm. Solely at wavelengths above 1000 nm the both side textured solar cell has a lower reflection. The associated *EQEs* of the four cell types are depicted in Figure 5.26b. The top cell *EQE* is all light that is absorbed in the perovskite, the bottom cell *EQE* all light that is absorbed in the silicon in the optical simulation. We can see that every texture increases the long-wavelength bottom cell *EQE* significantly due to the reduced reflection. The planar rear side and rear side texture however have a reduced top and bottom cell *EQE* within a wavelength range from 400 to 1000 nm

compared to the front side and both side textured solar cell due to the increased reflection at the top cell interfaces.

The difference in current between the front side textured and both side textured solar cell stems only from the reduced reflection for wavelengths above 1000 nm.

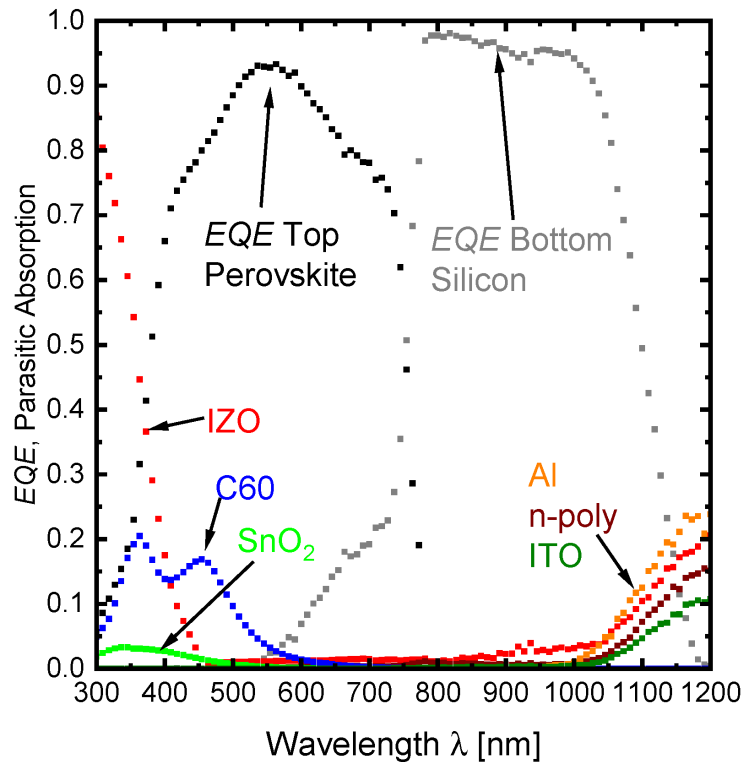


Figure 5.27: EQE and parasitic absorption in the tandem solar cell with BS texture and RS metallisation.

For the both side textured solar cell with metallised backside, the current losses due to parasitic absorption are displayed in Figure 5.27. LiF, SiN and  $AlO_x$  are transparent in the optical model and do not cause any parasitic absorption.

At the short wavelength range of 300 to 450 nm, we can see that IZO, C60 and  $SnO_2$  cause parasitic absorption of most incoming light. C60 even causes parasitic absorption at a wavelength range up to 600 nm. From 600 to 1000 nm only a small fraction of light is absorbed in the IZO.

For wavelengths above 1000 nm, IZO, ITO, n-poly and aluminum cause parasitic absorption.

The amount of absorbed light, converted to current density for each layer, is displayed in Table 5.2.

Since the light between 300 and 400 nm is partially lost in a solar module due to absorption in the encapsulation or glass [173], the absorption in the IZO and



#### 5.4. OPTICAL SIMULATION OF TANDEM CELLS

Layer	Current Density [mA/cm <sup>2</sup> ]
Perovskite	19.91
Silicon	19.90
IZO	2.06
SnO <sub>2</sub>	0.14
C60	1.29
ITO	0.38
poly-Si	0.66
Al	0.9

Table 5.2: Total light absorption in the layers shown in Figure 5.27

SnO<sub>2</sub> would be severely lowered. The most sufficient layer to improve or replace is the C60, which is also limiting the cells  $V_{OC}$  [174], because of its absorption in the 400 to 550 nm wavelength range. Finding a suitable replacement for C60 is therefore a further step towards better PSCs.

#### 5.4.2 Influence of recombination junction and current optimisation in tandem solar cells

Another cell concept for a tandem solar cell is the replacement of the ITO layer with a heavily p-doped poly silicon. The concept of a n- and p-doped silicon recombination junction between a perovskite and silicon solar cell was first proposed in 2015 [175]. The exact design with a p-type silicon wafer, a PERC rear side and a doped poly-silicon tunneljunction was first proposed by Peibst et. al in 2019 [170]. There are currently (Q1/2022) no working tandem solar cells processed with this configuration at ISFH, however a similar cell concept featuring doped amorphous silicon with solar cell efficiencies of over 25% was demonstrated by Sahli et al. [7, 176].

I performed optical simulations for the poly silicon used for the recombination junction of the tandem solar cell design depicted in Figure 5.24. In this design, the working top cell of HZB is used, ITO and the SAM HTL are replaced by spiro-TTB and p-poly, similar to the cell concept of Sahli et al. [7]. The material parameters used for the poly-silicon are for highly doped p-type and n-type poly silicon developed in the 27plus6 project (FKZ 03EE1056A) and will not be further discussed here. For the other layers we use the data used in chapter 5.4.1 as well. For the poly silicon we use thicknesses of 10 to 50 (p-poly) or 10 to 100 nm (n-poly), which is the thickness range currently evaluated at ISFH for this recombination junction. Other publications present 30/30 nm as a thickness [177], so the

thicknesses represented here are most likely in a reasonable range.

If we look at the current densities achievable with the poly silicon recombina-

Thickness p-poly	Thickness n-poly	Current top cell	Current bottom cell	Absorption p-poly	Absorption n-poly
nm	nm	mA/cm <sup>2</sup>	mA/cm <sup>2</sup>	mA/cm <sup>2</sup>	mA/cm <sup>2</sup>
10	10	20.01	19.99	0.45	0.02
20	10	19.91	19.93	0.84	0.02
50	10	19.59	19.57	1.88	0.02
10	50	19.99	19.92	0.45	0.09
20	50	19.88	19.79	0.86	0.09
50	50	19.51	19.51	1.9	0.1
10	100	19.94	19.87	0.45	0.18
20	100	19.77	19.83	0.87	0.18
50	100	19.48	19.48	1.93	0.19

Figure 5.28: Tandem cell current and absorption in poly silicon for a p-n poly silicon recombination junction on a both side textured tandem solar cell.

tion junction for a both side textured cell with the cell design similar to the one in chapter 5.4.1, which is given in Figure 5.28, we can see that for thin p-poly current densities of 19.9 mA/cm<sup>2</sup> are achievable, even with thick n-poly. For 50 nm p-poly however, the tandem cell current decreases to about 19.5 mA/cm<sup>2</sup> for all n-poly thicknesses. This is because the p-poly causes a much higher parasitic absorption than the n-poly with about 0.45 mA/cm<sup>2</sup> compared to 0.02 mA/cm<sup>2</sup> per 10 nm layer thickness.

In Figure 5.29 the wavelength dependent absorption in the poly silicon layers is displayed. We can see that the p-type poly silicon not only absorbs more light at a wavelength range of 500 to 1000 nm for comparable thicknesses, but that for wavelengths higher than 1000 nm, where the n-type poly silicon is nearly transparent, a sharp increase in absorption occurs. This is due to heavy doping in the p-type poly silicon, which causes free carrier absorption, similar to TCOs [178].

For 20 nm thick p-poly and 50 nm n-poly the achievable currents for rear and front side textured, as well as planar silicon substrates, all with metallised back side, are summarized in Figure 5.30. We can see, that the differences in achievable current density between the four substrate types are similar to the cells discussed in chapter 5.4.1.

These results clarify that highly doped poly silicon can cause considerable amounts of parasitic absorption and has to be carefully assessed with optical simulations

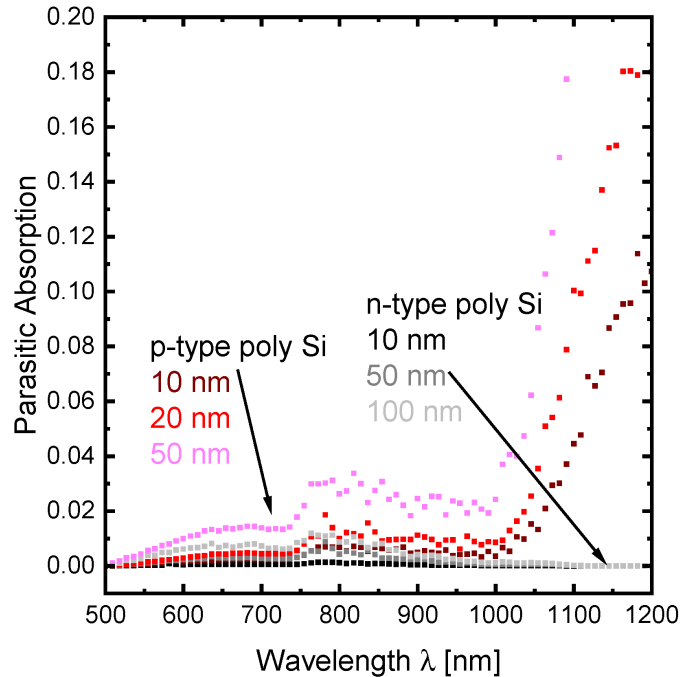


Figure 5.29: Parasitic absorption in n- and p-poly silicon with different thicknesses. For wavelengths under 500 nm, all light is absorbed in the perovskite. Therefore no light can be absorbed in the poly silicon and this wavelength range is not displayed in the figure.

in future tandem solar cell design concepts, but has the potential to replace the TCO without additional losses if it is thin enough.

### 5.4.3 Current matching in tandem solar cells

For a two-terminal tandem solar cell, the current is limited by the lower current of both subcells. So far, in all tandem simulations we have optimised the perovskite thickness for a matching current. In reality, current matching is not easily achieved and can heavily decrease cell performance [169].

As discussed in chapter 3.1.2, the perovskite thickness with our co-evaporated MAPbI<sub>3</sub> process is not constant. To evaluate the effect of a changing perovskite thickness on a two-terminal tandem solar cell we perform simulations with the both side textured and rear side textured variant of the solar cell design presented in chapter 5.4.1. We pick those two as a comparison to show the influence caused by front side reflection changes due to interference, which is present in the rear side textured, but not in the both side textured solar cell.

Figure 5.31 shows the tandem cell current density for different perovskite thicknesses for both cell types. With increasing perovskite thickness the absorption in

Structure	Current top cell	Current bottom cell	Absorption p-poly	Absorption n-poly
20 nm p-poly, 50 nm n-poly	mA/cm <sup>2</sup>	mA/cm <sup>2</sup>	mA/cm <sup>2</sup>	mA/cm <sup>2</sup>
BS texture with RS metallisation	19.88	19.79	0.86	0.09
FS texture with RS metallisation	19.4	19.48	0.76	0.1
RS texture with RS metallisation	18.66	18.69	0.69	0.09
Planar with RS metallisation	17.59	17.54	0.38	0.11

Figure 5.30: Tandem cell current and absorption for 20 nm p-poly and 50 nm n-poly silicon for tandem solar cells with planar and textured surfaces.

the perovskite layer increases as well. This leads to a change in current density in both subcells for changing perovskite thicknesses. Since the subcells are series connected in a two-terminal configuration, the subcell with the lower current output limits the current output of the overall device. For thin perovskite layers, the perovskite subcell limits the device current (perovskite limited) for a thick perovskite layer the silicon subcell (silicon limited).

For the both side textured solar cell, the thickness dependency of the current density is linearly decreasing for the silicon and perovskite limited side. Fitting with a linear function yields a slope of  $-0.0129 \pm 0.0007$  mA/cm<sup>2</sup> per nm perovskite thickness for the perovskite limited and  $-0.0079 \pm 0.0003$  mA/cm<sup>2</sup> per nm perovskite thickness for the silicon limited side. These results indicate, that for the both side textured solar cell, if the perovskite deposition process has variations in thickness, it is beneficial to aim for medium perovskite thicknesses in the silicon limited range if you want to maximize the current density from your average solar cell.

This is a quite obvious result, since the amount of light absorbed in any material generally follows the Lambert-Beer law, which results in lesser absolute differences of absorption in a material with two different thicknesses the thicker the material is.

For the rear side textured sample the slope is not linear anymore because of interference effects, that also influence the generated tandem cell current. In the case of our tandem cell, the current density follows a linear behaviour for a perovskite thickness of 360 nm to 420 nm and 420 nm to 450 nm. This behaviour can dif-

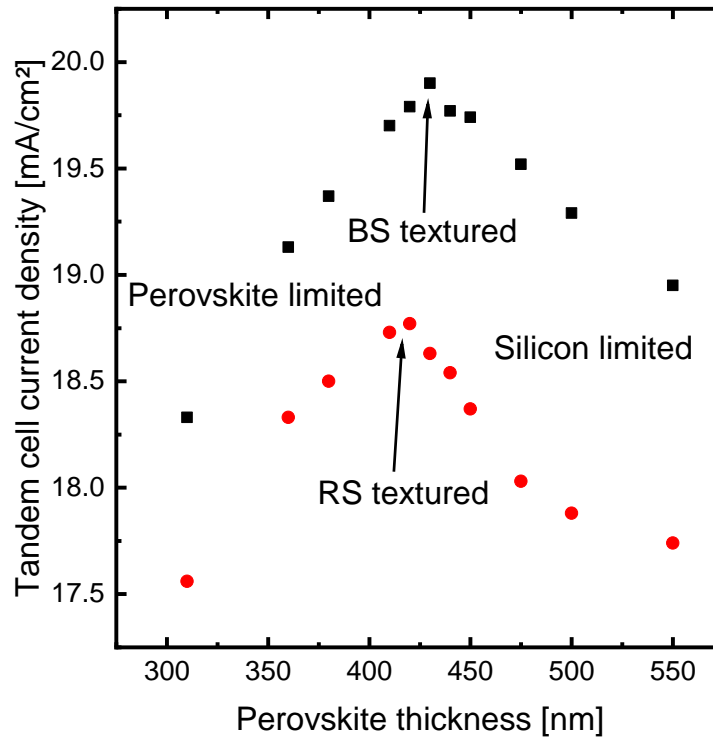


Figure 5.31: Resulting tandem solar cell current density for a RS and BS textured two-terminal tandem solar cell.

fer for other perovskites and/or cell designs. Using the data points here gives a slope of  $-0.0075 \pm 0.0004$  mA/cm<sup>2</sup> for the perovskite limited and  $-0.0135 \pm 0.0005$  mA/cm<sup>2</sup> for the silicon limited side. In this case, if you want to maximize the average current output of your solar cells, it is beneficial to use an average perovskite thickness slightly on the perovskite limited side.

This example shows that optical simulations can provide important information to optimise processing conditions for tandem solar cells, especially if the reproducibility of some process steps is questionable. In real ambient conditions, optimising the current density, generated in a two-terminal solar cell, is more complex. For example different angles and varying spectral composition of incoming light, diffuse radiation and shading also have to be considered. Varying environmental conditions will decrease the efficiency of a two-terminal tandem solar cell optimised for the AM1.5G spectrum (as done in this work) due to changing currents generated in both subcells. Therefore the current density optimisation has to be made taking real illumination data into account. A way to circumvent current matching issues for tandem cells could also be to use 4-terminal or 3-terminal solar cells, as proposed in [179].

## 5.5 Chapter summary

Determining the complex refractive index of the perovskite is rather complex, because different perovskite depositions yield perovskite layers with differences not only in layer thickness but especially in long wavelength absorption. I therefore use an effective medium approach consisting of stoichiometric  $\text{MAPbI}_3$  and  $\text{PbI}_2$  to model perovskites with a varying absorption.

By comparing optical simulations with *EQE* and light measurements of our perovskite solar cells we can see that the *EQE* is reduced qualitatively in the short wavelength range. This likely stems from parasitic absorption, occurring near the spiro-TTB/perovskite interface at the solar cell front side. A qualitative description of this behaviour is given with the introduction of a perovskite deadlayer, which was first demonstrated by Dennis Winter for our solar cells [164].

When scaling the *EQE* of our solar cells to the short circuit current measured in the light-IV and comparing the resulting *IQE* to an *IQE* from optical simulations, we can determine the overestimation of the  $J_{SC}$  from the light-IV to be at least 10 to 15% for measurements in forward scan direction.

Since the *EQE* cannot be scaled correctly for now, I present an alternative approach to optical modelling by just using the reflection measurement. With this approach, a quantitative description of the varying perovskite thicknesses and absorptions is possible.

For tandem solar cells, I highlight the importance of a textured surface, which increases the achievable tandem cell current by up to  $1.7 \text{ mA/cm}^2$  in comparison to a planar surface.

Replacing the ITO with heavily p-doped poly silicon as recombination layer between both subcells can lead to similar tandem cell currents, if the p-doped poly silicon is thin enough.

I also explain the difficulties of current matching for tandem solar cells and the importance of optical simulations to optimise the current output of tandem solar cells.

# 6 Summary: Results and outlook

## 6.1 Results

In this thesis, I have depicted the progress we made with the processing and measurements of perovskite solar cells from Q4/2019 to Q1/2022.

I could show that the diffuse evaporation of MAI and the variability in the amount of evaporated MAI limits the reproducibility of the MAPbI<sub>3</sub> co-evaporation process. This leads to an uncertainty in the layer thickness and stoichiometry of the deposited perovskite. A key factor determining the amount of evaporated MAI in the deposition process is the source material of MAI itself.

In XRD measurements, perovskites with MAI excess exhibit crystalline perovskite hydrates, proving water incorporation. SEM investigations further show that the water incorporation is partially reversible under the electron beam, because holes in the perovskite layer start to form, once a MAI rich perovskite is illuminated in the SEM. Even though we cannot directly measure this form of water incorporation with SEM or XRD for PbI<sub>2</sub> rich perovskites, they are still prone to aging in ambient atmosphere, with a changing photoluminescence intensity before and after air and humidity exposure.

All perovskite solar cells (PSCs) made with MAI rich perovskites are low performing with cell efficiencies of under 2%. PSCs made with PbI<sub>2</sub> rich perovskites are functioning better with cell efficiencies partially exceeding 15%, but are still affected by ambient processing and measurement. Measurements after storage in inert gas atmosphere reveal further degradation of our solar cells, like s-shape.

The two major effects that limit our cell performance and stability are degradation due to moisture incorporation and mobile ions. PbI<sub>2</sub> excess in the perovskite increases the robustness of cell performance in regards to processing and measurement under ambient conditions, likely due to the suppression of moisture incorporation into the perovskite. PbI<sub>2</sub> excess however leads to more pronounced effects of ion movement as well, leading to a large hysteresis in light-IV measurements.

By processing and encapsulation of the PSCs in an inert gas atmosphere we could achieve cell efficiencies of up to 17% in first experiments for perovskites with a small excess of  $\text{PbI}_2$ , with less than 1% absolute difference in cell efficiency for different scan directions in the light-IV measurement. This work therefore clearly demonstrates the importance of controlled environmental conditions for the production of high performing PSCs.

Optical simulations of the PSCs with  $\text{PbI}_2$  rich perovskites are possible by using an effective medium, consisting of  $\text{MAPbI}_3$  and  $\text{PbI}_2$ , to describe its varying thickness and absorption. Due to an uncertain determination of the short-circuit current of the solar cells, a quantification of the *EQE* is not possible. In this work, I presented an approach that mainly focusses on the reflection measurement of a PSC to identify the thickness and absorption of the perovskite layer.

At last, optical simulations of tandem solar cells with a perovskite top and silicon bottom solar cell demonstrate the necessity of a textured silicon surface for a high current output of the solar cells.

## 6.2 Outlook

To improve our PSC performance and reproducibility in future, there are some hurdles to overcome.

The easiest to avoid is of course degradation due to moisture, which can be prevented by processing and measurement in inert atmosphere in a glovebox. This is the standard for all groups that produce the highest efficiency PSCs and is partially already adapted at ISFH.

To reduce any influence of cross-contamination of the CTL with MAI during deposition, the CTLs should not be deposited in the same chamber as the perovskite, which is partially adapted at ISFH as well.

With the current temperature controlled MAI deposition process, we cannot achieve the same perovskite thickness and absorption in consecutive processes. Currently most work at ISFH is performed to use MAI-free perovskites [180] in hope that the deposition process is more stable. For improving the reproducibility of the perovskite deposition using MAI, the incorporation of an additional QCM or cooled metal shieldings inside the deposition chamber are the most promising approaches [39, 84].

Another important aspect is the measurement of our perovskite solar cells. Currently, we cannot perform steady state efficiency measurements or maximum



power point tracking, which are crucial for the analysis of for example stability and ionic movement in perovskites solar cells. In addition, the uncertainty regarding the measurement of  $J_{SC}$  of our solar cells is another factor complicating further analysis.

Ionic movement that causes various degradation effects is to this date the mayor issue that limits stability and efficiency of perovskite solar cells. Currently no perovskite or perovskite silicon tandem solar cell is stable and efficient enough to be commercially viable.

# Bibliography

- [1] A. Kojima, K. Teshima, Y. Shirai, and T. Miyasaka, "Organometal Halide Perovskites as Visible-Light Sensitizers for Photovoltaic Cells," *J. Am. Chem. Soc.*, vol. 131, no. 17, pp. 6050–6051, 2009.
- [2] NREL, "NREL Efficiency Chart Emerging PV." <https://www.nrel.gov/pv/assets/pdfs/cell-pv-eff-emergingpv-rev211214.pdf>, 2022. [Online; accessed 21.04.2022].
- [3] J. J. Yoo, G. Seo, M. R. Chua, *et al.*, "Efficient perovskite solar cells via improved carrier management," *Nature*, vol. 590, pp. 587–594, 2020.
- [4] K. Yamamoto, K. Yoshikawa, H. Uzu, and D. Adachi, "High-efficiency heterojunction crystalline Si solar cells," *Jpn. J. Appl. Phys.*, vol. 57, no. 8S3, 2018.
- [5] G. E. Eperon, T. Leijtens, K. A. Bush, *et al.*, "Perovskite-perovskite tandem photovoltaics with optimized band gaps," *Science*, vol. 354, no. 6314, pp. 861–865, 2016.
- [6] T. Todorov, T. Gershon, O. Gunawan, *et al.*, "Monolithic Perovskite-CIGS Tandem Solar Cells via In Situ Band Gap Engineering," *Adv. Energy Mater.*, vol. 5, no. 23, 2015.
- [7] F. Sahli, J. Werner, B. A. Kamino, *et al.*, "Fully textured monolithic perovskite/silicon tandem solar cells with 25.2% power conversion efficiency," *Nature Materials*, vol. 17, pp. 820–826, 2018.
- [8] M. Jost, L. Kegelmann, L. Korte, , and S. Albrecht, "Monolithic Perovskite Tandem Solar Cells: A Review of the Present Status and Advanced Characterization Methods Toward 30% Efficiency," *Adv. Energy Mater.*, vol. 10, no. 26, 2020.
- [9] J. Xu, C. C. Boyd, Z. J. Yu, *et al.*, "Triple-halide wide-band gap perovskites with suppressed phase segregation for efficient tandems," *Science*, vol. 367, pp. 1097–1104, 2020.

- [10] Fraunhofer ISE, "Fraunhofer ISE Photovoltaics Report." <https://www.ise.fraunhofer.de/content/dam/ise/de/documents/publications/studies/Photovoltaics-Report.pdf>, 2022. [Online; accessed 21.04.2022].
- [11] A. Al-Ashouri, E. Köhnen, B. Li, *et al.*, "Monolithic perovskite/silicon tandem solar cell with >29% efficiency by enhanced hole extraction," *Science*, vol. 370, pp. 1300–1309, 2020.
- [12] F. Haase, C. Hollemann, S. Schäfer, *et al.*, "Laser contact openings for local poly-Si-metal contacts enabling 26.1%- efficient POLO-IBC solar cells," *Solar Energy Materials and Solar Cells*, no. 186, pp. 184–193, 2018.
- [13] H.-S. Kim, J.-Y. Seo, and N.-G. Park, "Material and Device Stability in Perovskite Solar Cells," *ChemSusChem*, vol. 9, no. 18, pp. 2528–2540, 2016.
- [14] A. R. bin Mohd Yusoff, M. Vasilopoulou, D. G. Georgiadou, *et al.*, "Passivation and process engineering approaches of halide perovskite films for high efficiency and stability perovskite solar cells," *Energy and Environ. Sci.*, vol. 14, pp. 2906–2953, 2021.
- [15] C. U. Kim, E. D. Jung, and Y. W. Noh, "Strategy for large-scale monolithic Perovskite/Silicon tandem solar cell: A review of recent progress," *EcoMat*, vol. 3, no. 2, 2021.
- [16] J. Li, H. Wang, and X. Y. Chin, "Highly Efficient Thermally Co-evaporated Perovskite Solar Cells and Mini-modules," *Joule*, vol. 4, no. 5, pp. 1035–1053, 2020.
- [17] D. Li, D. Zhang, K.-S. Lim, *et al.*, "A Review on Scaling Up Perovskite Solar Cells," *Adv. Funct. Mater.*, vol. 31, no. 12, 2020.
- [18] Y. Hou, E. Aydin, M. D. Bastiani, *et al.*, "Efficient tandem solar cells with solution-processed perovskite on textured crystalline silicon," *Science*, vol. 367, no. 6482, pp. 1135–1140, 2020.
- [19] J. Li, H. A. Dewi, H. Wang, *et al.*, "Co-Evaporated MAPbI<sub>3</sub> with Graded Fermi Levels Enables Highly Performing, Scalable, and Flexible p-i-n Perovskite Solar Cells," *Adv. Funct. Mater.*, vol. 31, no. 42, 2021.
- [20] L. Gil-Escrig, M. Roß, J. Sutter, A. Al-Ashouri, C. Becker, and S. Albrecht, "Fully Vacuum-Processed Perovskite Solar Cells on Pyramidal Microstructures," *Solar RRL*, vol. 5, no. 1, 2020.

## Bibliography

- [21] E. Mosconi, P. Umari, and F. D. Angelis, "Electronic and optical properties of MAPbX<sub>3</sub> perovskites (X = I, Br, Cl): a unified DFT and GW theoretical analysis," *Phys. Chem. Chem. Phys.*, vol. 18, pp. 27158–27164, 2016.
- [22] P. Wuerfel, *Physics of Solar cells*. Weinheim, Germany: WILEY-VCH Verlag, 5 ed. , 2005.
- [23] J. H. Heo, D. S. Lee, D. H. Shina, and S. H. Im, "Recent advancement and perspective of flexible hybrid perovskitesolar cells," *Journal of Materials Chemistry A*, vol. 3, 2019.
- [24] H. D. Pham, T. C.-J. Yang, S. M. Jain, G. J. Wilson, and P. Sonar, "Development of Dopant-Free Organic Hole Transporting Materials for Perovskite Solar Cells," *Adv. Energy Mater.*, vol. 10, no. 13, 2020.
- [25] T. Lemerrier, L. Perrin, E. Planès, S. Berson, and L. Flandin, "A Comparison of the Structure and Properties of Opaque and Semi-Transparent NIP/PIN-Type Scalable Perovskite Solar Cells," *Energies*, vol. 13, no. 15, 2020.
- [26] T. Kim, J. Lim, and S. Song, "Recent Progress and Challenges of Electron Transport Layers in Organic–Inorganic Perovskite Solar Cells," *Energies*, vol. 13, no. 5572, 2020.
- [27] W. Xiang, S. F. Liu, and W. Tress, "Interfaces and Interfacial Layers in Inorganic Perovskite Solar Cells," *Angew. Chem. Int. Ed*, vol. 60, p. 26440–26453, 2021.
- [28] S. Li, Y.-L. Cao, W.-H. Li, and Z.-S. Bo, "A brief review of hole transporting materials commonly used in perovskite solar cells," *Rare Met.*, vol. 40, no. 10, pp. 2712–2729, 2021.
- [29] P.-K. Kung, M.-H. Li, P.-Y. Lin, *et al.*, "A Review of Inorganic Hole Transport Materials for Perovskite Solar Cells," *Adv. Mater. Interfaces*, vol. 5, 2018.
- [30] A. Al-Ashouri, A. Magomedov, M. Roß, *et al.*, "Conformal monolayer contacts with lossless interfaces for perovskite single junction and monolithic tandem solar cells," *Energy Environ. Sci.*, vol. 12, no. 3356, 2019.
- [31] C. Momblona, L. Gil-Escrig, E. Bandiello, *et al.*, "Efficient vacuum deposited p-i-n and n-i-p perovskite solar cells employing doped charge transport layers," *Energy Environ. Sci.*, 2016, vol. 9, no. 3456, 2016.

- [32] Z.-K. Wang and L.-S. Liao, "Doped Charge-Transporting Layers in Planar Perovskite Solar Cells," *Adv. Optical Mater.*, vol. 6, no. 1800276, 2018.
- [33] D. P. del Rey, L. Gil-Escrig, K. P. S. Zanoni, *et al.*, "Molecular Passivation of MoO<sub>3</sub>: Band Alignment and Protection of Charge Transport Layers in Vacuum-Deposited Perovskite Solar Cells," *Chem. Mater.*, vol. 31, no. 17, p. 6945–6949, 2019.
- [34] T. Golubev, D. Liu, R. Lunt, and P. Duxbury, "Understanding the impact of C60 at the interface of perovskite solar cells via drift-diffusion modeling," *AIP Advances*, vol. 9, no. 035026, 2019.
- [35] G. Sitarz, *Photoelektronenspektroskopie an Kontakt- und Absorbermaterialien fuer Perovskitesolarzellen*. Leibniz Universität Hannover. Bachelor Thesis, 2020.
- [36] S. S. Shin, S. J. Lee, and S. I. Seok, "Metal Oxide Charge Transport Layers for Efficient and Stable Perovskite Solar Cells," *Adv. Funct. Mater.*, vol. 29, no. 1900455, 2019.
- [37] S. Kavadiya, A. Onno, and C. C. Boyd, "Investigation of the Selectivity of Carrier Transport Layers in Wide-Bandgap Perovskite Solar Cells," *Sol. RRL*, vol. 5, no. 7, p. 2100107, 2021.
- [38] T. Sakurai, S. Toyoshima, and H. Kitazume, "Influence of gap states on electrical properties at interface between bathocuproine and various types of metals," *J. Appl. Phys.*, vol. 108, no. 043707, 2010.
- [39] B.-S. Kim, L. Gil-Escrig, M. Sessolo, and H. J. Bolink, "Deposition Kinetics and Compositional Control of Vacuum Processed CH<sub>3</sub>NH<sub>3</sub>PbI<sub>3</sub> Perovskite," *J. Phys. Chem. Lett.*, vol. 11, no. 16, pp. 6852–6859, 2020.
- [40] D. Liu, Q. Wang, and C. J. Traverse, "Impact of Ultrathin C60 on Perovskite Photovoltaic Devices," *ACS Nano*, vol. 12, pp. 876–883, 2018.
- [41] G.-W. Kim, D. V. Shinde, and T. Park, "Thickness of the hole transport layer in perovskite solar cells: performance versus reproducibility," *RSC Adv.*, vol. 5, no. 99356, 2015.
- [42] L. K. Ono, P. Schulz, J. J. Endres, *et al.*, "Air-Exposure-Induced Gas-Molecule Incorporation into Spiro- MeOTAD Films," *J. Phys. Chem. Lett.*, vol. 5, pp. 1374–1379, 2014.

## Bibliography

- [43] B. Hoex, J. Schmidt, P. Pohl, M. C. M. van de Sanden, and W. M. M. Kessels, "Silicon surface passivation by atomic layer deposited  $\text{Al}_2\text{O}_3$ ," *J. Appl. Phys.*, vol. 104, no. 044903, 2008.
- [44] J. Wang, W. Fu, S. Jariwala, *et al.*, "Reducing Surface Recombination Velocities at the Electrical Contacts Will Improve Perovskite Photovoltaics," *ACS Energy Lett*, vol. 4, pp. 22–227, 2019.
- [45] X. Liu, Z. Liu, and H. Ye, "Novel efficient C60-based inverted perovskite solar cells with negligible hysteresis," *Electrochimica Acta*, vol. 288, pp. 115–125, 2018.
- [46] T. S. Sherkar, C. Momblona, and L. Gil-Escrig, "Recombination in Perovskite Solar Cells: Significance of Grain Boundaries, Interface Traps, and Defect Ions," *ACS Energy Lett.*, vol. 2, pp. 1214–1222, 2017.
- [47] M. Stolterfoht, P. Caprioglio, C. M. Wolff, *et al.*, "The perovskite/transport layer interfaces dominate non-radiative recombination in efficient perovskite solar cells," *arXiv*, no. arXiv:1810.01333, 2018.
- [48] W. Tress, N. Marinova, O. Inganäs, *et al.*, "Predicting the Open-Circuit Voltage of  $\text{CH}_3\text{NH}_3\text{PbI}_3$  Perovskite Solar Cells Using Electroluminescence and Photovoltaic Quantum Efficiency Spectra: the Role of Radiative and Non-Radiative Recombination," *Adv. Energy Mater.*, vol. 5, no. 1400812, 2015.
- [49] T. Kirchartz, F. Deledalle, P. S. Tuladhar, J. R. Durrant, and J. Nelson, "On the Differences between Dark and Light Ideality Factor in Polymer:Fullerene Solar Cells," *J. Phys. Chem. Lett.*, vol. 4, pp. 2371–2376, 2013.
- [50] M. Stolterfoht, M. Grischek, P. Caprioglio, C. M. Wolff, *et al.*, "How To Quantify the Efficiency Potential of Neat Perovskite Films: Perovskite Semiconductors with an Implied Efficiency Exceeding 28%," *Adv. Mater.*, vol. 32, no. 2000080, 2020.
- [51] T. Oku, *Solar Cells - New Approaches and Reviews*, chapter: *Crystal Structures of  $\text{CH}_3\text{NH}_3\text{PbI}_3$  and Related Perovskite Compounds Used for Solar Cells*. London: IntechOpen. Edited by Leonid A. Kosyachenko.
- [52] G. Schileo and G. Grancini, "Lead or no lead? Availability, toxicity, sustainability and environmental impact of lead-free perovskite solar cells," *J. Mater. Chem.*, vol. 9, pp. 67–76, 2021.

- [53] S. Shukla, S. Shukla, L. J. Haur, *et al.*, "Effect of Formamidinium/Cesium Substitution and  $\text{PbI}_2$  on the Long-Term Stability of Triple-Cation Perovskites," *ChemSusChem*, vol. 10, pp. 3804–3809, 2017.
- [54] F. F. Targhia, Y. S. Jalili, and F. Kanjouric, "MAPbI<sub>3</sub> and FAPbI<sub>3</sub> perovskites as solar cells: Case study on structural, electrical and optical properties," *Results in Physics*, vol. 10, pp. 618–627, 2018.
- [55] C. Motta, F. El-Mellouhi, S. Kais, *et al.*, "Revealing the role of organic cations in hybrid halide perovskite  $\text{CH}_3\text{NH}_3\text{PbI}_3$ ," *NATURE COMMUNICATIONS*, vol. 6, no. 7026, 2015.
- [56] W.-J. Yin, T. Shi, and Y. Yan, "Unusual defect physics in  $\text{CH}_3\text{NH}_3\text{PbI}_3$  perovskite solar cell absorber," *Applied physics letters*, vol. 104, no. 063903, 2014.
- [57] J. Kim, S.-H. Lee, J. H. Lee, and K.-H. Hong, "The Role of Intrinsic Defects in Methylammonium Lead Iodide Perovskite," *J. Phys. Chem. Lett.*, vol. 5, pp. 1312–1317, 2014.
- [58] A. Koda, H. Okabe, M. Hiraishi, *et al.*, "Organic molecular dynamics and charge-carrier lifetime in lead iodide perovskite MAPbI<sub>3</sub>," *PNAS*, vol. 119, no. 4, 2022.
- [59] T. Zhang, C. Hu, and S. Yang\*, "Ion Migration: A "Double-Edged Sword" for Halide-Perovskite-Based Electronic Devices," *Small Methods*, vol. 4, no. 19000552, 2020.
- [60] N. Phung, A. Al-Ashouri, S. Meloni, *et al.*, "The Role of Grain Boundaries on Ionic Defect Migration in Metal Halide Perovskites," *Adv. Energy Mater.*, vol. 10, no. 1903735, 2020.
- [61] J. M. Azpiroz, E. Mosconi, J. Bisquert, and F. D. Angelis, "Defect migration in methylammonium lead iodide and its role in perovskite solar cell operation," *Energy Environ. Sci.*, vol. 8, no. 2118, 2015.
- [62] D.-H. Kang and N.-G. Park, "On the Current-Voltage Hysteresis in Perovskite Solar Cells: Dependence on Perovskite Composition and Methods to Remove Hysteresis," *Adv. Mater.*, vol. 31, no. 1805214, 2019.
- [63] Z. Li, C. Xiao, Y. Yang, *et al.*, "Extrinsic ion migration in perovskite solar cells," *Energy Environ. Sci.*, vol. 10, no. 1234, 2017.

## Bibliography

- [64] D. A. Jacobs, Y. Wu, H. Shen, *et al.*, "Hysteresis phenomena in perovskite solar cells: the many and varied effects of ionic accumulation," *Phys. Chem. Chem. Phys.*, vol. 19, pp. 3094–3103, 2017.
- [65] M. Engl, *Quanteneffizienzmessung von Perowskit-Solarzellen*. Leibniz Universität Hannover. Master Thesis, 2021.
- [66] W. Tress, "Metal Halide Perovskites as Mixed Electronic-Ionic Conductors: Challenges and Opportunities-From Hysteresis to Memristivity," *J. Phys. Chem. Lett.*, vol. 8, pp. 3106–3114, 2017.
- [67] Q. Wang, B. Chen, Y. Liu, *et al.*, "Scaling behavior of moisture-induced grain degradation in polycrystalline hybrid perovskite thin films," *Energy Environ. Sci.*, vol. 10, no. 516, 2016.
- [68] N. Aristidou, C. Eames, I. Sanchez-Molina, *et al.*, "Fast oxygen diffusion and iodide defects mediate oxygen-induced degradation of perovskite solar cells," *Nature Communications*, vol. 8, no. 15218, 2017.
- [69] H.-S. Kim, J.-Y. Seo, and N.-G. Park, "Material and Device Stability in Perovskite Solar Cells," *ChemSusChem*, vol. 9, pp. 2528–2540, 2016.
- [70] G. E. Eperon, S. N. Habisreutinger, T. Leijtens, *et al.*, "The Importance of Moisture in Hybrid Lead Halide Perovskite Thin Film Fabrication," *ACS Nano*, vol. 9, no. 9, pp. 9380–9393, 2015.
- [71] G. Wang, C. Liu, W. Kong, *et al.*, "Liberating Researchers from the Glove-box: A Universal Thermal Radiation Protocol Toward Efficient Fully Air-Processed Perovskite Solar Cells," *Sol. RRL*, vol. 3, no. 1800324, 2019.
- [72] N. Y. Nia, M. Zendehtdel, L. Cin'á, c F. Matteoccia, and A. D. Carlo, "A crystal engineering approach for scalable perovskite solar cells and module fabrication: a full out of glove box procedure," *J. Mater. Chem. A*, vol. 6, no. 659, 2018.
- [73] Y. Zhang, H. Lv, C. Cui, *et al.*, "Enhanced Optoelectronic Quality of Perovskite Films with Excess CH<sub>3</sub>NH<sub>3</sub>I for High-efficient Solar Cells in Ambient Air," *Nanotechnology*, vol. 28, no. 205401, 2017.
- [74] P. P. Khlyabich and Y.-L. Loo, "Crystalline Intermediates and Their Transformation Kinetics during the Formation of Methylammonium Lead Halide Perovskite Thin Films," *Chem. Mater.*, vol. 28, pp. 9041–9048, 2016.



- [75] C. Roldán-Carmona, P. Gratia, I. Zimmermann, *et al.*, “High efficiency methylammonium lead triiodide perovskite solar cells: the relevance of non-stoichiometric precursors,” *Energy Environ. Sci.*, vol. 8, pp. 3550–3556, 2015.
- [76] B. Roose, K. Dey, Y.-H. Chiang, *et al.*, “Critical Assessment of the Use of Excess Lead Iodide in Lead Halide Perovskite Solar Cells,” *J. Phys. Chem. Lett.*, vol. 11, pp. 6505–6512, 2020.
- [77] T. J. Jacobsson, J.-P. Correa-Baena, E. H. Anaraki, *et al.*, “Unreacted PbI<sub>2</sub> as a Double-Edged Sword for Enhancing the Performance of Perovskite Solar Cells,” *J. Am. Chem. Soc.*, vol. 138, pp. 10331–10343, 2016.
- [78] J. an Yang, A. Xiao, L. Xie, *et al.*, “Precise control of PbI<sub>2</sub> excess into grain boundary for efficacious charge extraction in off-stoichiometric perovskite solar cells,” *Electrochimica Acta*, vol. 338, no. 135697, 2020.
- [79] Q. Chen, H. Zhou, T.-B. Song, *et al.*, “Controllable self-induced passivation of hybrid lead iodide perovskites toward high performance solar cells,” *Nano Lett.*, vol. 14, no. 7, p. 4158–4163, 2014.
- [80] O. Eklund, *Introduction to Perovskite Solar Cells in an Undergraduate Laboratory Exercise*. 651 88 Karlstad, Sweden: Karlstads Universitet. Bachelor Thesis, 2021.
- [81] P. Cui, P. Fu, D. Wei, *et al.*, “Reduced surface defects of organometallic perovskite by thermal annealing for highly efficient perovskite solar cells,” *RSC Adv.*, vol. 5, no. 75622, 2015.
- [82] C. Bi, Y. Shao, Y. Yuan, *et al.*, “Understanding the formation and evolution of interdiffusion grown organolead halide perovskite thin films by thermal annealing,” *J. Mater. Chem. A*, vol. 2, no. 18508, 2014.
- [83] L. Gil-Escrig, M. Roß, J. Sutter, *et al.*, “Fully Vacuum-Processed Perovskite Solar Cells on Pyramidal Microtextures,” *Sol. RRL*, vol. 5, no. 2000553, 2021.
- [84] M. Roß, L. Gil-Escrig, A. Al-Ashouri, *et al.*, “Co-Evaporated p-i-n Perovskite Solar Cells Beyond 20% Efficiency: Impact of Substrate Temperature and Hole-Transport Layer,” *ACS Appl. Mater. Interfaces*, vol. 12, no. 35, p. 39261–39272, 2020.

## Bibliography

- [85] M. Roß, S. Severin, M. B. Stutz, *et al.*, “Co-Evaporated Formamidinium Lead Iodide Based Perovskites with 1000 h Constant Stability for Fully Textured Monolithic Perovskite/Silicon Tandem Solar Cells,” *Adv. Energy Mater.*, vol. 11, no. 2101460, 2021.
- [86] Y. Vaynzof, “The Future of Perovskite Photovoltaics-Thermal Evaporation or Solution Processing?,” *Adv. Energy Mater.*, vol. 10, no. 2003073, 2020.
- [87] M. M. Tavakoli, P. Yadav, D. Prochowicz, and R. Tavakoli, “Efficient, Hysteresis-Free, and Flexible Inverted Perovskite Solar Cells Using All-Vacuum Processing,” *Sol. RRL*, vol. 5, no. 2000552, 2021.
- [88] J. Borchert, I. Levchuk, L. C. Snoek, *et al.*, “Impurity Tracking Enables Enhanced Control and Reproducibility of Hybrid Perovskite Vapor Deposition,” *ACS Appl. Mater. Interfaces*, vol. 11, pp. 28851–28857, 2019.
- [89] D. Zhao, W. Ke, C. R. Grice, *et al.*, “Annealing-free efficient vacuum-deposited planar perovskite solar cells with evaporated fullerenes as electron-selective layers,” *Nano Energy*, vol. 19, pp. 88–97, 2016.
- [90] T. Abzieher, J. A. Schwenzler, S. Moghadamzadeh, *et al.*, “Efficient All-Evaporated pin-Perovskite Solar Cells: A Promising Approach Toward Industrial Large-Scale Fabrication,” *IEEE Journal of Photovoltaics*, vol. 9, no. 5, pp. 1249–1257, 2019.
- [91] T. Abzieher, T. Feeney, F. Schackmar, *et al.*, “From Groundwork to Efficient Solar Cells: On the Importance of the Substrate Material in Co-Evaporated Perovskite Solar Cells,” *Adv. Funct. Mat.*, vol. 31, no. 42, p. 2104482, 2021.
- [92] J. Li, H. Wang, X. Y. Chin, *et al.*, “Highly Efficient Thermally Co-evaporated Perovskite Solar Cells and Mini-modules,” *Joule*, vol. 4, pp. 1035–1053, 2020.
- [93] J. Li, H. A. Dewi, H. Wang, *et al.*, “Co-Evaporated MAPbI<sub>3</sub> with Graded Fermi Levels Enables Highly Performing, Scalable, and Flexible p-i-n Perovskite Solar Cells,” *Adv. Funct. Mater.*, vol. 31, no. 42, p. 2103252, 2021.
- [94] K. B. Lohmann, J. B. Patel, M. U. Rothmann, *et al.*, “Control over Crystal Size in Vapor Deposited Metal-Halide Perovskite Films,” *ACS Energy Lett.*, vol. 5, pp. 710–717, 2020.

- [95] I. C. Kaya, K. P. S. Zanoni, F. Palazon, *et al.*, "Crystal Reorientation and Amorphization Induced by Stressing Efficient and Stable P–I–N Vacuum-Processed MAPbI<sub>3</sub> Perovskite Solar Cells," *Adv. Energy Sustainability Res.*, vol. 2, no. 2000065, 2021.
- [96] K. L. Heinze, O. Dolynchuk, T. Burwig, *et al.*, "Importance of methylammonium iodide partial pressure and evaporation onset for the growth of co-evaporated methylammonium lead iodide absorbers," *Scientific Reports*, vol. 11, no. 15299, 2021.
- [97] N. Mielich, *Einfluss der Metallisierung auf Effizienz und Stabilität von Perowskit-Solarzellen*. Leibniz Universität Hannover. Bachelor Thesis, 2021.
- [98] PV Education, "Finger Resistance." <https://www.pveducation.org/pvcdrom/design-of-silicon-cells/finger-resistance>, 2022. [Online; accessed 03.05.2022].
- [99] PV Education, "Emitter Resistance." <https://www.pveducation.org/pvcdrom/design-of-silicon-cells/emitter-resistance>, 2022. [Online; accessed 03.05.2022].
- [100] M. Müller, G. Fischer, B. Bitnar, *et al.*, "Loss analysis of 22% efficient industrial PERC solar cells," *Energy Procedia*, vol. 124, pp. 131–137, 2017.
- [101] Y. Cheng, Y. Peng, A. K.-Y. Jen, and H.-L. Yip, "Development and Challenges of Metal Halide Perovskite Solar Modules," *Sol. RRL*, vol. 6, no. 2100545, 2021.
- [102] L. M. Perez, "Oxford PV: Addressing climate change with the rapid development of perovskite/silicon tandem photovoltaics." HOPV21 Conference Talk, 2021.
- [103] C. Messmer, B. S. Goraya, S. Nold, *et al.*, "The race for the best silicon bottom cell: Efficiency and cost evaluation of perovskite–silicon tandem solar cells," *Prog Photovolt Res Appl.*, vol. 29, pp. 744–759, 2021.
- [104] A. Uddin, M. B. Upama, H. Yi, and L. Duan, "Encapsulation of Organic and Perovskite Solar Cells: A Review," *Coatings*, vol. 9, no. 65, 2019.
- [105] K. Prashanthan, B. Naydenov, K. Lips, *et al.*, "Interdependence of photon upconversion performance and antisolvent processing in thin-film halide perovskite-sensitized triplet–triplet annihilators," *J. Chem. Phys.*, vol. 153, no. 164711, 2020.

## Bibliography

- [106] S. J. Wolter, V. Steckenreiter, M. C. Tatarzyn, *et al.*, "Determination and influence evaluation of the acoustic impedance ratio for thermal coevaporation," *Appl. Phys. Lett.*, vol. 113, no. 013301, 2018.
- [107] R. Niepelt, S. J. Wolter, M. Tatarzyn, *et al.*, "Application of Experimentally Determined Acoustic Impedance Ratio for Homogeneous Co-Evaporation of Perovskite Absorbers," *IEEE 34th EU PVSEC*, 2018.
- [108] F. Palazon, D. P. del Rey, B. Dänekamp, *et al.*, "Room-Temperature Cubic Phase Crystallization and High Stability of Vacuum-Deposited Methylammonium Lead Triiodide Thin Films for High-Efficiency Solar Cells," *Adv. Mater.*, vol. 31, no. 1902692, 2019.
- [109] D. P. del Rey, P. P. Boix, M. Sessolo, A. Hadipour, and H. J. Bolink, "Interfacial Modification for High-Efficiency Vapor-Phase-Deposited Perovskite Solar Cells Based on a Metal Oxide Buffer Layer," *J. Phys. Chem. Lett.*, vol. 9, no. 5, pp. 1041–1046, 2018.
- [110] T. Gallet, R. G. Poeira, E. M. Lanzoni, *et al.*, "Co-evaporation of  $\text{CH}_3\text{NH}_3\text{PbI}_3$ : How Growth Conditions Impact Phase Purity, Photostriction, and Intrinsic Stability," *ACS Appl. Mater. Interfaces*, vol. 13, pp. 2642–2653, 2021.
- [111] T. Gotanda, H. Oooka, S. Mori, *et al.*, "Facile and scalable fabrication of low-hysteresis perovskite solar cells and modules using a three-step process for the perovskite layer," *Journal of Power Sources*, vol. 430, pp. 145–149, 2019.
- [112] Z. Zhou, Z. Wang, Y. Zhou, *et al.*, "Methylamine-Gas-Induced Defect-Healing Behavior of  $\text{CH}_3\text{NH}_3\text{PbI}_3$  Thin Films for Perovskite Solar Cells," *Angew. Chemie*, vol. 127, pp. 9841–9845, 2015.
- [113] R. W. G. Wyckoff, *Crystal Structures, Band 1*. Wiley. page 239-244.
- [114] J. B. Patel, R. L. Milot, A. D. Wright, *et al.*, "Formation Dynamics of  $\text{CH}_3\text{NH}_3\text{PbI}_3$  Perovskite Following Two-Step Layer Deposition," *J. Phys. Chem. Lett.*, vol. 7, pp. 96–102, 2016.
- [115] X. Ren, Z. Yang, D. Yang, *et al.*, "Modulating crystal grain size and optoelectronic properties of perovskite films for solar cells by reaction temperature," *Nanoscale*, vol. 8, no. 3816, 2016.

- [116] L. A. Muscarella, E. M. Hutter, S. Sanchez, *et al.*, “Crystal Orientation and Grain Size: Do They Determine Optoelectronic Properties of MAPbI<sub>3</sub> Perovskite?,” *J. Phys. Chem. Lett.*, vol. 10, pp. 6010–6018, 2019.
- [117] M. Richter, *Strom- und Spannungsverhalten von Perowskit-Solarzellen beim Anlegen von Spannung in Rückwärtsrichtung*. Leibniz Universität Hannover. Master Thesis, 2021.
- [118] S. Kim, J. H. Jang, Z. Wu, *et al.*, “Interfacial Defects Change the Correlation between Photoluminescence, Ideality Factor, and Open-Circuit Voltage in Perovskite Solar Cells,” *Small*, vol. 17, no. 2101839, 2021.
- [119] N. Evert, *Zeitaufgelöste Photolumineszenzspektroskopie an Bleihalogenperovskiten für Solarzellen*. Leibniz Universität Hannover. Master Thesis, 2020.
- [120] Q. Wang, X. Wang, Z. Yang, *et al.*, “Efficient sky-blue perovskite light-emitting diodes via photoluminescence enhancement,” *Nature Communications*, vol. 10, no. 5633, 2019.
- [121] S. Jiang, Y. Fang, R. Li, *et al.*, “Pressure-Dependent Polymorphism and Band-Gap Tuning of Methylammonium Lead Iodide Perovskite,” *Angew. Chem. Int. Ed.*, vol. 55, pp. 6540–6544, 2016.
- [122] A. Zohar, I. Levine, S. Gupta, *et al.*, “What Is the Mechanism of MAPbI<sub>3</sub> p-Doping by I<sub>2</sub>? Insights from Optoelectronic Properties,” *ACS Energy Lett.*, vol. 2, pp. 2408–2414, 2017.
- [123] E. Meyer, “Extraction of Saturation Current and Ideality Factor from Measuring  $V_{OC}$  and  $I_{SC}$  of Photovoltaic Modules,” *International Journal of Photoenergy*, vol. 2017, no. 8479487, 2017.
- [124] C. N. Kruse, K. Bothe, and R. Brendel, “Comparison of Free Energy Loss Analysis and Synergistic Efficiency Gain Analysis for PERC Solar Cells,” *IEEE JOURNAL OF PHOTOVOLTAICS*, vol. 8, pp. 683–688, 2018.
- [125] D. Shen, X. Yu, X. Cai, *et al.*, “Understanding the solvent-assisted crystallization mechanism inherent in efficient organic–inorganic halide perovskite solar cells,” *J. Mater. Chem. A*, vol. 2, no. 20454, 2014.
- [126] E. H. Anaraki, A. Kermanpur, L. Steier, *et al.*, “Highly efficient and stable planar perovskite solar cells by solution-processed tin oxide,” *Energy Environ. Sci.*, vol. 9, no. 3128, 2016.

## Bibliography

- [127] J. Shi, Y. Li, Y. Li, *et al.*, “From Ultrafast to Ultraslow: Charge-Carrier Dynamics of Perovskite Solar Cells,” *Joule*, vol. 2, pp. 879–901, 2018.
- [128] H. Wang, A. Guerrero, A. Bou, *et al.*, “Kinetic and material properties of interfaces governing slow response and long timescale phenomena in perovskite solar cells,” *Energy Environ. Sci.*, vol. 12, pp. 2054–2079, 2019.
- [129] P. Lopez-Varo, J. A. Jimenez-Tejada, M. García-Rosell, *et al.*, “Device Physics of Hybrid Perovskite Solar cells: Theory and Experiment,” *Adv. Energy Mater.*, vol. 8, no. 1702772, 2018.
- [130] J. A. Christians, J. S. Manser, and P. V. Kamat, “Best Practices in Perovskite Solar Cell Efficiency Measurements. Avoiding the Error of Making Bad Cells Look Good,” *J. Phys. Chem. Lett.*, vol. 6, pp. 852–857, 2015.
- [131] Y. Wang, X. Liu, Z. Zhou, *et al.*, “Reliable Measurement of Perovskite Solar Cells,” *Adv. Mater.*, vol. 31, no. 1803231, 2019.
- [132] V. M. L. Corre, J. Diekmann, F. Pena-Camargo, *et al.*, “Best Practices in Perovskite Solar Cell Efficiency Measurements. Avoiding the Error of Making Bad Cells Look Good,” *Sol. RRL*, vol. 6, no. 2100772, 2022.
- [133] F. Wu, B. Bahrami, K. Chen, *et al.*, “Bias-Dependent Normal and Inverted J-V Hysteresis in Perovskite Solar Cells,” *ACS Appl. Mater. Interfaces*, vol. 10, pp. 25604–25613, 2018.
- [134] E. Zimmermann, K. K. Wong, M. Müller, *et al.*, “Characterization of perovskite solar cells: Towards a reliable measurement protocol,” *APL Mater.*, vol. 4, no. 091901, 2016.
- [135] S.-E. Chiang, J.-R. Wu, H.-M. Cheng, *et al.*, “Origins of the s-shape characteristic in J-V curve of inverted-type perovskite solar cells,” *Nanotechnology*, vol. 31, no. 115403, 2020.
- [136] A. Guerrero, J. You, C. Aranda, *et al.*, “Interfacial Degradation of Planar Lead Halide Perovskite Solar Cells,” *ACS Nano*, vol. 10, pp. 218–224, 2016.
- [137] Y. Cheng and L. Ding, “Pushing commercialization of perovskite solar cells by improving their intrinsic stability,” *Energy Environ. Sci.*, vol. 14, pp. 3233–3255, 2021.

- [138] F. Haque, N. T. T. Hoang, J. Ji, and M. Mativenga, "Effect of Precursor Composition on Ion Migration in Hybrid Perovskite  $\text{CH}_3\text{NH}_3\text{PbI}_3$ ," *IEEE ELECTRON DEVICE LETTERS*, vol. 40, pp. 1756–1759, 2019.
- [139] J.-W. Lee, S.-G. Kim, J.-M. Yang, *et al.*, "Verification and mitigation of ion migration in perovskite solar cells," *APL Mater.*, vol. 7, no. 041111, 2019.
- [140] H. A. Dewi, J. Li, H. Wang, *et al.*, "Excellent Intrinsic Long-Term Thermal Stability of Co-Evaporated  $\text{MAPbI}_3$  Solar Cells at  $85^\circ\text{C}$ ," *Adv. Funct. Mater.*, vol. 31, no. 2100557, 2021.
- [141] S. N. Habisreutinger, N. K. Noel, H. J. Snaith, *et al.*, "Hysteresis Index: A Figure without Merit for Quantifying Hysteresis in Perovskite Solar Cells," *ACS Energy Lett.*, vol. 3, pp. 2472–2476, 2018.
- [142] J. Herterich, M. Unmüssig, G. Loukeris, *et al.*, "Ion Movement Explains Huge  $V_{\text{OC}}$  Increase despite Almost Unchanged Internal Quasi-Fermi-Level Splitting in Planar Perovskite Solar Cells," *Energy Technol.*, vol. 9, no. 2001104, 2021.
- [143] C. Dreessen, D. P. del Rey, P. P. Boix, and H. J. Bolink, "Radiative and non-Radiative Losses Analysis by In-situ Photoluminescence in Perovskite Solar Cell Current-Voltage Curves," *Journal of Luminescence*, vol. 222, no. 117106, 2020.
- [144] T. Kirchartz, L. Krückemeier, and E. L. Unger, "Research Update: Recombination and open-circuit voltage in lead-halide perovskites," *APL Mater.*, vol. 6, no. 100702, 2018.
- [145] M. Stolterfoht, P. Caprioglio, C. M. Wolff, *et al.*, "The impact of energy alignment and interfacial recombination on the internal and external open-circuit voltage of perovskite solar cells," *Energy Environ. Sci.*, vol. 12, no. 2778, 2019.
- [146] H. Xua, Y. Wua, J. Cui, *et al.*, "Formation and evolution of the unexpected  $\text{PbI}_2$  phase at interface during the growth of evaporated perovskite films," *Phys. Chem. Chem. Phys.*, vol. 18, pp. 18607–18613, 2016.
- [147] T. Du, W. Xu, M. Daboczi, *et al.*, "p-doping of organic hole transport layers in p-i-n perovskite solar cells: correlating open-circuit voltage and photoluminescence quenching," *J. Mater. Chem. A*, vol. 7, pp. 18971–18979, 2019.

## Bibliography

- [148] J. Hong, H. Kim, and I. Hwang, "Aging-induced light-soaking effects and open-circuit voltage hysteretic behavior of inverted perovskite solar cells incorporating a hole transport metal halide layer via morphology-dependent inflow of iodide ions," *J. Mater. Chem. C*, vol. 7, no. 1173, 2019.
- [149] R. Brendel, "Sunrays: a versatile ray tracing program for the photovoltaic community," *Proceedings of the 12th European Photovoltaic Solar Energy Conference*, pp. 1339–1342, 1994.
- [150] A. Nakane, H. Tampo, M. Tamakoshi, *et al.*, "Quantitative determination of optical and recombination losses in thin-film photovoltaic devices based on external quantum efficiency analysis," *J. Appl. Phys.*, vol. 120, no. 064505, 2016.
- [151] P. P. Altermatt, G. Heiser, A. G. Aberle, *et al.*, "Spatially resolved analysis and minimization of resistive losses in high-efficiency Si solar cells," *Progress in Photovoltaics: Research and Applications*, vol. 4, no. 6, pp. 399–414, 1996.
- [152] P. Tockhorn, J. Sutter, R. Colom, *et al.*, "Improved Quantum Efficiency by Advanced Light Management in Nanotextured Solution-Processed Perovskite Solar Cells," *ACS Photonics*, vol. 7, pp. 2589–2600, 2020.
- [153] J. A. Raiford, R. A. Belisle, K. A. Bush, *et al.*, "Atomic layer deposition of vanadium oxide to reduce parasitic absorption and improve stability in n-i-p perovskite solar cells for tandems," *Sustainable Energy Fuels*, vol. 3, no. 1517, 2019.
- [154] Z. Liu, C. Kwong, C. Cheunga, *et al.*, "The characterization of the optical functions of BCP and CBP thin films by spectroscopic ellipsometry," *Synthetic Metals*, vol. 59, pp. 159–163, 2005.
- [155] S. L. Ren, Y. Wang, A. M. Rao, *et al.*, "Ellipsometric determination of the optical constants of C60 (Buckminsterfullerene) films," *Appl. Phys. Lett.*, vol. 59, no. 2678, 1991.
- [156] E. D. Palik, *Handbook of Optical Constants of Solids*. Elsevier, volume 2 ed.
- [157] H. Peelaers, E. Kioupakis, and C. G. V. de Walle, "Fundamental limits on optical transparency of transparent conducting oxides: Free-carrier absorption in SnO<sub>2</sub>," *Appl. Phys. Lett.*, vol. 100, no. 01191, 2012.



- [158] H. Fujiwara and R. W. Collins, *Spectroscopic Ellipsometry for Photovoltaics*. Springer Series in Optical Sciences, volume 2 ed.
- [159] P. Löper, M. Stuckelberger, B. Niesen, *et al.*, “Complex Refractive Index Spectra of  $\text{CH}_3\text{NH}_3\text{PbI}_3$  Perovskite Thin Films Determined by Spectroscopic Ellipsometry and Spectrophotometry,” *J. Phys. Chem. Lett.*, vol. 6, pp. 66–71, 2015.
- [160] J. A. Guerra, A. Tejada, L. Korte, *et al.*, “Determination of the complex refractive index and optical bandgap of  $\text{CH}_3\text{NH}_3\text{PbI}_3$  thin films,” *J. Appl. Phys.*, vol. 121, no. 173104, 2017.
- [161] J.-S. Park, S. Choi, Y. Yan, *et al.*, “Electronic Structure and Optical Properties of  $\alpha$ - $\text{CH}_3\text{NH}_3\text{PbBr}_3$  Perovskite Single Crystal,” *J. Phys. Chem. Lett.*, vol. 6, pp. 4304–4308, 2015.
- [162] Q. Dong, Y. Fang, Y. Shao, *et al.*, “Electron-hole diffusion lengths above  $175\ \mu\text{m}$  in solution-grown  $\text{CH}_3\text{NH}_3\text{PbI}_3$  single crystals,” *Science*, vol. 347, pp. 967–970, 2015.
- [163] S. Ravishankar, C. Aranda, P. P. Boix, *et al.*, “Effects of Frequency Dependence of the External Quantum Efficiency of Perovskite Solar Cells,” *J. Phys. Chem. Lett.*, vol. 9, pp. 3099–3104, 2018.
- [164] D. Winter, *Untersuchung der Schichtstruktur von Perowskitabsorbern anhand von Quanteneffizienzanalysen*. Leibniz Universität Hannover. Master Thesis, 2021.
- [165] J. Oh, H.-C. Yuan, and H. M. Branz, “An 18.2%-efficient black-silicon solar cell achieved through control of carrier recombination in nanostructures,” *Nature Nanotechnology*, vol. 7, pp. 743–748, 2012.
- [166] T. Hara, T. Maekawa, S. Minoura, *et al.*, “Quantitative Assessment of Optical Gain and Loss in Submicron-Textured  $\text{CuIn}_{1-x}\text{Ga}_x\text{Se}_2$  Solar Cells Fabricated by Three-Stage Coevaporation,” *Phys. Rev. Appl.*, vol. 2, no. 034012, 2014.
- [167] A. Nakane, H. Tampo, M. Tamakoshi, *et al.*, “Quantitative determination of optical and recombination losses in thin-film photovoltaic devices based on external quantum efficiency analysis,” *J. Appl. Phys.*, vol. 120, no. 064505, 2016.

## Bibliography

- [168] A. Tejada, S. Braunger, L. Korte, *et al.*, "Optical characterization and bandgap engineering of flat and wrinkle-textured  $\text{FA}_{0.83}\text{Cs}_{0.17}\text{Pb}(\text{I}_{1-x}\text{Br}_x)_3$  perovskite thin films," *J. Appl. Phys.*, vol. 123, no. 175302, 2018.
- [169] S. Mariotti, K. Jäger, M. Diederich, *et al.*, "Monolithic Perovskite/Silicon Tandem Solar Cells Fabricated Using Industrial p-Type Polycrystalline Silicon on Oxide/Passivated Emitter and Rear Cell Silicon Bottom Cell Technology," *Sol. RRL*, vol. 6, no. 2101066, 2022.
- [170] R. Peibst, M. Rienäcker, B. Min, *et al.*, "From PERC to Tandem: POLO- and  $\text{p}^+/\text{n}^+$  Poly-Si Tunneling Junction as Interface Between Bottom and Top Cell," *IEEE Journal of Photovoltaics*, vol. 9, no. 1, pp. 49–54, 2019.
- [171] T. Dullweber, C. Kranz, R. Peibst, *et al.*, "PERC+: industrial PERC solar cells with rear Al grid enabling bifaciality and reduced Al paste consumption," *Progress in Photovoltaics: Research and Applications*, vol. 24, no. 12, pp. 1487–1498, 2015.
- [172] H. Shen, D. Walter, Y. Wu, *et al.*, "Monolithic Perovskite/Si Tandem Solar Cells: Pathways to Over 30% Efficiency," *Adv. Energy Mater.*, vol. 10, no. 1902840, 2020.
- [173] W. Tao and Y. Du, "The optical properties of solar cells before and after encapsulation," *Solar Energy*, vol. 122, pp. 718–726, 2015.
- [174] J. Warby, F. Zu, S. Zeiske, *et al.*, "Understanding Performance Limiting Interfacial Recombination in pin Perovskite Solar Cells," *Adv. Energy Mater.*, vol. 12, no. 2103567, 2022.
- [175] J. P. Mailoa, C. D. Bailie, E. C. Johlin, *et al.*, "A 2-terminal perovskite/silicon multijunction solar cell enabled by a silicon tunnel junction," *Appl. Phys. Lett.*, vol. 106, no. 121105, 2015.
- [176] Y. Li, B. Shi, Q. Xu, *et al.*, "Wide Bandgap Interface Layer Induced Stabilized Perovskite/Silicon Tandem Solar Cells with Stability over Ten Thousand Hours," *Adv. Energy Mater.*, vol. 11, no. 2102046, 2021.
- [177] C. Shou, J. Zheng, Q. Han, *et al.*, "Optimization of Tunnel-Junction for Perovskite/Tunnel Oxide Passivated Contact (TOPCon) Tandem Solar Cells," *Phys. Status Solidi A*, vol. 218, no. 2100562, 2021.
- [178] D. K. Schroeder, R. N. Thomas, and J. C. Swartz, "Free Carrier Absorption in Silicon," *IEEE Journal of Solid-State Circuits*, vol. SC-13, pp. 180–187, 2021.

- [179] E. L. Warren, W. E. McMahon, M. Rienecker, *et al.*, “A Taxonomy for Three-Terminal Tandem Solar Cells,” *ACS Energy Lett.*, vol. 5, pp. 1233–1242, 2020.
- [180] Y.-H. Chiang, M. Anaya, , S. D. Stranks, *et al.*, “Multisource Vacuum Deposition of Methylammonium-Free Perovskite Solar Cells,” *ACS Energy Lett.*, vol. 5, pp. 2498–2504, 2020.



## List of Publications

Parts of this thesis have previously been presented in the following conferences:

M. Diederich, S. Kajari-Schröder, S. Wolter, et. al, "Modelling Perovskites with Reduced Absorption from Reflection Measurements of Perovskite Solar Cells", *Proceedings of 13th Conference on Hybrid and Organic Photovoltaics (HOPV21)*, no. 137, 2021.

Other publications:

S. Wolter, V. Steckenreiter, M. Tatarzyn, et al., "Dual-Source Co-Evaporation of Perovskite Absorbers and Determination of the Acoustic Impedance Ratio of the Deposited Single Precursors", *MRS Fall Meeting*, 2017.

R. Niepelt, S. Wolter, M. Tatarzyn, et. al, "Application of Experimentally Determined Acoustic Impedance Ratio for Homogeneous Co-Evaporation of Perovskite Absorbers", *2018 IEEE 7th World Conference on Photovoltaic Energy Conversion (WCPEC) (A Joint Conference of 45th IEEE PVSC, 28th PVSEC & 34th EU PVSEC)*, pp. 508-511, 2018.

S. Mariotti, K. Jäger, M. Diederich, et al., "Monolithic Perovskite/Silicon Tandem Solar Cells Fabricated Using Industrial p-Type Polycrystalline Silicon on Oxide/Passivated Emitter and Rear Cell Silicon Bottom Cell Technology", *Sol. RRL*, vol. 6, no. 2101066, 2022.

## Appendix - sheet resistance in TCO

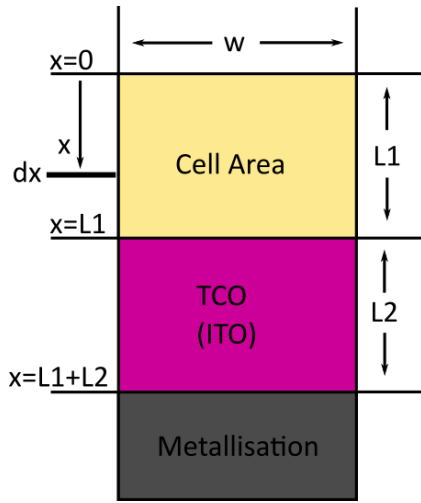


Figure 6.1: Pathway of charge carriers along L1 and L2 in the cell area and TCO of a PSC.

In the following, I will briefly explain the derivation for Equation 2.1, which calculates the series resistance contribution of the sheet resistance in the TCO in a typical PSC. It is mostly analogous to [98, 99], which calculates the series resistance for a finger or emitter in a solar cell.

The according cell geometry is depicted in Figure 6.1.

We can calculate the current  $I_{cell,L1}$  in the cell area in increment  $dx$  for  $0 \leq x \leq L1$ , with cell length  $L1$ ,  $J_{mpp}$  = generated current density at the solar cells  $mpp$ ,  $w$  = cell width:

$$I_{cell,L1} = x \cdot J_{mpp} \cdot w$$

The current in the TCO  $I_{cell,L2}$  for  $L1 \leq x \leq L2 + L1$  is constant:

$$I_{cell,L2} = L1 \cdot J_{mpp} \cdot w$$

The power loss through sheet resistance in the TCO (ITO) in element  $dx$  (along  $L1$  and  $L2$ ) is then  $P_{loss} = I_{cell}^2 \cdot R$

with  $R = (R_{ITO}/w) \cdot dx$ , with sheet resistance of ITO  $R_{ITO}$

For the total power loss we have to integrate  $P_{loss}$  over  $x$  from 0 to  $L1 + L2$  with  $I_{cell,L1}$  for  $0 \leq x \leq L1$  and  $I_{cell,L2}$  for  $L1 \leq x \leq L2 + L1$ .

For  $0 \leq x \leq L1$  (cell area):

$$\int_0^{L1} (x \cdot J_{mpp} \cdot w)^2 \cdot (R_{ITO}/w) \cdot dx = 1/3 \cdot L1^3 \cdot J_{mpp}^2 \cdot R_{ITO} \cdot w$$

For the TCO area this results in:  $L2 \cdot L1^2 \cdot J_{mpp}^2 \cdot R_{ITO} \cdot w$

The total power loss in  $L1$  and  $L2$  is then  $P_{loss} = (L1/3 + L2) \cdot L1^2 \cdot J_{mpp}^2 \cdot R_{ITO} \cdot w$

Total generated power in solar cell area:  $P_{SC} = V_{mpp} \cdot J_{mpp} \cdot L1 \cdot w$

Fraction of lost power:  $P_{loss}/P_{SC} = (L1/3 + L2) \cdot L1 \cdot (J_{mpp}/V_{mpp}) \cdot R_{ITO}$

To get series resistance contribution of ITO  $R_{S,ITO}$  we multiply with the cell resistance  $V_{mpp}/J_{mpp}$  which leads to:

$$R_{S,ITO} = (L1/3 + L2) \cdot L1 \cdot R_{ITO} \text{ (Equation in chapter 2.2.5)}$$

Since  $L1$ ,  $L2$  and  $R_{ITO}$  are trivial to measure, this allows a fast estimation of the series contribution of ITO. For ITO width  $\neq$  cell width multiply with the factor ITO width/cell width accordingly.

## Acknowledgments

At last, i want to thank all the people that contributed to this work:

- Prof. Dr. Hans-Jörg Osten for his willingness to replace Tobias Wietler as official supervisor and examination of this Ph.D. thesis.
- Prof. Dr. Robby Peibst and Prof. Dr. Jan Schmidt for performing the additional examination.
- Prof. Dr. Bernhard Wicht for taking over the chair of the doctoral committee.
- Prof. Dr. Tobias Wietler for the actual supervision of this work and his helpful guidance throughout my dissertation.
- Prof. Dr. Rolf Brendel for updating his optical simulation software SunRays during his holidays and providing support and guidance with optical simulations. Without his efforts, no optical simulations of tandem solar cells would be possible at ISFH currently.
- Dr. Sarah Kajari-Schröder and the original perovskite team with Dr. Raphael Niepelt, Dr. Sascha Wolter, Dr. Michael Rienäcker, Verena Steckenreiter and especially Marta Löhning and Heike Kohlenberg for the open welcome at ISFH and for teaching me all the groundwork needed for processing solar cells.
- The fellow PhD candidates Verena Barnscheidt and Lukas Brockmann for our often successful attempts to at least identify and sometimes even solve a problem as well as fruitful discussions about various topics for a better understanding of our solar cells.
- Dennis Winter, who I supervised during his master thesis at ISFH who initially had the idea to use  $\text{PbI}_2$  as material in a prototype of the effective medium model to simulate varying absorption in the perovskite.
- Yevgeniya Larionova for her committed efforts to identify issues with the metallisation of our solar cells.
- Mircea Turcu and Jessica Strey for processing many of the samples used in this work.

- The new additions to the perovskite team Dr. Felix Haase, Annika Raugewitz and Cornelia Marquardt for their continuing efforts to extend our processing capabilities and cell efficiencies.
- David Sylla and Tobias Neubert for structuring our ITO samples and providing us with all types of different masks for different types of sample designs.
- Rolf Reineke-Koch for teaching me ellipsometry analysis and an open ear for several related issues.
- Marita, Ulrike, Hilke, Stefan, Michael, Jan, Dirk, Manuel, Johannes, Christine, Bettina and many more at ISFH, who provide excellent support to keep the ISFH functioning.
- Dr. Marc Halbich, Patrick Schäfer and Katharina Friebe for their continuous support during the duration of my study in Marburg as well as during my time at ISFH.

This work was performed within the framework of the research projects P3T (FKZ 03EE1017B), 27plus6 (FKZ 03EE1056A) and EASi (FKZ 0324040) with funding from the Federal Ministry for Economic Affairs and Climate Action.



# Lebenslauf Marvin Diederich

Kontakt: Unter dem Todtenberg 2A  
31855 Aerzen

Telefon: 01577/6342032  
Mail: marvin.diederich@hotmail.de

Geburtstag/-ort: 25.03.1992/ Homberg(Efze)

Familienstand: ledig

Nationalität: deutsch

## Studium

---

01/2017 – 06/2022 **Wissenschaftlicher Mitarbeiter**  
Institut für Solarenergieforschung Hameln (ISFH)

04/2015 – 12/2016 **Masterstudium Physik**  
Philipps-Universität Marburg  
Abschluss: Master of Science (Note: 1,6)

10/2011 – 03/2015 **Bachelorstudium Physik**  
Philipps-Universität Marburg  
Abschluss: Bachelor of Science (Note: 2,2)

## Schulbildung

---

08/2008 - 05/2011 **Sekundarstufe II**  
Geschwister Scholl Schule Melsungen  
Abschluss: Abitur (Note: 1,5)

Aerzen, den 21.07.22

Marvin Diederich